ANNUAL REPORT 2003

OPTOELECTRONICS DEPARTMENT

UNIVERSITY OF ULM

Contents

1:	Georgi Stareev	2:	Johannes M. Ostermann	3:	Jürgen Mähnß
4:	Eckart Gerster	5:	Martin Stach	6:	Rainer Michalzik
7:	Peter Unger	8:	Peter Brückner	9:	Andrea Kroner
10:	Philipp Gerlach	11:	Ferdinand Scholz	12:	Hendrik Roscher
13:	Manfred Mundbrod	14:	Christoph Eichler	15:	Frank Demaria
16:	Barbara Neubert	17:	Sven-Silvius Schad	18:	Frank Habel
19:	Steffen Lorch				

Missing in the picture

20:	Rainer Blood	21:	Christine Bunk	22:	Karl J. Ebeling
23:	Daniel Hofstetter	24:	Ihab Kardosh	25:	Sükran Kilic
26:	Hildegard Mack	27:	Gerlinde Meixner	28:	Susanne Menzel
29:	Michael C. Riedl	30:	Fernando Rinaldi	31:	Josef Theisz

Optoelectronics Department
University of Ulm

Albert-Einstein-Allee 45, D-89081 Ulm, Germany
URL: http://www-opto.e-technik.uni-ulm.de
Fax: +49–731/50–260 49
Phone: +49–731/50–

Head of Department

Prof. Dr.	Peter Unger	–2 60 54	peter.unger@e-technik.uni-ulm.de

Deputy Head

Prof. Dr.	Ferdinand Scholz	–2 60 52	ferdinand.scholz@e-technik.uni-ulm.de

President of the University of Ulm (Rector)

Prof. Dr.	Karl Joachim Ebeling	–2 60 51	karl.ebeling@e-technik.uni-ulm.de

Senior Research Assistant

Dr.-Ing.	Rainer Michalzik	–2 60 48	rainer.michalzik@e-technik.uni-ulm.de

Cleanroom Management

Dr.-Ing.	Jürgen Mähnß	–2 60 53	juergen.maehnss@e-technik.uni-ulm.de

Secretaries

	Christine Bunk	–2 60 50	christine.bunk@e-technik.uni-ulm.de
	Sükran Kilic	–2 60 51	suekran.kilic@e-technik.uni-ulm.de
	Hildegard Mack	–2 60 59	hildegard.mack@e-technik.uni-ulm.de

Research Staff

Dipl.-Ing.	Peter Brückner	–2 60 35	peter.brueckner@e-technik.uni-ulm.de
Dr.-Ing.	Eckard Deichsel*	–2 60 57	eckard.deichsel@e-technik.uni-ulm.de
Dipl.-Phys.	Frank Demaria	–2 60 46	frank.demaria@e-technik.uni-ulm.de
Dr.-Ing.	Irene Ecker*	–2 60 41	irene.ecker@e-technik.uni-ulm.de
Dipl.-Ing.	Christoph Eichler	–2 61 95	christoph.eichler@e-technik.uni-ulm.de
Dipl.-Ing.	Philipp Gerlach	–2 60 37	philipp.gerlach@e-technik.uni-ulm.de
Dipl.-Ing.	Eckart Gerster	–2 60 57	eckart.schiehlen@e-technik.uni-ulm.de
Dipl.-Ing.	Frank Habel	–2 64 52	frank.habel@e-technik.uni-ulm.de
Dipl.-Ing.	Ihab Kardosh	–2 60 36	ihab.kardosh@e-technik.uni-ulm.de
Dipl.-Ing.	Steffen Lorch	–2 60 39	steffen.lorch@e-technik.uni-ulm.de
Dipl.-Phys.	Manfred Mundbrod	–2 60 39	manfred.mundbrod@e-technik.uni-ulm.de
Dipl.-Ing.	Barbara Neubert	–2 64 54	barbara.neubert@e-technik.uni-ulm.de
Dr.	James O'Callaghan*	–2 60 36	james.ocallaghan@e-technik.uni-ulm.de
Dipl.-Phys.	Johannes M. Ostermann	–2 60 38	johannes-michael.ostermann@ e-technik.uni-ulm.de
Dipl.-Ing.	Michael C. Riedl	–2 60 36	michael.riedl@e-technik.uni-ulm.de
Dipl.-Phys.	Fernando Rinaldi	–2 60 46	fernando.rinaldi@e-technik.uni-ulm.de

Dipl.-Ing.	Hendrik Roscher	–2 60 36	hendrik.roscher@e-technik.uni-ulm.de
Dipl.-Ing.	Sven-Silvius Schad	–2 61 95	sven-silvius.schad@e-technik.uni-ulm.de
Dipl.-Ing.	Marcus Scherer*	–2 60 35	marcus.scherer@e-technik.uni-ulm.de
Dipl.-Phys.	Matthias Seyboth*	–2 60 35	matthias.seyboth@e-technik.uni-ulm.de
Dipl.-Ing.	Martin Stach	–2 60 37	martin.stach@e-technik.uni-ulm.de
Dr.-Ing.	Georgi Stareev	–2 64 53	georgi.stareev@e-technik.uni-ulm.de

Technical Staff

	Rainer Blood	–2 60 44	rainer.blood@e-technik.uni-ulm.de
	Gerlinde Meixner	–2 60 41	gerlinde.meixner@e-technik.uni-ulm.de
	Susanne Menzel	–2 60 41	susanne.menzel@e-technik.uni-ulm.de
	Josef Theisz	–2 60 30	josef.theisz@e-technik.uni-ulm.de

* Member has left the department meanwhile

Preface

The year 2003 was another successful one for the Optoelectronics Department. Research concentrated on optical interconnect systems, vertical-cavity surface-emitting lasers (VCSELs), GaN-based electronic and optoelectronic devices, optically pumped semiconductor disk lasers, unstable-resonator edge-emitting lasers, and high-power laser amplifiers. The VCSELs and Optical Interconnects Group has been prolific in the fabrication of novel VCSEL structures, the analysis of electroabsorption modulators integrated with DFB lasers, as well as the investigation of optical data transmission systems. Outstanding results have been obtained with polarization-stable VCSELs and flip-chip bonded two-dimensional arrays. In the GaN Electronics and Optoelectronics Group, a time-resolved measurement method has been developed which allows a detailed characterization of the local temperature effects in InGaN narrow-stripe laser diodes. Together with a numerical model, this novel method provides a better understanding of the microscopic physical effects in nitride-based semiconductor lasers. In the High-Power Semiconductor Laser Group, a semiconductor disk laser emitting at around $1200\,\mathrm{nm}$ has been realized in the GaAsSb/GaAs material system. Using intra-cavity second-harmonic generation, the first orange-emitting semiconductor disk laser has been demonstrated.

In March, Dr. Ferdinand Scholz, formerly with the University of Stuttgart, joined the Department as a new Professor, now heading the GaN Electronics and Optoelectronics Group. His strong expertise in epitaxial growth techniques will strengthen the research activities in this field which is of vital importance for the Department. In October, our former head Karl Joachim Ebeling who had left the Department in April 2002 to serve as Director of Research at Infineon Technologies, was appointed President of the University of Ulm. In November, Rainer Michalzik and Peter Unger were awarded with the Merckle Research Prize for their research on semiconductor lasers with vertical resonator configurations. Seven members of the Department, namely Eckard Deichsel, Franz Eberhard, Thomas Knödl, Safwat W.Z. Mahmoud, Felix Mederer, Veit Schwegler, and Heiko Unold received their Ph.D. degrees. Furthermore, nine Diploma or Master Theses and five Semester Projects have been carried out in 2003.

The Department further intensified the close cooperation with industrial partners. We also appreciate the financial support of national and European research organizations, which contribute the major part of our funding. Numerous publications at international conferences and a large number of articles in respected journals document the strong research activities. A detailed list is provided at the end of this Annual Report.

Peter Unger   Ulm, January 2004

Ridge-Waveguide Lasers with Tilted Facets

Manfred Mundbrod

In this article, we report on the dependence of the residual facet reflectivity on the facet tilt angle of a ridge-waveguide laser working in the fundamental mode. This includes the design of the test devices, a short description of the Hakki-Paoli measurement method and a presentation of the experimental results for the modal facet reflectivity. Additionally, we show a theoretical calculation of the facet reflectivity and compare this with our experimentally obtained data. The plausibility of the parameters used in the calculation is verified.

1.   Introduction

The undesired spectral gain ripple which arises due to the Fabry-Pérot resonance can be considered a major limitation for the performance of semiconductor laser amplifiers. The angling of the waveguide from the cleavage plane as shown in Fig. 1 provides a simple way to overcome the need for tightly controlled multi-layer antireflection coatings of the facets, when reflectivities below $1 \cdot 10^{-4}$ are desired [1, 2].

It is important for an optical amplifier that self-oscillation is sufficiently suppressed because the wavelength of the master laser doesn't have to be adjusted to the very narrow Fabry-Pérot resonances of the amplifier which is very complex. Furthermore, self-oscillation leads to enhanced filamentation which deteriorates the beam quality.

2.   Experimental Results

2.1   Design of the Test Lasers

The design of the test lasers is illustrated in Fig. 1. The lasers consist of a $50\,\mu$m-long straight part, followed by a $450\,\mu$m long bent waveguide whose radius of curvature is chosen in such a way, that the waveguide and the cleavage plane include the angle $90° - \theta$. The tilt angle of the facet is then equal to θ and varies from 0° to 10°. This was carried out for nominal ridge widths of 3, 4, and $5\,\mu$m.
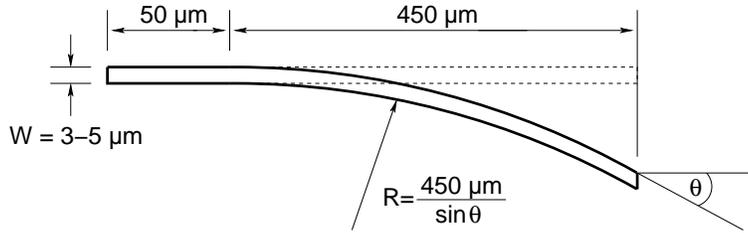
Fig. 1: Design of the test lasers.

2.2   Measurement Method

For the determination of the modal reflectivity of the tilted facet the so-called Hakki-Paoli method is used [3, 4]. Here, the lasers are driven at the threshold current of a completely straight laser ($\theta = 0°$). Then the emitted light is coupled into a spectrum analyzer. A part of a typical spectrum of a $500\,\mu$m long ridge-waveguide laser can be seen in Fig. 2. With the minima and maxima of the Fabry-Pérot resonances of the spectrum, the modulation index m can be calculated

$$m = \frac{I_{\max} - I_{\min}}{I_{\max} + I_{\min}} \, .$$

If we assume that the modal reflectivity R of the perpendicular laser facet remains the same for all lasers, the modal reflectivity R^* of the ridge waveguide at the tilted facet can be determined as follows:
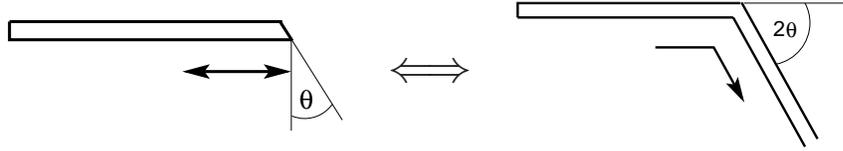
$$R^* = R \left(\frac{1 - \sqrt{1 - m^2}}{m} \right)^2 .$$

This is shown in the diagram on the right-hand side in Fig. 2.
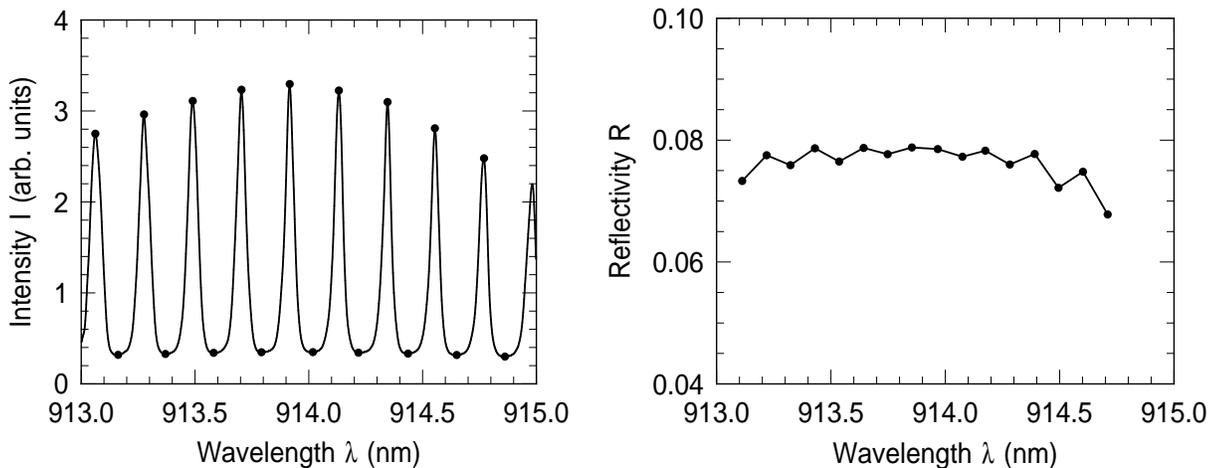
Fig. 2: Spectrum of a ridge-waveguide laser and calculated modal reflectivity of the tilted facet.

## 2.3 Theoretical Calculation of the Modal Facet Reflectivity

Fig. 3: Equivalent model for the calculation of the facet reflectivity.

The reflectivity of the fundamental mode at a tilted facet of a ridge-waveguide laser can be theoretically calculated using a model as described in [2]. As sketched in Fig. 3, the problem of collecting the light reflected from the tilted mirror back into the laser waveguide is equivalent to the problem of light transmission from the laser waveguide into a waveguide tilted by an angle of 2θ. The fundamental mode in this tilted outgoing waveguide is excited by the incident field. If the two fields were perfectly aligned, the transmission coefficient would be unity. So the loss is caused by the misalignment of the phase fronts, which is in this case $\Delta\varphi(x) = \beta x \cdot 2\tan\theta \approx 2\beta\theta x$. According to [5], the coupling coefficient of two waveguides is proportional to the correlation integral of the two fields. The modal power reflection coefficient is no given by

$$R = R_{\mathrm{f}}(\theta) \cdot |c|^2 \qquad \text{with} \quad c \propto \int\limits_{-\infty}^{\infty} |E_{\mathrm{y}}|^2 \cdot e^{i2\theta\beta x} dx \, ,$$

where E_{y} is the y-component of the fundamental TE mode of the waveguide. $R_{\mathrm{f}}(\theta)$ is the Fresnel reflection coefficient of the dielectric interface between laser crystal and air.
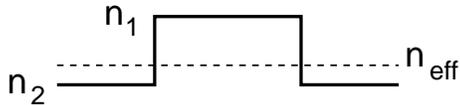
**Fig. 4:** Slab model for the ridge waveguide and corresponding refractive indices.

When we apply a simple slab model for our ridge waveguide, as indicated in Fig. 4, we obtain the following solution for the fundamental mode in the waveguide:

$$
\begin{aligned}
E_{\mathrm{y}} &= A \cdot \cos(\kappa x) \, , & |x| &\leq d \\
E_{\mathrm{y}} &= A \cdot \cos(\kappa d) \cdot e^{-\gamma(|x|-d)} \, , & |x| &> d
\end{aligned}
\qquad \text{with} \qquad
\begin{aligned}
\kappa^2 &= n_1^2 k_0^2 - \beta^2 \\
\gamma^2 &= \beta^2 - n_2^2 k_0^2 \, ,
\end{aligned}
$$

with $k_0 = 2\pi/\lambda$ and $\beta = 2\pi n_{\mathrm{eff}}/\lambda$. So, by solving the correlation integral we obtain the dependence of the modal reflectivity on the angle. Free parameters are in this case the width d of the ridge waveguide and the three refractive indices n_1, n_2, and n_{eff} which account for the shape of the fundamental mode.

2.4　Comparison with Experimental Results

Figure 5 shows the reflectivity in dependence of the facet angle for uncoated ridge-waveguide lasers with nominal ridge widths of $3\,\mu\mathrm{m}$, $4\,\mu\mathrm{m}$, and $5\,\mu\mathrm{m}$. The dots in the diagrams represent the experimentally determined values using the Hakki-Paoli method. The solid lines, however, are calculated as described above using the indicated numbers for n_1, n_2, n_{eff}, and d.
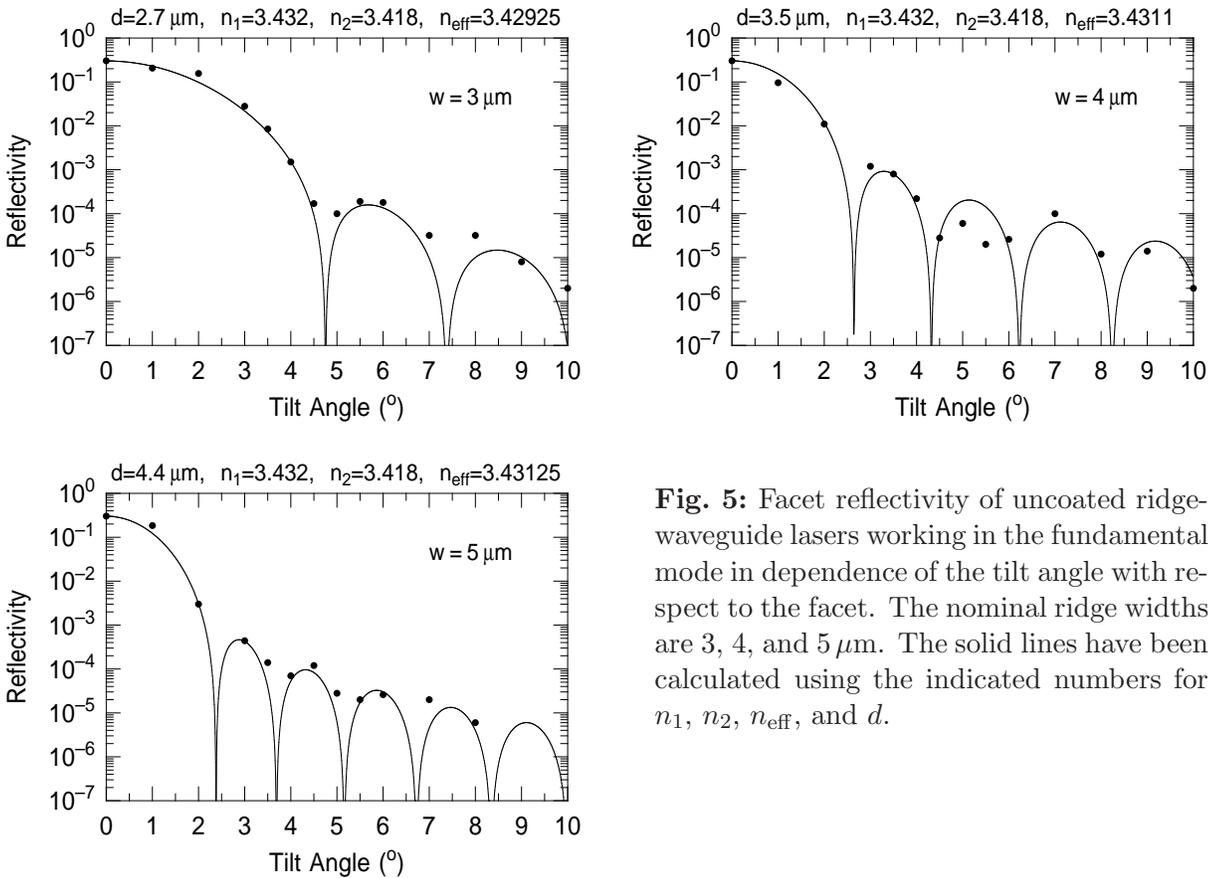
Fig. 5: Facet reflectivity of uncoated ridge-waveguide lasers working in the fundamental mode in dependence of the tilt angle with respect to the facet. The nominal ridge widths are 3, 4, and $5\,\mu\mathrm{m}$. The solid lines have been calculated using the indicated numbers for n_1, n_2, n_{eff}, and d.

The measured data fit very well to the calculated reflectivity. For $0°$, the reflectivity is the usual Fresnel-reflectivity caused by the step of refractive index between laser crystal and air. From the diagrams it can be seen that the reflectivity then drops rapidly with increasing facet angle. The broader the waveguide is, the faster is the decline of the reflectivity. At a tilt angle of about $4.5°$, the reflectivity is for all ridge widths in the range of 10^{-4}. The lowest value for the reflectivity is $2\cdot10^{-6}$ for $\theta = 10°$. If additionally an antireflection coating was applied on the laser facet, the Fresnel reflectivity would be lowered which even further decreases the overall facet reflectivity.

The calculated curves show several dips in the reflectivity. Again, the broader the waveguide is, the smaller is the angle at which the first dip arises, and the more often the dips appear. It is experimentally very hard to meet the exact angle of a specific dip. This

would only be possible if the exact mode structure or the exact waveguide parameters were known. But the technological tolerances in fabricating the ridge waveguide are too big for this. Anyway, with a residual reflectivity of 10^{-4} self-oscillation of an optical amplifier for example with an angled ridge-waveguide section can be suppressed sufficiently.

2.5 Plausibility of the Fit Parameters

The discrepancy between the nominal value for the ridge width as designed on the lithography mask and the value used for the calculation of the reflectivity can be easily explained with Fig. 6.
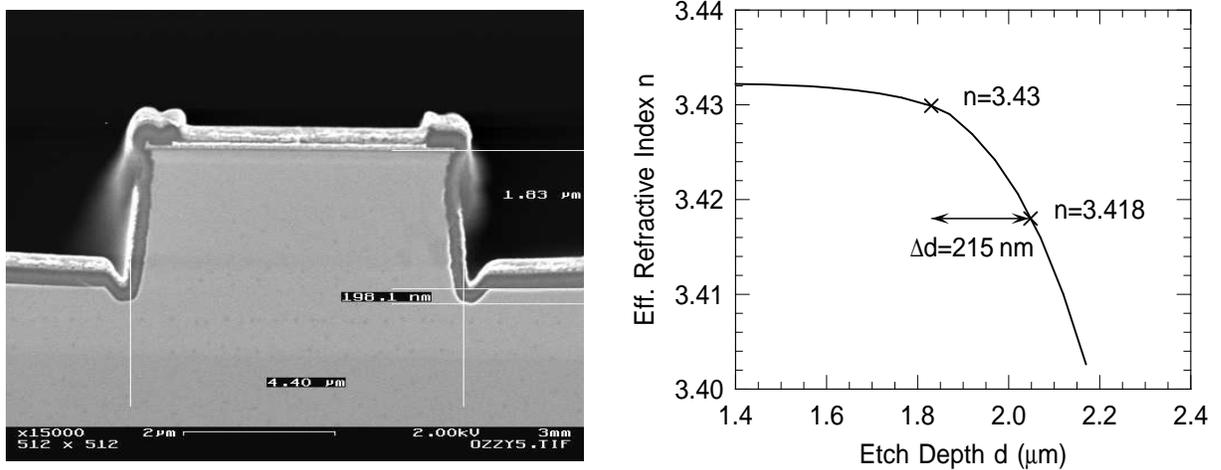
Fig. 6: SEM cross section of a nominal $5\,\mu$m wide ridge (left) and calculated effective refractive index in dependence on the etching depth for the used epitaxial laser material (right).

First, the ridge width taken from the SEM picture is consistent with the value used for the calculation. On the lithography mask the ridge is designed for $5\,\mu$m, but the processing effects a shrinkage of the waveguide. Another feature of the etch process to form the ridge are the sputter trenches on both sides of the ridge. Here, the semiconductor material is locally etched deeper which leads to a significant deacrease of the effective refractive index in the etched regions. This can be seen in the diagram on the right side of Fig. 6, where the effective refractive index of the epitaxial layer structure is plotted versus the etching depth. Instead of the intended etch depth of $1.83\,\mu$m, the additional $200\,$nm decrease the effective index from 3.43 to 3.418.

The refractive index of the unetched layer structure can also be calculated easily using a transfer-matrix method. So, finally, only the effective index of the mode n_{eff} remains as a really free fit parameter for the calculation.

3. Conclusion

In this article the dependence of the residual facet reflectivity on the facet tilt angle of a ridge-waveguide laser working in the fundamental mode was shown. For this purpose, the design of the test lasers and the measurement method according to Hakki and Paoli have been described. Also a model for the theoretical calculation of the facet reflectivity has been presented.

The experimentally obtained data and the calculated values are in very good agreement. The residual facet reflectivity drops rapidly with increasing tilt angle. For all ridge widths, the residual facet reflectivity was already in the range of 10^{-4} at a tilt angle of $\theta = 4.5°$. The lowest value was $2 \cdot 10^{-6}$ for $\theta = 10°$. The parameters used for the theoretical calculation of the reflectivity were also in good agreement with experimentally determined waveguide parameters.

Consequently, a ridge waveguide with a tilted end facet is an ideal structure to work as a preamplifier in combination with a gain-guided flared amplifier as a high-power laser amplifier having high brightness.

References

[1] A.J. Collar, G.D. Henshall, J. Farré, B. Mikkelsen, Z. Wang, L. Eskildsen, D.S. Olesen and K.E. Stubkjaer, "Low residual reflectivity of angled-facet semiconductor laser amplifiers," *IEEE Photon. Technol. Lett.*, vol. 2, pp. 553–555, 1990.

[2] D. Marcuse, "Reflection loss of laser mode from tilted end mirror," *IEEE J. Lightwave Technol.*, vol. 7, pp. 336–339, 1989.

[3] I.P. Kaminov, G. Eisenstein, and L.W. Lutz, "Measurement of the modal reflectivity of an antireflection coating on a superluminescent diode," *IEEE J. Quantum Electron.*, vol. 19, pp. 493–495, 1983.

[4] B.W. Hakki and T.L. Paoli, "Gain spectra in GaAs double-heterostructure injection lasers," *J. Appl. Phys.*, vol. 46, pp. 1299–1306, 1975.

[5] K.J. Ebeling, *Integrated Optoelectronics,* Berlin: Springer-Verlag, 1993

High Brightness Semiconductor Laser Amplifiers with Tilted Facets

Frank Demaria

As a part of master-oscillator power-amplifier configurations, semiconductor laser amplifiers show the capability of emitting high-power laser radiation with excellent spatial beam quality. We report on 920 nm laser emission of such a device with a diffraction limited power fraction of 1.5 W of a slow-axis diffraction number $M_s^2 < 1.05$. The chip design includes a ridge waveguide preamplifier section with a tilted input facet in combination with a gain-guided flared amplifier section.

1. Introduction

In hybrid all-semiconductor master-oscillator power-amplifier (MOPA) configurations, the fairly low optical output power of a spatial single-mode laser diode is increased by an optical amplifier, while its spatial and spectral properties remain almost unchanged. The requirement of low residual facet reflectivities for the amplifier with less than 10^{-4} can just be fulfilled by high quality multi-layer anti-reflection coatings. However, modal reflectivity measurements have shown in good agreement with calculations that this can be achieved more easily by ridge waveguides with tilted end facets [1]. In conclusion, the combination of both actually reduces the reflectivity even more and therefore can be regarded as the optimum concept for such devices.
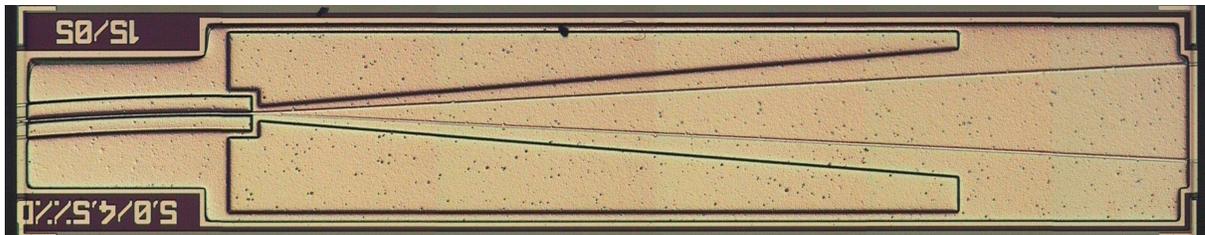
Fig. 1: Microscope image of a laser amplifier. The bended ridge-waveguide section hits the input facet at the left side with a tilt angle of 4.5 °. Both facets are covered with a 4-layer broad-band anti-reflection coating. The gain-guided flared section on the right is flanked by absorbers in order to surpress parasitical criss-cross lasing.

2.   Device Structure

Figure 1 shows an amplifier with a $500\,\mu$m long and $5\,\mu$m wide ridge-waveguide. In the input region of the tapered section we added lateral absorbers in order to absorb the residual reflections from the output facet and to prevent lateral parasitical lasing. The electrogalvanic layer at the top of the contact is clearly visible. Its offset at the edges is necessary for proper individualisation of the devices by cleaving.

To permit high power operation, the ridge-waveguide preamplifier section is connected to a gain-guided flared power amplifier section. There, due to diffraction, the optical wave expands laterally whilst it is amplified and therefore obtains high power levels beyond $1\,$W as it is coupled out at the output facet.

We fabricated various amplifiers out of different epitaxial materials with miscellaneous lateral structures. The overall length of the devices generally was chosen $2.51\,$mm according to the $2.5\,$mm long heat spreaders on which the amplifiers are mounted junction-side down. Two different ridge-waveguide section lengths of $0.5\,$mm and $0.75\,$mm have been fabricated, both with a tilt angle of $4.5°$. The full taper angle of the flared section is $6°$. For a good performance, the internal diffraction angle should be optimized with respect to a reasonable overlap of the optical mode and the pumped region. To investigate this influence and to find out the optimum, the width of the ridge has been varied from $3\,\mu$m to $5\,\mu$m with a step size of $0.5\,\mu$m. Besides that a precise control of the etch depth was necessary, because this determines properties of the waveguide.

3.   Characterisation of Beam Quality

There are many approaches of benchmarking the beam quality of broad area semiconductor lasers. For flared gain region devices it is quite common to take advantage from their astigmatism by measuring the lateral intensity distribution in the external focus of a vertically collimated beam. It is compared to the distribution which is expected for an ideal diffraction limited beam [2].

Another approach defines the beam quality factor M^2 with which the beam divergence exceeds that of a diffraction limited beam [3]. There are commercial beam analysing measurement devices available that allow a quantification of the M^2-value. The brightness of a light source is defined as the power P emitted per surface area A into the solid angle Ω

$$B = \frac{P}{A\,\Omega}\,. \tag{1}$$

It is connected to the fast and slow axis' diffraction number of an edge-emitting laser diode M_{f}^2 and M_{s}^2 by

$$B = \frac{P}{\lambda^2 M_{\mathrm{f}}^2 M_{\mathrm{s}}^2}\,. \tag{2}$$

As for typical high-power semiconductor devices the approximation $M_{\mathrm{f}}^2 \approx 1$ is valid [5], P/M_{s}^2 is a good measure for the brightness at a given wavelength.

However, accurate M^2 determination requires definite beam width measurement [4], which can be performed in different ways and with different boundary conditions. This is why we observed a poor comparability of M^2-values for measurements with different beam analyzing systems.

We overcame that problem by a setup that implies both of the methods mentioned above. As shown in Fig. 2, we placed a variable slit in the plane of the corrected farfield and
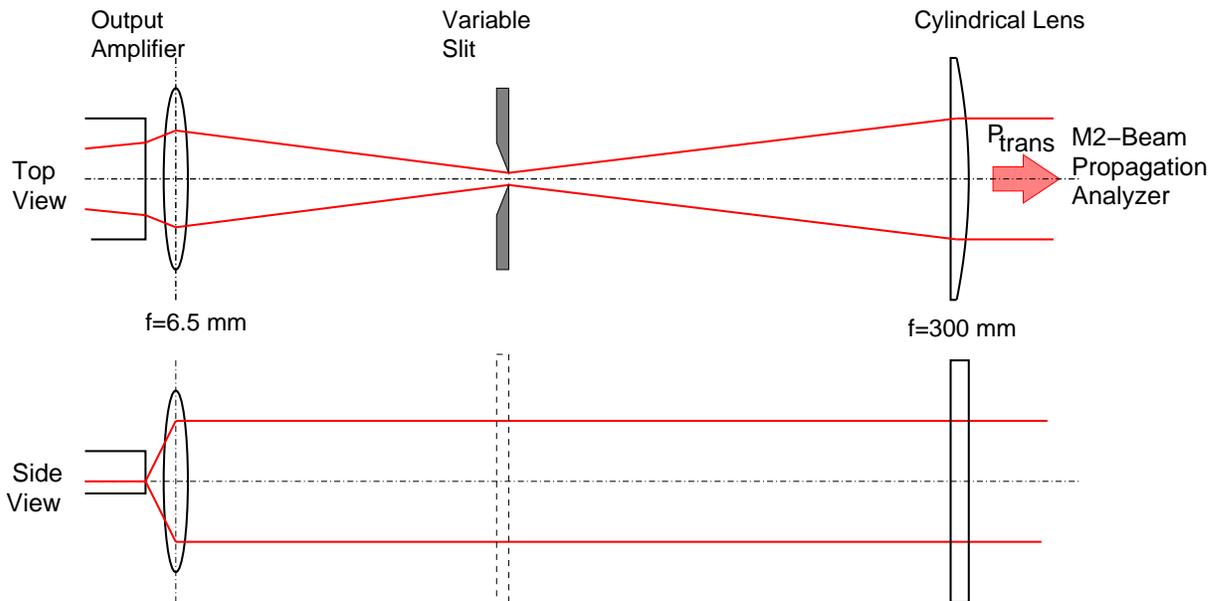

Fig. 2: Setup for characterisation of the amplifiers' beam quality. Because of the strong astigmatism, the vertically collimated beam is convergent in the lateral direction. At its beam-waist a variable slit is placed which acts as a spatial mode filter. The absolute and relative power of the transmitted beam and its quality factor M^2 are qualified.

measured the M^2-factor of the transmitted beam as well as the optical power before and after the slit. The advantage of this measurement-method consists not only of the high information about the emitted beam that has to be characterised. As for a small aperture the slit filters out higher order modes, the transmitted power gives instantaneous information about the brightness. It therefore is a fast and convenient method to find out the best parametrical conditions for the amplifier.

4. Experimental Results

The results presented here have been obtained by using amplifiers with 750 μm long ridge. They have been fabricated out of epitaxial material that has been provided by the *Ferdinand-Braun-Institut für Höchstfrequenztechnik, Berlin*. As a signal laser, we used a laterally single-mode Fabry-Pérot laser diode. The optical powers have been generally measured in the collimated optical beam. For the M^2-measurements we used the *Coherent*
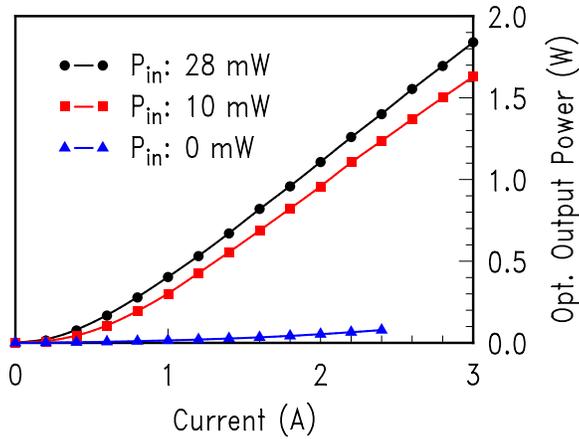
Fig. 3: Optical output characteristics for different optical input powers and a free-running amplifier at a temperature of 20° C. The ridge has a width of 4.5 μm and a length of 750 μm. The optical output power was measured in the collimated beam.

Mode Master-PC beam propagation analyzer. According to Fig. 3, the optical output power and the differential quantum efficiency of 53 % at 28 mW optical injection are compareable to results we achieved up to now. To make sure to preserve the device for further investigations we restricted ourselves to low currents and optical output powers in this measurement. The remarkable characteristics is the extremely low optical output power of the free running amplifier and the outstanding linearity of the curves. Also the saturation characteristics, which is depicted in Fig. 4, is quite good, but not much better than that of less sophisticated devices we already fabricated in the past. The real progress
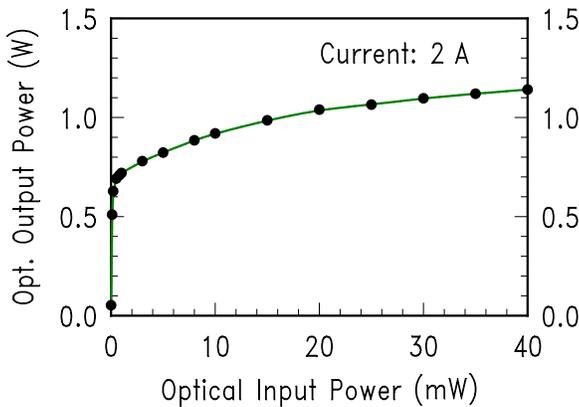
Fig. 4: Saturation characteristics for the same device as in Fig. 3. For 1 mW input power, the device is fairly saturated with an output of 720 mW. For even lower input powers, the small signal net-gain exceeds 30 dB.

is manifested in the beam quality measurement. In formerly fabricated devices we always observed strong degradation of the beam quality with increasing optical output power of values above 1 W. For amplifiers with the new design, the beam quality is distinctly enhanced even for high powers. The measurement given in Fig. 5, exemplifies that. It has been performed as explained in Section 3. By cutting off the side-lobes of the intermediate focus, which contained about 16 % of the optical power, we achieved a diffraction limited beam. Its diffraction number was less than 1.05, the optical power was 1.5 W. With the reduction of the slit width and the decrease of the diffraction number, a smoothening of the collimated beam after the slit and the cylindrical lens took place. At minimal diffraction number, the collimated beam is nearly perfectly round and smooth. With
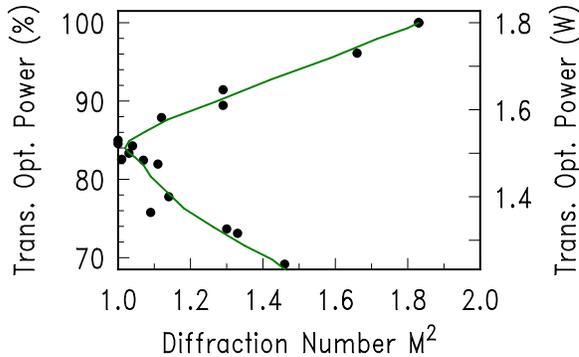
Fig. 5: Beam quality measurement according to Fig. 2. The amplifiers' ridge has a width of $4.5\,\mu$m and a length of $750\,\mu$m. The current was $3\,$A, the optical input power $42.2\,$mW. The power fraction of the diffraction limited beam is $84\,\%$ which is eqivalent to $1.5\,$W.

further reduction of the slit width, the diffraction number is increasing again and the collimated beam becomes broader. At this state, already the central lobe is cutted and due to the reduction of its width, the diffraction angle increases. Because the shape is more and more transformed from gaussian-like to tophat-like, the diffraction number is also increasing. It has to be added that a lateral variation of the coupling lens position at the input facet considerably affected the beam quality, so this position had to be optimised.

5. Conclusion and Discussion

We demonstrated the capabilities of laser-amplifiers with ridge-waveguide preamplifiers as high brightness laser sources by creating diffraction limited emission of $1.5\,$W at a wavelength of $920\,$nm. The devices showed good saturation behavior. We also demonstrated a useful way of beam quality and brightness characterisation by taking advantage from an external mode filter. This measurement method reveals a general problem of beam quality characterisation. In Eqn. (1) the brightness represents an integral value over the area A and solid angle Ω. As the spatial and angular intensity distribution is quite inhomogeneous, a clear definition of the spatial scope which is taken into account is necessary. The full width at half maximum (FWHM) definition of beam width and angle leads to much higher brightness values, consistent with the fact that the local brightness actually is bigger near the optical axis. Equation (2) bases on the $1/e^2$ clipping level definition, which generally should be used in that context.

Anyway, because of the assumed constance of M_f^2 and the presented measurement in Fig. 5, we showed that according to definition (2), the brightness of a non-gaussian beam can be increased by a simple external mode filter. Regardless of the fact, that the achievable maximum optical power density in the focused beam is not increased by that way.

References

[1] M. Mundbrod, "Ridge-waveguide lasers with tiltet facets," *Annual Report 2003, Dept. of Optoelectronics, University of Ulm.*

[2] J. N. Walpole, "Semiconductor amplifiers and lasers with tapered gain regions", *Opt. Quantum Electron.*, vol. 28, pp. 623–645, 1996.

[3] M.W. Sasnett, T.F. Johnston, Jr., "Beam characterization and measurement of propagation attributes", in *Laser Beam Diagnostics*, R.N. Hindy and K. Kohandazeh (Eds.), Proc. SPIE 1414, pp. 21–32, 1991.

[4] A.E. Siegmann, M.W. Sasnett, T.F. Johnston, Jr., "Choice of clip levels for beam width measurements using knife-edge techniques", *IEEE J. Quantum Electron.*, vol. 27, no. 4, pp. 1098–1104, 1991.

[5] H. Wenzel, B. Sumpf, G. Erbert, "High-brightness diode lasers", *C. R. Physique*, vol. 4, pp. 649–661, 2003.

Theory and Measuring of Antireflection Coatings

Steffen Lorch

The characterization of antireflection (AR) coatings is not trivial. A preferred measurement method is the Hakki-Paoli method. But for broad-area lasers, an advanced method has to be used. One way is the measurement of the spectrally resolved far field, another is the use of single-mode ridge-waveguide lasers. Different AR coatings in the range of 10^{-1}–10^{-4} (fabricated by ion-beam sputter deposition) have been deposited on single-mode lasers and characterized successfully.

1.   Introduction

Antireflection (AR) coatings with reflectivities lower than 10^{-4} are required for many applications such as laser amplifiers. These coatings can be deposited by reactive ion-beam sputter deposition [1] to achieve the required reflectivities with low absorption and a good passivation of the semiconductor material. The measurement of antireflection coatings with reflectivities below $R < 10^{-2}$ is not trivial.

2.   Measurement Methods

A quick and simple method to determine the reflectivity of a coating on a laser facet is the threshold-shift method [1]. The L–I curve is measured before and after the deposition of the coating. The threshold current increases with decreasing reflectivity, see Fig. 1.

$$R^* = R \left(\frac{I_{\text{th}}}{I_{\text{th}}^*}\right)^{2L\Gamma g_0} . \tag{1}$$

Whereas R^* is the reflectivity of the coated facet, which can be calculated from the threshold currents of the uncoated I_{th} and the coated I_{th}^* lasers. For this calculations, the laser length L, the gain Γg_0, and the effective refractive index n_{eff} have to be known. The reflectivity R of the uncoated laser is $R = \left(\frac{1-n_{\text{eff}}}{1+n_{\text{eff}}}\right)^2$. Using this method, high-reflection (HR) coatings can also be measured. If the parameters of the uncoated laser are not known, the reflectivity can be determined with an advanced method described in [2]. Using this threshold-shift method, antireflection coatings with reflectivities up to $R \geq 10^{-3}$ can be measured. For lower reflectivities, no threshold can be found and this method cannot be used.
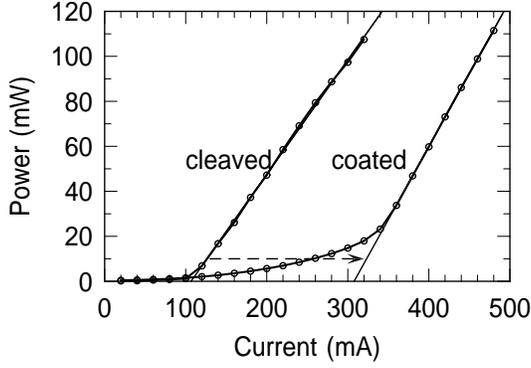
Fig. 1: Threshold-shift method; With decreasing reflectivity R the threshold current I_{th} increases.
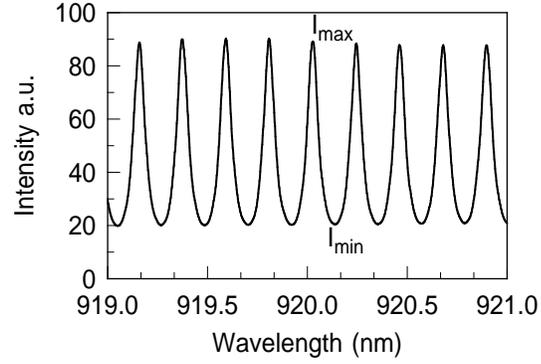
Fig. 2: Hakki-Paoli (Kaminow-Eisenstein) method; Modulation of the intensity I over wavelength λ.

For low reflectivities, the Kaminow-Eisenstein method [3] which is based on Hakki-Paoli [4] is a method commonly used for the determination of the reflectivity. The coated laser is operated with the current corresponding to the threshold current of the uncoated laser. With a spectrometer, the modulation of the intensity over wavelength is measured (see Fig. 2) and with

$$m = \frac{I_{\max} - I_{\min}}{I_{\max} + I_{\min}} \quad , \qquad m = \frac{2a}{1 + a^2} \quad , \text{ and} \qquad R^* = a^2 R_1 \tag{2}$$

the reflectivity R^* can be calculated. The effective refractive index n_{eff} has to be known to calculate the reflectivity R of the uncoated laser. For broad area lasers when a simple optic is used to couple the light directly into a spectrometer, the spectral modulation and so the calculated reflectivity is too low. The reason is the difference in the spectrum for different propagation angles. This will be discussed in the next section.

3. Theory

In a laser, there are modes with different propagation angles. Assuming single mode behavior in the vertical (y) direction, there are different propagation angles in the lateral (x) direction. The laser length L is orientated in (z) direction.
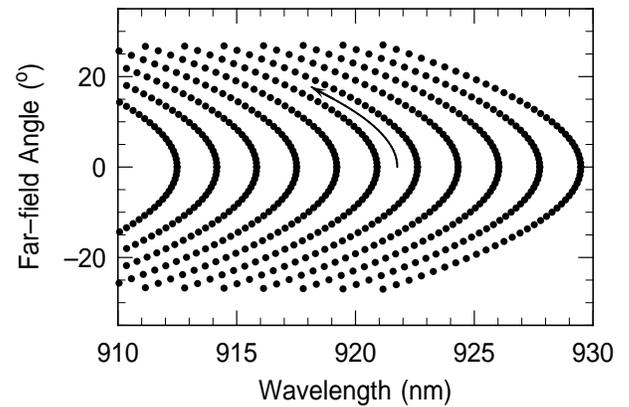
3.1 Simulation

In Fig. 3, the k_x/k_z diagram for a laser with a length of $L_z = 500\,\mu$m and a width of $L_x = 100\,\mu$m is shown.

$$k = \sqrt{(nk_x)^2 + (nk_z)^2} = \frac{2\pi n}{\lambda} \quad \text{and} \qquad k_{x,z} = \frac{\pi n}{L_{x,z}} . \tag{3}$$

The solutions of constructive superposition are given which results in an intensity maximum in the spectrum are shown as points in the k_x/k_z diagram in Fig. 3. It can be seen that the distance in the longitudinal (z) direction is shorter than in the lateral (x) direction due to the larger length than the width. With increasing angle (increasing k_x) and consistent longitudinal mode (k_z), the absolute value of k increases. This results in a decreasing wavelength. Figure 4 shows the expected form for the spectrally resolved far field. The points demonstrate maxima in the spectrum which shift towards shorter wavelengths with increasing propagation angle.
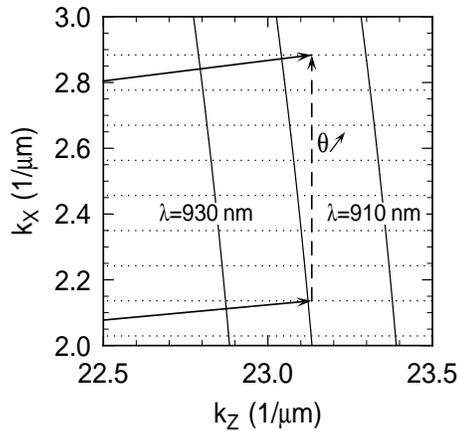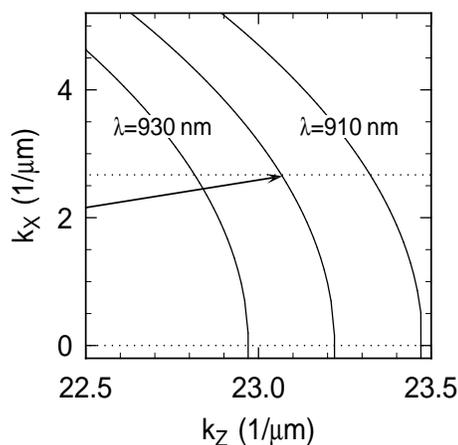

Fig. 3: k_x/k_z diagram of a laser with a length of $L_z = 500\,\mu$m and a width of $L_x = 100\,\mu$m.

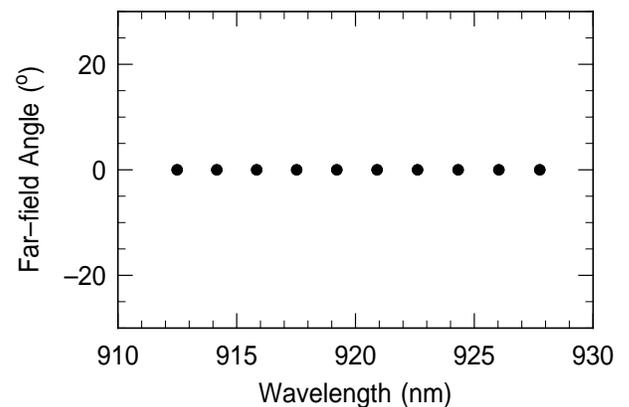**Fig. 4:** Simulation of a spectrally resolved far field for a laser with a length of $L_z = 500\,\mu$m and a width of $L_x = 100\,\mu$m.

In Fig. 5, the k_x/k_z diagram for a laser with a length of $L_z = 500\,\mu$m and a width of $L_x = 4\,\mu$m is shown.

**Fig. 5:** k_x/k_z diagram of a laser with a length of $L_z = 500\,\mu$m and a width of $L_x = 4\,\mu$m.

Fig. 6: Simulation of a spectrally resolved far field for a laser with a length of $L_z = 500\,\mu$m and a width of $L_x = 4\,\mu$m.

In this case, the distance of the points in the k_x direction is much larger due to the small laser width. This results in a different spectrally resolved far field compared to that of the laser with $100\,\mu$m width. Spectral maxima are only expected at an angle of 0° as shown in Fig. 6.

3.2   Measurement

The measurement of the spectrally resolved far field is described in [5] and depicted in Fig. 7. The laser beam is collimated in the vertical direction and focused into the spectrometer. Due to the astigmatism, the horizontal direction shows a focus behind the first collimating lens (corrected far field) which is magnified with a cylindrical lens.
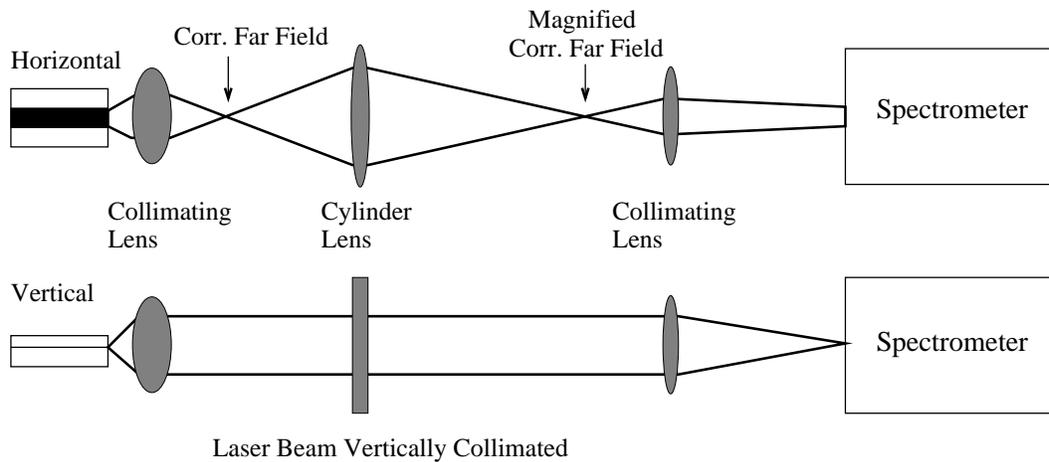

Fig. 7: Measurement setup for the spectrally resolved far field.

Figure 8 shows the measured results for a ridge-waveguide laser with a ridge width of $100\,\mu$m at an emission wavelength of $\lambda = 920\,$nm. The picture shows the intensity over wavelength and far-field angle. The spectrum has the same shape as the simulation in Fig. 4, with increasing far-field angle, the maxima in the intensity shift to shorter wavelengths. In Fig. 9, the spectrally resolved far field of a ridge-waveguide laser with a ridge width of $4\,\mu$m is shown. As shown in the simulation (Fig. 6), only maxima around the far-field angle of 0° can be observed.

Using a spectrally resolved far field, the modulation at one angle can be measured correctly. However, if the entire laser beam is coupled into a spectrometer without filtering out all angles other than that of 0°, the resulting modulation is too low. With increasing angle, the spectrum shifts to shorter wavelengths. Hence, the spectrometer superposes all spectra of the different angles and the resulting spectrum shows lower maxima and higher minima which results in a lower modulation depth and so in lower reflectivities. As the laser width is increased, the apparent calculated reflectivity is lowered.
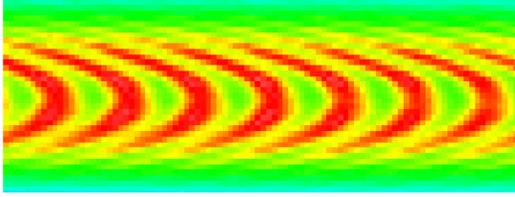
Fig. 8: Spectrally resolved far field of a ridge-waveguide laser with a ridge width of $100\,\mu$m.
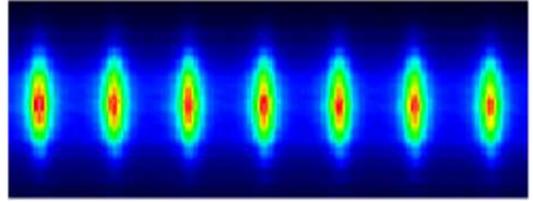

Fig. 9: Spectrally resolved far field of a ridge-waveguide laser with a ridge width of $4\,\mu$m.

4. Results

Ridge-waveguide lasers with different ridge widths have been fabricated [6]. After the deposition of antireflection coatings on one facet (fabricated by ion-beam sputter deposition), the light has been coupled into a spectrometer. Using the modulation of the spectrum, the reflectivity is calculated using Eqn. 2. In Fig. 10, the measured reflectivities for three different AR coatings over ridge width is shown. As expected, the reflectivity decreases with increasing laser width. In the range of laser widths between $3\,\mu$m and $6\,\mu$m, the reflectivities show the values of the designed reflectivities.
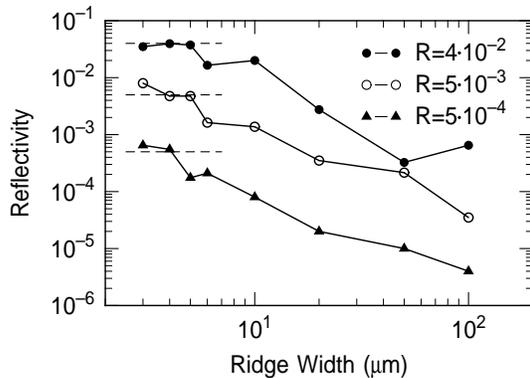
Fig. 10: Reflectivity over ridge width measured with the Hakki-Paoli method.
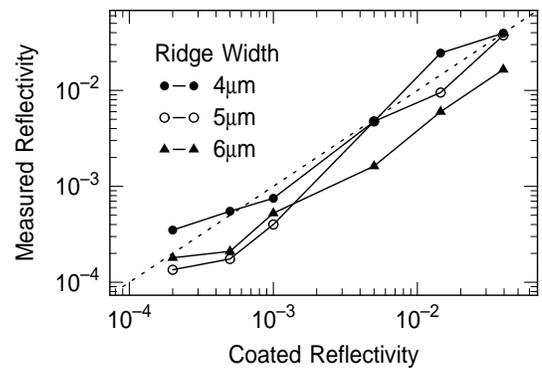
Fig. 11: Calculated and measured reflectivities for different laser widths measured with the Hakki-Paoli method.

Different AR coatings in the range of 10^{-1} to 10^{-4} have been fabricated and measured. In Fig. 11, the results for laser widths between $4\,\mu$m and $6\,\mu$m are shown. As can be seen, the measured values are in the range of the designed reflectivities. This demonstrates that the reflectivities of AR coatings on ridge-waveguide lasers with small ridge widths can be accurately characterized using the Hakki-Paoli method.

5.   Conclusion

Different antireflection coatings have been deposited on ridge-waveguide lasers with ion-beam sputter deposition. Using the Hakki-Paoli method, the reflectivities have been measured. For ridge widths in the range of $4\,\mu$m to $6\,\mu$m, the results are quite good. With such a measurement method, a fast and correct characterization of AR coatings is possible.

References

[1] S. Lorch, "Optical coatings for laser facets fabricated by reactive ion-beam sputter deposition," *Annual Report 2001,* University of Ulm, Optoelectronics Department, ch. 11, pp. 67–72, 2002.

[2] K.S. Repasky, G.W. Switzer, C.W. Smith, and J.L. Carlsten, "Laser diode facet modal reflectivity measurements," *Appl. Optics*, vol. 39, no. 24, pp. 4338–4344, 2000.

[3] I.P. Kaminow, G. Eisenstein, and L.W. Stulz, "Measurement of the modal reflectivity of an antireflection coating on a superluminescent diode," *IEEE J. Quantum Electron.*, vol. 19, no. 4, pp. 493–495, 1983.

[4] B.W. Hakki and T.L. Paoli, "Gain spectra in GaAs double-heterostructure injection lasers," *J. Appl. Phys.*, vol. 46, no. 3, pp. 1299–1306, 1975.

[5] D.J. Bossert and D. Gallant, "Improved method for gain/index measurements of semiconductor lasers," *Electron. Lett.*, vol. 32, no. 4, pp. 338–339, 1996.

[6] M. Mundbrod, "Properties of ridge-waveguide lasers," *Annual Report 2002,* University of Ulm, Optoelectronics Department, ch. 9, pp. 49–54, 2003.

High-Brightness Unstable-Resonator Semiconductor Laser Diodes

Eckard Deichsel

High-power high-brightness unstable-resonator edge-emitting semiconductor laser diodes with dry-etched curved mirrors were fabricated and characterized. The epitaxial structure was optimized for high output power operation and consists of a GaAs/AlGaAs graded-index separate-confinement heterostructure (GRINSCH) with a single 980-nm-emitting InGaAs quantum well. The curved mirrors of the unstable-resonator lasers were fabricated using an optimized chemically assisted ion-beam etching (CAIBE) process. The beam quality of the devices was evaluated by measuring the position and the size of the virtual source. Tapered designs with lateral absorber regions show continuous-wave (cw) output powers of over 1.6 W having 85% of the intensity in the main lobe of the lateral virtual source. A maximum brightness of $150\,MW/(cm^2 sr)$ was achieved in cw operation.

1. Introduction

The concept of unstable resonators using spherically curved mirrors is a common approach for gas and solid-state lasers. First attempts were made in the mid 80s to transfer this concept to edge-emitting semiconductor laser diodes. Since the transverse waveguide of an edge-emitting laser diode is defined by the epitaxial layer sequence, this concept can only be applied to the lateral direction and requires an optimized dry-etching process for the fabrication of the cylindrically shaped mirrors. Unstable-resonator semiconductor lasers of this type offer the advantages of broad-area lasers in terms of high output power combined with an improved lateral beam quality, which leads to a significant improvement in the brightness of the devices [1]. For these lasers, the risk of catastrophic optical mirror damage (COMD) is much lower than for single-mode laser diodes having a lateral waveguide, because the width of the output facet is more than one order of magnitude larger. Handling and mounting techniques are the same as for high-power broad-area lasers having the advantage of an increased brightness. The fabrication sequence is the standard process for broad-area lasers with the inclusion of a dry-etching step for the mirror formation [2, 3]. Additionally, monolithic integration and on-wafer testing becomes possible [4].

2. Theory

The stability of an optical resonator is determined by its cavity length L and radii ρ_1, ρ_2 of curvature of its mirrors. The g parameters are defined as $g_{1,2} = 1 - L/\rho_{1,2}$, whereas

focusing mirrors have positive and defocusing mirrors negative curvature radii. From these parameters, the equivalent G parameter can be determined as $G = 2g_1g_2 - 1$. The condition for stable resonators is $0 < g_1g_2 < 1$ which is equivalent to $|G| < 1$. In this case, a Gaussian beam is the fundamental eigensolution of the resonator. Unstable resonators with $g_1g_2 < 0$ or $g_1g_2 > 1$, which is equivalent to $|G| > 1$, have complex eigensolutions. Unstable does not mean that there is no stable laser oscillation, but that a Gaussian beam inside the resonator is magnified by a factor $M = |G| + \sqrt{G^2 - 1}$ after each round trip and is therefore not a stable eigensolution. However, there are spherical wavefronts which reproduce themselves after each round trip. With increasing magnification M, the loss of the resonator increases. The stability diagram in Fig. 1 shows the conditions for stable and unstable resonators. Details of the theory can be found in [5, 6].
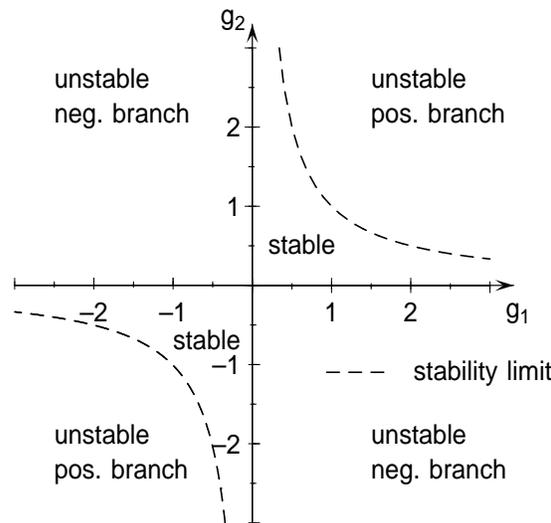

Fig. 1: Stability diagram for an optical resonator. The stability is determined by the parameters $g_{1,2}$ which can be calculated from the resonator length L and the mirror curvature radii $\rho_{1,2}$ of the front and back facet. The stability limits are the dashed lines $g_1g_2 = 1$ ($G = 1$) and the axes of the diagram $g_1g_2 = 0$ ($G = -1$).

In the stability diagram, there are two types of unstable resonator regions which are called positive (for $g_1g_2 > 1$ or $G > 1$) and negative (for $g_1g_2 < 0$ or $G < -1$) branch, exhibiting external or internal focal points. Resonators with a defocusing mirror ($\rho_1 < 0$) and a cleaved output facet ($\rho_2 = \infty$) are unstable resonators in the positive branch of the stability diagram. This type of unstable resonator has an external focal point behind the back facet as shown in Fig. 2.

The focal point of this device is located in a distance of

$$S = \sqrt{\left(\frac{L}{2}\right)^2 - \frac{\rho_1 L}{2}} + \frac{L}{2}$$
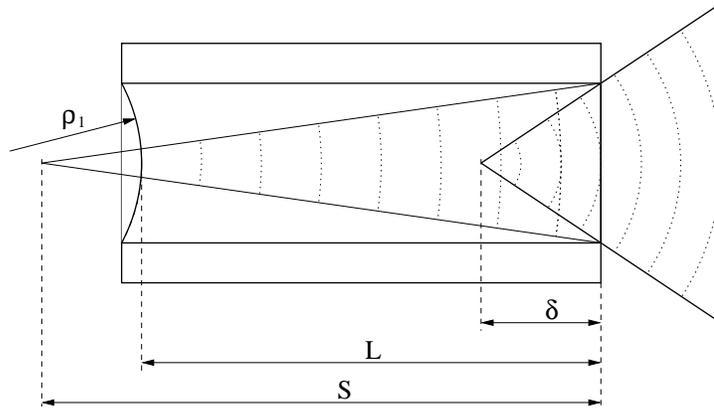
Fig. 2: Unstable resonator laser with a dry-etched back facet having a convex mirror curvature radius $\rho_1 < 0$ and a cleaved output facet $\rho_2 = \infty$. Also shown is the external focal point and the virtual source located in distances S and δ, respectively, behind the back facet.

behind the front facet. From this focal point, spherical wave fronts propagate towards the output mirror. After each round trip, the radius of curvature of these wave fronts is reproduced. However, due to the refraction at the output facet, the origin of the wave fronts seems to be a focal point inside the resonator, which is called the virtual source. This point is located in a distance of $\delta = S/n_{\text{eff}}$ behind the output facet. Since the origin of the horizontal and vertical far fields are separated by the distance δ, this type of semiconductor unstable resonator laser exhibits an astigmatism having a value of δ.

A magnified image of the virtual source can be measured in the plane of the corrected far field. For that purpose the output beam of the unstable resonator is collimated in the vertical direction using a lens with focal length f. The corrected far field can be imaged in a distance b behind the collimating lens. The size of the virtual source G_{vs} can be calculated from the size of the corrected far field B_{vs} with the lens equation $G_{\text{vs}} = B_{\text{vs}}f/(b-f)$. Additionally, the astigmatism $\delta = f^2/(b-f)$ of the device can be calculated.

To evaluate the brightness $B = P/(A\Omega)$ of these laser diodes, the optical output power P, the dimension of the emitting area A and the solid angle Ω needs to be known. The advantage of an unstable resonator is the small size of its virtual source combined with a wide output facet. Therefore, the risk of catastrophic optical mirror damage (COMD) is much smaller for unstable resonators compared to single-mode lasers leading to an increased brightness.

3. Fabrication

High-brightness unstable resonator lasers with good performance can only be realized with excellent epitaxial material, which is optimized for high-power cw operation. In

this study, a graded-index separate-confinement heterostructure (GRINSCH) grown with molecular-beam epitaxy (MBE) was used. The active region consists of an 8-nm-thick compressively strained $In_{0.20}Ga_{0.80}As$ single quantum well (SQW) which is surrounded by 10-nm-thick GaAs spacing layers followed by doped AlGaAs grading and cladding layers. The p- and n-dopants are C and Si, respectively. The emission wavelength is in the range of 980 nm and the internal efficiency of the epitaxial material is 78% with an intrinsic absorption of $2.1\,cm^{-1}$. The vertical far-field angle was measured to be $34°$ and $69°$ at full-width half maximum (FWHM) and $1/e^2$, respectively. Details of the epitaxial growth process are described in [7].

For the unstable-resonator laser diodes a tapered gain region is used. The tapered gain region is defined by wet-chemical etching of the highly p-doped surface layer. Lateral Ge absorbers can be introduced by etching down groves beside the active area to the quantum well followed by the evaporation and structuring of a thin Ge layer which acts as a strong absorber after annealing. A 250 nm-thick plasma-enhanced chemical-vapor-deposition (PECVD) SiN layer is used as surface passivation. The contact windows in this passivation layer are opened by CF_4 reactive ion etching (RIE). After the e-beam evaporation of Ti/Pt/Au as p-contact metalization, the contacts are structured with lift-off technique.

For the fabrication of the $8\,\mu m$-deep dry-etched curved mirror grooves, an optimized chemically-assisted ion-beam etching (CAIBE) process is used. Vertical, flat, and very smooth facets are achieved using a substrate temperature of $75\,°C$, an ion energy of $400\,eV$, and a chlorine flow of $4\,sccm$. Additionally, a multi-level resist is used as etch mask. AFM measurements show remaining roughnesses on the dry-etched facets of 3–5 nm (RMS). Details of this fabrication process are described in [3] and [8].

To achieve a better thermal behavior of the lasers, a $4\,\mu m$-thick gold layer can be electro-
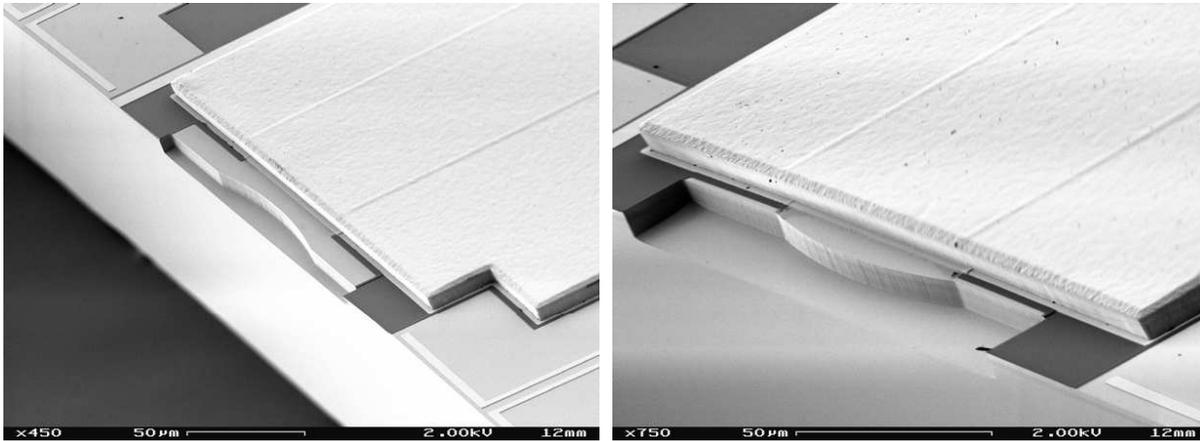
Fig. 3: SEM micrographs of dry-etched laser facets with the electroplated gold layer on top. The left picture shows a defocusing mirror ($\rho < 0$) with radius $-250\,\mu m$ and the right picture a focusing mirror ($\rho > 0$) with $250\,\mu m$ radius.

plated on top of the Ti/Pt/Au p-contact metalization, which provides good continuous wave (cw) operation with p-side-up mounted laser diodes. After wafer thinning, the n-contact is formed by Ge/Au/Ni/Au evaporation and annealing. As diffusion barriers, a thin Ti/Ni/Au top-metalization layer can be evaporated on top of the electroplated gold layer and the n-contact metalization. This has advantages concerning solder mounting techniques. Cleaved laser bars were mounted p-side-up on a copper submount. For high-power operation, the devices are AR/HR coated after cleaving and separated devices are soldered p-side-down on a diamond heat spreader.

The SEM micrographs of Fig. 3 show the dry-etched rear facets of an unstable-resonator lasers with $\pm 250\,\mu$m mirror curvature radius for a defocusing mirror with $\rho < 0$ (left picture) and a focusing mirror with $\rho > 0$ (right picture).

4. Characterization

The devices were AR/HR coated and soldered junction-side down on diamond heat spreaders. All results are measured in cw operation at $21\,°$C. The output powers refer only to the single output facet. The devices characterized in this section have a tapered resonator geometry, a resonator length L of $100\,\mu$m, a straight 200-μm-wide antireflection coated output facet, and a high-reflection coated defocussing mirror having curvature radii in the range of $\rho_1 = 255$–$2000\,\mu$m and widths of 67–$133\,\mu$m.
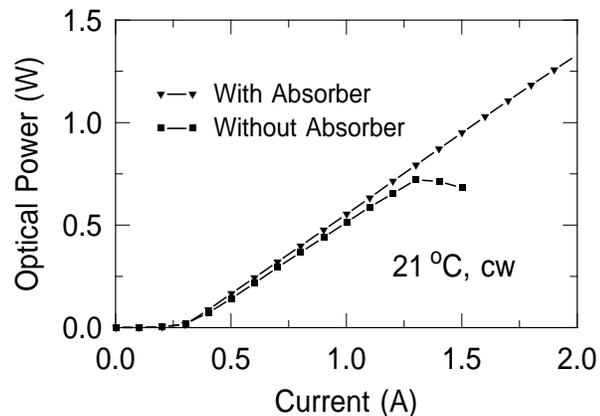
Fig. 4: *L–I* curves of lasers with and without absorbers. The curved mirror has radius of $2000\,\mu$m and a width of $133\,\mu$m, resulting in a magnification of $M = 3.7$, an equivalent G-parameter of $G = 2.0$, and an astigmatism of $\delta = 479\,\mu$m.

The advantage of lateral Ge absorbers can be demonstrated in Fig. 4 where the *L–I* curves of devices with and without absorbers are compared. At higher output power, a roll over for the device without absorbers is observed. Detailed examinations showed a parasitic laser oscillation perpendicular to the resonator direction. Such devices show very nice profiles for the lateral intensity distributions of the virtual source, which is shown in

Fig. 5 for different pump currents. There is a strong main lobe above threshold, however with a small side lobe on each side. The ratio of optical power in the main lobe is for all currents over 85 %.
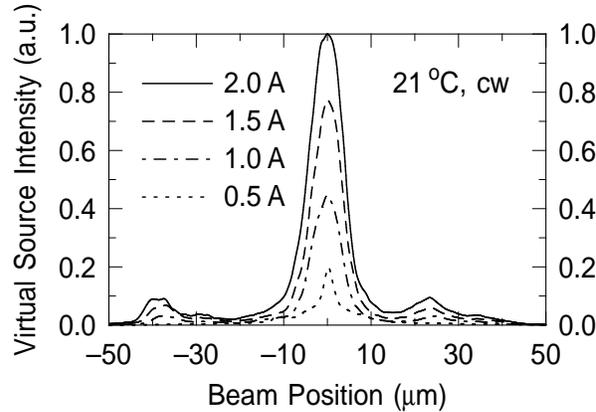
Fig. 5: Lateral intensity distribution of tapered unstable-resonator laser diode with lateral Ge absorbers. The curved mirror has radius of $500\,\mu$m and a width of $67\,\mu$m, resulting in a magnification of $M = 9.9$, an equivalent G-parameter of $G = 5.0$, and an astigmatism of $\delta = 357\,\mu$m.
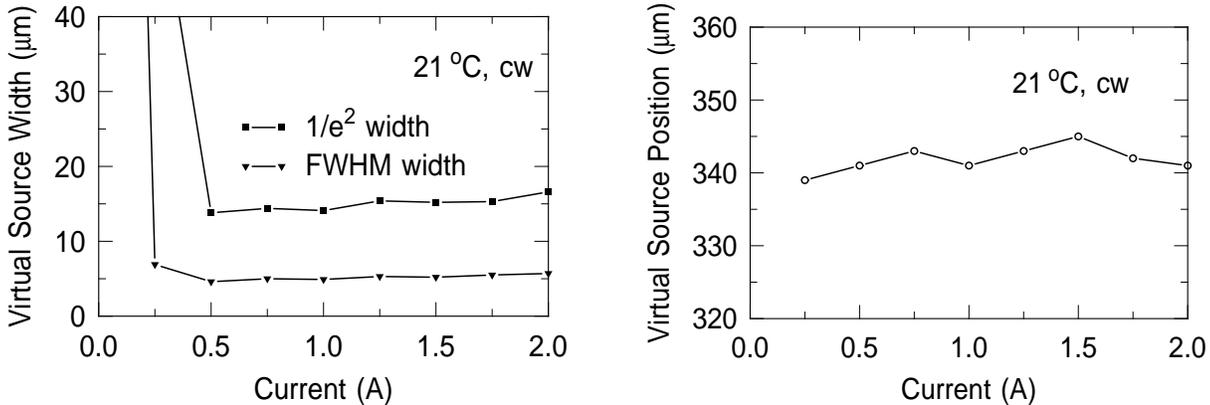
Fig. 6: Lateral size (left-hand side) and position (right-hand side) of the virtual source at FWHM and $1/e^2$ for the device shown in Fig. 5.

In Fig. 6, the lateral size and the position of the virtual source is shown. Above threshold, the lateral size remains almost constant and shows values of 5 and $15\,\mu$m at FWHM and $1/e^2$, respectively. The position of the virtual source which determines the astigmatism of the device is located between 340 and $345\,\mu$m behind the front facet and is almost constand for all pump currents. The measured results are in good agreement with the theoretical value of $357\,\mu$m.

To determine the brightness of this unstable resonator laser diode, the lateral beam quality was measured using the above described technique. A value of $\mathcal{M}^2 = 2.4$ is achieved when

neglecting the side lobes, which means that only the intensity in the main lobe (85 % of the total output power) is taken. With a collimated output power of 1.5 W at 2.5 A and the wavelength of 980 nm, the brightness is 150 MW/(cm²sr) in cw operation at 21 °C.

5. Fiber Coupling

To couple light from unstable cavity laser diodes into a fiber, a lens system with 3 lenses can be used [9, 10]. A first lens collimates the output beam in vertical direction. The second lens is a cylindrical lens to collimate the beam in horizontal direction and to correct the astigmatism. With the third lens, the light is coupled into the fiber. All lenses need to be chosen properly to match the properties of the unstable resonator device and the fiber. Using the unstable laser device, the coupling efficiencies into single-mode fibers with a core diameter of 5.9 μm were below 30 %, since the size of the virtual source is too large. However, if a fiber with 25 μm core diameter (Crystal Fibre MM-HNA-25) is used, much better coupling efficiencies can be achieved. Figure 7 shows the *L–I* curve of the fiber coupled unstable resonator with more than 1 W in the fiber at a pump current of 2 A in cw operation. The coupling efficiency is in the range of 80 % for all pump currents and is mainly limited by reflection losses.
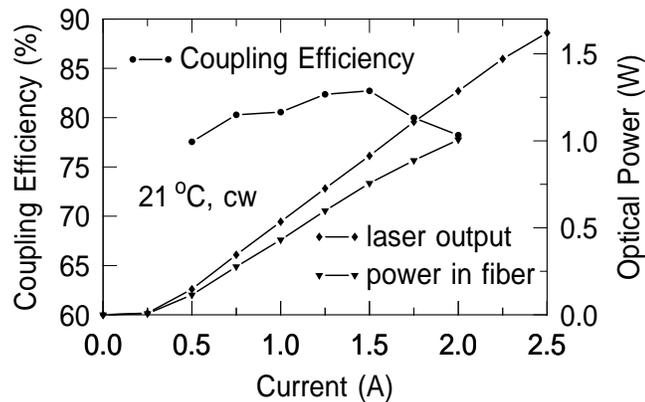
Fig. 7: Fiber coupling of an unstable resonator laser into a 25-μm-core fiber. The device design is identical to the design of the devices characterized in Figs. 5 and 6.

References

[1] S.A. Biellak, C.G. Fanning, Y. Sun, S.S. Wong, and A.E. Siegman, "Reactive-ion-etched diffraction-limited unstable resonator semiconductor lasers," *IEEE J. Quantum Electron.*, vol. 33, no. 2, pp. 219–230, 1997.

[2] P. Unger, V. Boegli, P. Buchmann, and R. Germann, "Fabrication of curved mirrors for visible semiconductor lasers using electron beam lithography and chemically assisted ion-beam etching," *J. Vac. Sci. Technol. B*, vol. 11, no. 6, pp. 2514–2518, 1993.

[3] E. Deichsel, F. Eberhard, R. Jäger, and P. Unger, "High-power laser diodes with dry-etched mirror facets and integrated monitor photodiodes," *IEEE J. Select. Topics Quantum Electron.*, vol. 7, no. 2, pp. 106–110, 2001.

[4] P. Vettiger, M.K. Benedict, G.-L. Bona, P. Buchmann, E.C. Cahoon, K. Dätwyler, H.-P. Dietrich, A. Moser, H.K. Seitz, O. Voegeli, D.J. Webb, and P. Wolf, "Full-wafer technology — A new approach to large-scale laser fabrication and integration," *IEEE J. Quantum Electron.*, vol. 27, no. 6, pp. 1319–1331, 1991.

[5] A. E. Siegman, *Lasers*, Mill Valley, CA: University Science Books, 1986.

[6] N. Hodgson and H. Weber, *Optical Resonators*, Berlin Heidelberg: Springer, 1997.

[7] R. Jäger, J. Heerlein, E. Deichsel, and P. Unger, "63% wallplug efficiency MBE grown InGaAs/AlGaAs broad-area laser diodes and arrays with carbon p-type doping using CBr$_4$," *J. Crystal Growth*, vol. 201/202, pp. 882–885, 1999.

[8] E. Deichsel, R. Jäger, and P. Unger, "High-brightness semiconductor lasers fabricated with improved dry-etching technology for ultra-smooth laser facets," *Digest of Papers, Microprocess and Nanotechnology Conference 2001*, pp. 218–219, 2001

[9] P. Salet, F. Gérard, T. Fillion, A. Pinquier, J.-L. Gentner, S. Delepine, and P. Doussière, "1.1 W continuous-wave 1480-nm semiconductor lasers with distributed electrodes for mode shaping" *IEEE Photon. Technol. Lett.*, vol. 10, no. 12, pp. 1706–1708, 1998.

[10] S. Delépine, F. Gérard, A. Pinquier, T. Fillion, J. Pasquier, D. Locatelli, J.P. Chardon, H.K. Bissessur, N. Bouché, F.R. Boubal, and P. Salet, "How to lounch 1 W into single-mode fiber from a single 1.48-µm flared resonator" *IEEE J. Select. Topics Quantum Electron.*, vol. 7, no. 2, pp. 111–123, 2001.

Epitaxy and Structural Characterization of 980 nm Semiconductor Disk Lasers

Fernando Rinaldi

The description of the epitaxial processes to obtain semiconductor disk lasers is presented. Optical and structural analyses are briefly described in order to have a better understanding of the grown structure. Different samples are studied, to better enhance the different properties of this special disk laser design. Emphasis is placed to HRXRD (high resolution X-ray diffraction) as a very flexible and non destructive characterization tool.

1. Introduction

The steps for the production of 980 nm disk lasers on a MBE system are described. This device is composed of a Bragg mirror and an active area which consists of 6 InGaAs/GaAs QWs sandwiched between pump-light absorbing layers. The mirror used is not only the bottom side of the optical cavity, but it is also reflecting the transmitted part of the 808 nm pump radiation back into the active region to improve the absorption efficiency. This is achieved with a special mirror design. Attention is focused on the methods used to have a good control on the layer parameters which allows us to produce good devices. Some problems regarding the QWs' quality are deeply discussed. The samples were grown at 580°C except in the QWs' regions where the temperature was lowered to 510°C.

2. Calibration Samples

For the calibration of the indium content, a sample with 3 InGaAs QWs was grown. The three QWs are separated by 10 nm thick GaAs barriers and the whole structure is confined between two 200 nm thick $Al_{0.5}Ga_{0.5}As$ layers. On the surface, a 40 nm GaAs top layer prevents the sample from oxidation. The HRXRD rocking curve of this sample is shown in Fig. 1. Not only the indium content and thickness of the QWs can be estimated to be 15.5% and 7.5 nm respectively, but also the thickness and composition of the confinement layers can be accurately checked, e.g. the fast modulation in the rocking curve stems from the 200 nm thick $Al_{0.5}Ga_{0.5}As$ layers. It is interesting to note that the fringes go out of phase on the large angle side in Fig. 1, while the intensity matches perfectly the simulation. This phenomenon is well known in the AlGaAs/GaAs system [1] and it is due to the presence of a nanometric transition layer between $Al_{0.5}Ga_{0.5}As$ and GaAs and they were not been taken into account in the simulation. The maximum of the photoluminescence peak at room temperature appears at about 960 nm in perfect agreement with [2], if the estimated QWs' thickness and composition values are used.
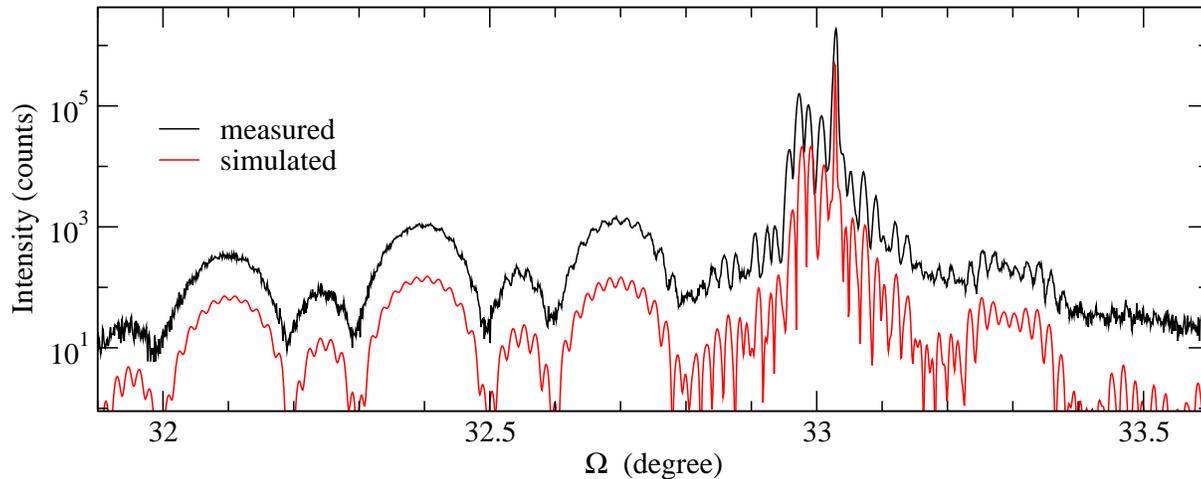
Fig. 1: HRXRD (004) reflection rocking curve of the photoluminescence calibration sample.

3.   Normal and Inverted Disk Laser Structures

In a normal disk laser structure the Bragg mirror is grown first followed by the active region which consists of 6 InGaAs/GaAs QWs. To improve the heat extraction, the sample can be grown in the inverted way starting with the QWs and following with the mirror, the substrate is then removed completely. In Fig. 2, the HRXRD rocking curve on a normal sample is shown. Looking carefully to the measured curve it can be noticed that the fringes due to the 6 fold repeated QW structure are double-peaked. This effect was simulated in the diagram with a change of 2% in the thickness in the last 2 QWs. During flux measurements, sometimes an abrupt change of the gallium flux was observed. It is interesting to see that HRXRD is sensitive to this kind of problem. In Fig. 3, the same
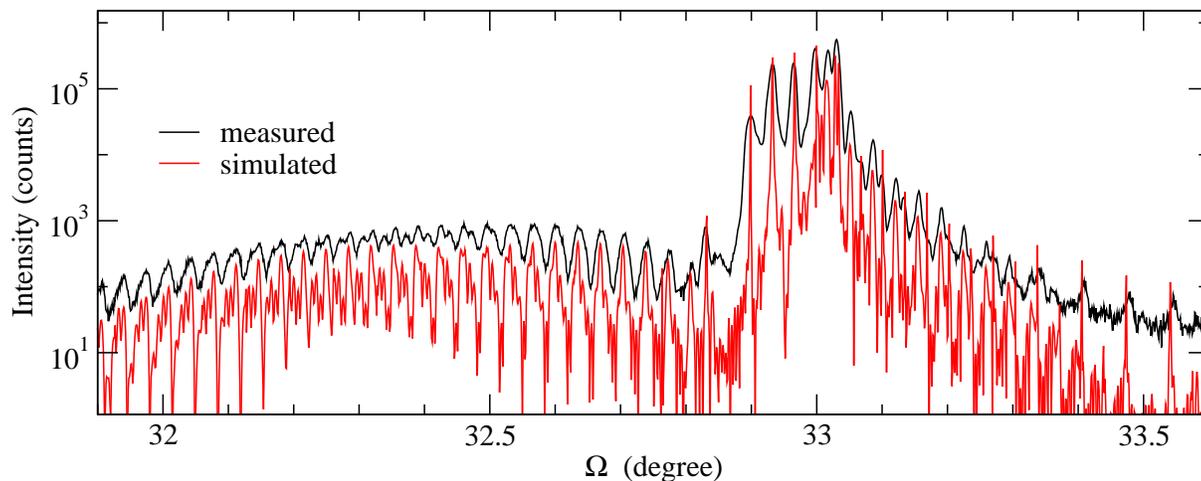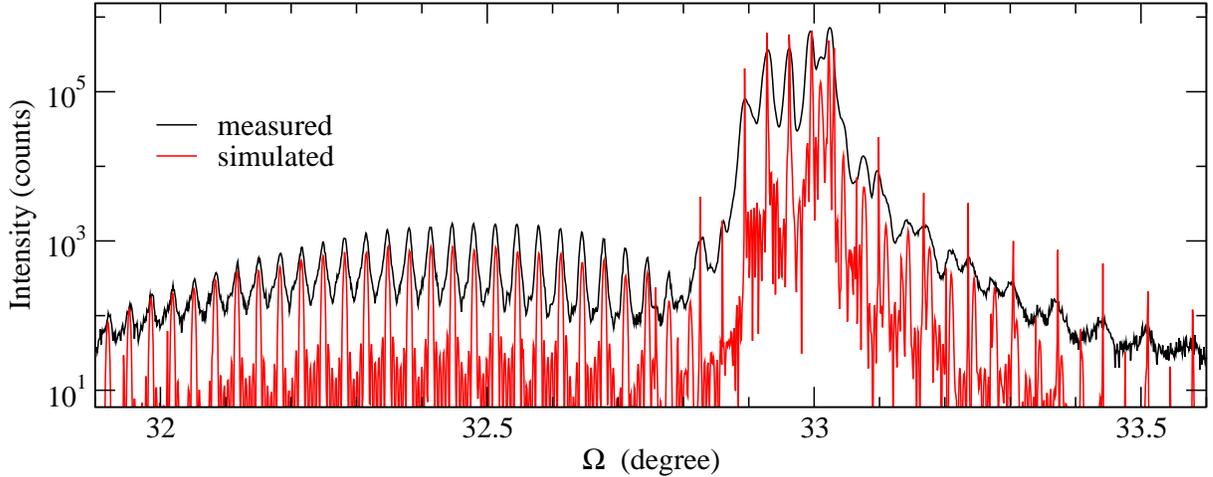

Fig. 2: HRXRD (004) reflection rocking curve of the normal sample.

Fig. 3: HRXRD (004) reflection rocking curve of the inverted sample.

scan on an inverted sample is shown. The spectrum shows single-peaked satellites. In this case, there was no gallium flux change during the QWs' growth. For both samples the content of indium is 15.0% and the QWs' thickness is 8.5 nm. The mirror is composed of 33 pairs of $Al_{0.2}Ga_{0.8}As/AlAs$ layers. The layer sequence and the numerically calculated layer thickness are shown in Fig. 4. The pairs are not identical. The thickness of the
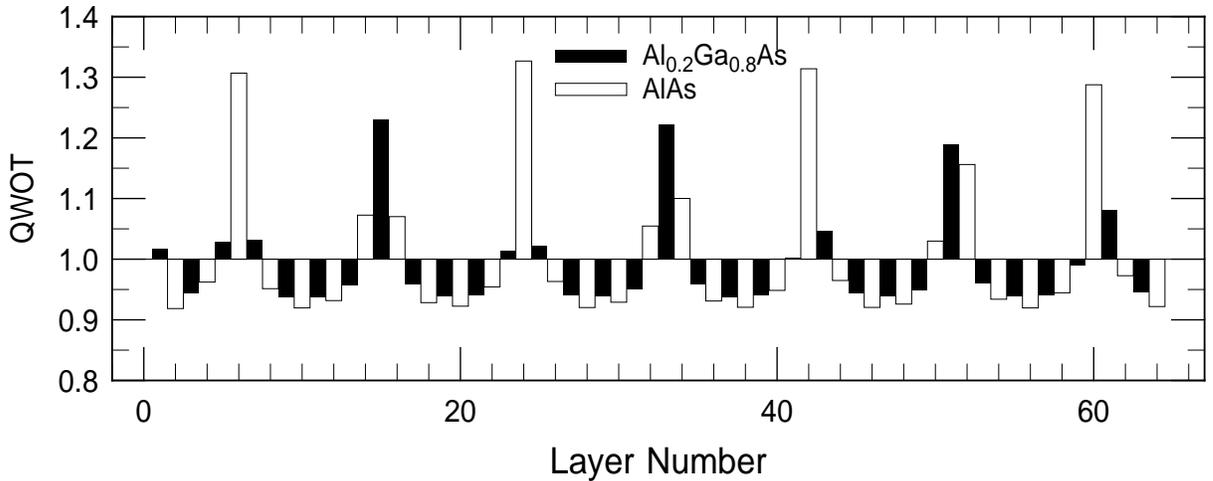
Fig. 4: Layer thickness scheme expressed in terms of QWOT (quarter wavelength optical thickness).

pairs is almost a QWOT (quarter wavelength optical thickness) for the lasing wavelength. Additionally there is an overperiodic modulation of the layer thickness which account for a second stop band for the reflection of the pump beam. In the HRXRD simulations, the mirrors pairs were treated as a 33 fold periodic structure, so that in Fig. 2 and in Fig. 3 we can see that the simulated lines have very sharp satellites peaks. In the measured

spectra of course, these peaks are strongly smoothed. In Fig. 5 the reflectivity spectrum of an inverted sample is shown. The main stop band is centered at about 980 nm and a second one at about 805 nm. The photoluminescence spectrum in Fig. 6 was recorded after mounting and substrate removal so that the QWs were on the top. The maximum emitted intensity is at about 970 nm in order to lase at 980 nm in working conditions.
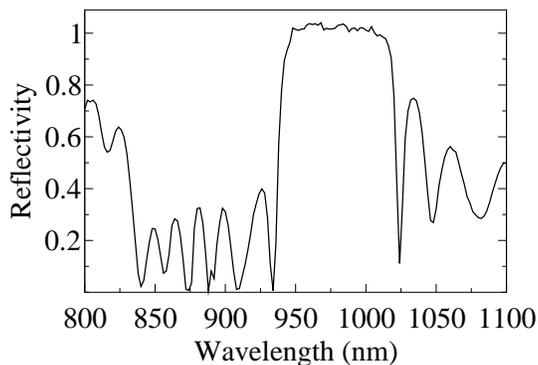
Fig. 5: Measured reflectivity spectrum that shows the presence of two stop bands.
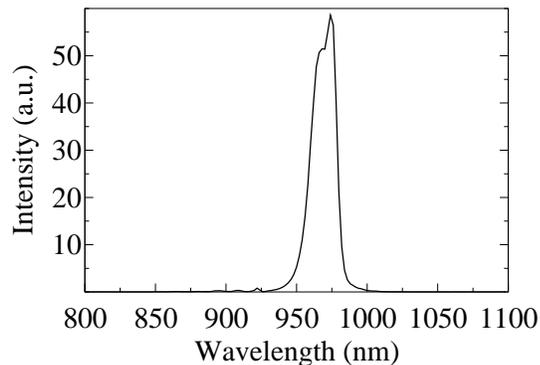
Fig. 6: Photoluminescence spectrum of the inverted sample (pump radiation 514 nm).

4. Pyrometer Signal Analysis

The pyrometer signal was recorded during growth. The pyrometer detects the thermal radiation which is emitted approximately normally from the surface of the sample. The instrument is sensitive in the band $\lambda_P = (0.94 \pm 0.03)\,\mu m$ and the emissivity is calibrated observing the GaAs oxide desorption with RHEED at 580°C. The interpretation of the pyrometer signal is not straightforward. The absorption depth for GaAs at λ_P is $\approx 1\,\mu m$. So in our case (where the layers are ≈ 100 nm thick) the pyrometer oscillations depend strongly on the underlying layer structure in a very complicated way [3, 4]. In case of Bragg reflectors composed of repeated pairs of quarter wavelength layers, the periodicity and the limited penetration depth force the pyrometer signal to be periodic. These conditions are not fullfilled with our reflectors (Fig. 4) where the structure is not periodic. However, the relative pyrometer signal in Fig. 7 shows a peculiar form that makes unwanted variation in the growth rates detectable.

5. Morphology

The morphology of the samples is now considered. In all the samples, a crosshatched surface is observed in Nomarski constrast micrographs. This is a clear sign that relaxation occurred. In Fig. 8, the Nomarski image of one sample at a magnification of 200 shows the crosshatched surface. The surface looks really smooth and the crosshatched pattern is almost invisible, Fig. 8 is the product of image processing to enhance the constrast as
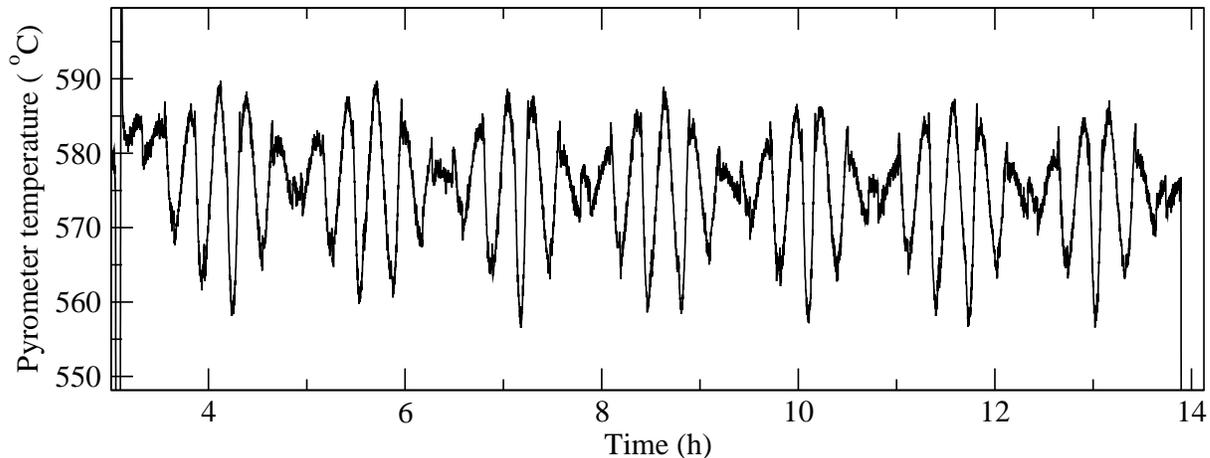
**Fig. 7:** Pyrometer signal of a double stop band mirror.

much as possible. As already observed for InGaAs/GaAs QWs [5], the relaxation is due to 60° misfit dislocations that are asymmetrically distributed. Also in our case, the [110] direction is slightly preferred to the [1$\bar{1}$0] one. In the picture, the difference is increased due to the anisotropic lighting. The distance between two lines can be roughly estimated to about 10 μm. This can provide a quantitative estimation for the value of the relaxation. In fact, assuming that in this system the dislocations are entirely of the 60° type [6], we can write

$$\left(\frac{\Delta a}{a}\right)_{\parallel} = Db \qquad \text{with } b = \frac{a}{2\sqrt{2}}, \tag{1}$$

where the QWs' in-plane mismatch is calculated from the density of dislocation per unity length D and the length of the in-plane component of the considered Burgers vector b; a is the GaAs lattice parameter. The relaxation can be easily calculated to $r = 0.1 - 0.2\%$. In Fig. 9 the reciprocal space map of the same sample is shown. The peaks of substrate and QWs are perfectly aligned, which is typical for this kind of structures, where the relaxation is spatially localized at the misfit in the dislocation region. It is not distributed all over the layer. It is important to note that other groups have found no sign for relaxation growing similar structures [5].

6.   Conclusion

We grown 980 nm disk lasers with 6 InGaAs QWs . The devices show good performances with more than 3.0 W at −20°C and 1.8 W at 10°C with more than 30% conversion efficiency. Despite this good results, the lifetime of the devices is short because degradation occurs presumably due to the misfit dislocations originating in the QWs. Future work will be done to optimize the growth conditions, to reduce the dislocation density, and to improve the device lifetime. Also strain compensation will be investigated. HRXRD will be used extensively to extract structural informations.
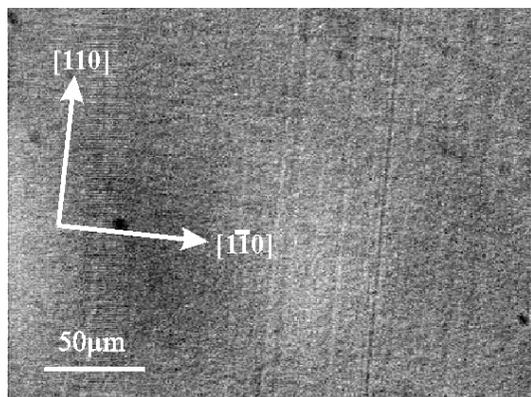
Fig. 8: Nomarsky contrast micrograph of a sample after computer elaboration. The crosshatched surface is visible with 200 magnification.
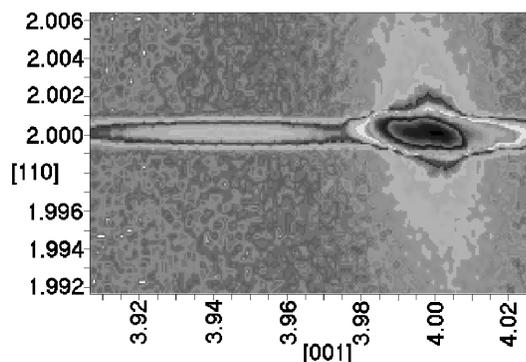
Fig. 9: Measured (224)+ HRXRD reciprocal space map of a sample. The structure is pseudomorphic.

References

[1] P.F. Fewster, *X-ray scattering from semiconductors.* London: Imperial College Press, 2000.

[2] M. Kudo and T. Mishima, "Improved photoluminescence properties of highly strained InGaAs/GaAs quantum wells grown by molecular-beam epitaxy," *J. Appl. Phys.*, vol. 78, no. 3, pp. 1685–1688, 1995.

[3] H.P. Lee, E. Ranalli, and X. Liu, "Physical modeling of pyrometric interferometry during molecular beam epitaxial growth of III-V layered structures," *Appl. Phys. Lett.*, vol. 13, no. 67, pp. 1824–1826, 1995.

[4] J. Muszalski, "Pyrometric interferometry during MBE growth of laser heterostructures," *Thin Solid Films*, no. 367, pp. 299–301, 2000.

[5] C.A. Wang, S.H. Groves, J.H. Reinold, and D.R. Calawa, "Critical layer thickness of strained-layer InGaAs/GaAs multiple quantum wells by double-crystal X-ray diffraction," *J. Electron. Mat.*, vol. 22, no. 11, pp. 1365–1368, 1993.

[6] K.L. Kavanagh, M.A. Capano, L.W. Hobbs, J.C. Barbour, P.M.J. Meree, W. Schaff, J.W. Mayer, D. Pettit, J.M. Woodal, J.A. Stroscio, and R.M. Feenstra, "Asymmetries in dislocation densities, surface morphology, and strain of GaInAs/GaAs single heterolayers," *J. Appl. Phys.*, vol. 64, no. 10, pp. 4843–4852, 1988.

Polarization Control of VCSELs

Johannes Michael Ostermann and Michael C. Riedl

A dielectric surface grating has been used to control the polarization of VCSELs. This grating is etched into the surface of top-emitting VCSELs. Its influence on the polarization depends strongly on the grating parameters like period and etching depth. With optimized parameters one can suppress the orthogonal polarization by 15 dB, even for highly multi-mode devices. By combining the surface grating with the well-known surface relief technique, we have fabricated first devices having high single-mode output power and stable polarization at the same time.

1. Introduction

Because of the cylindrical symmetry of their resonator, the isotropy of their gain — in case of the usual growth on [100]-oriented substrates — and the polarization independent reflectivity of their Bragg mirrors, VCSELs have a priori no preferred polarization. Only due to the electro-optic effect, which is caused by external and internal electric fields, the [011]- and the [0$\bar{1}$1]-crystal axes are favored polarization directions [1]. With a change of the driving current, a change of the laser temperature or with externally applied stress, the polarization of VCSELs often abruptly changes its orientation from one preferred crystal axis to the other. This is a so-called polarization switch [2].

These polarization switches increase the noise in optical communication links and inhibit the usage of VCSELs in systems with polarization-sensitive optical elements. Because a polarization switch is, due to the electro-optic effect, always connected with a change of the emission wavelength, one needs polarization-stable VCSELs for spectroscopic applications. This is why several attempts were made and are still made to control the polarization of VCSELs. These attempts can be divided into five groups: the usage of non-isotropic gain, e.g. by growing on substrates with higher indices [3], non-cylindrical resonators [4], external feedback [5], externally applied stress [6], or mirrors with a polarization dependent reflectivity [7]. By using metal or metal-interlaced gratings on top of one mirror of a VCSEL one can achieve different reflectivities for both polarizations [8], [9]. P. Debernardi et al. [10] could recently show with fully-vectorial, three-dimensional simulations of the electromagnetic properties of VCSELs that one expects a better polarization control if one uses a dielectric surface grating instead of a metallic one [11]. These calculations also show that the dichroism (difference between the threshold gains for the two polarizations) strongly depends on the grating parameters such as period and etching depth.

2. Fabrication

According to the calculations of P. Debernardi we have fabricated VCSELs with a dielectric surface grating. The wafer was grown by standard solid-source molecular beam epitaxy. The emission wavelength varies between 920 and 980 nm over the wafer due to a variation of the layer thickness from the center of the wafer to its edge. The active region consists of three InGaAs/GaAs quantum wells. 19 Bragg pairs form the top mirror of the top-emitting, oxide-confined VCSELs. The top mirror is terminated by a $3/4\,\lambda$ thick layer of GaAs, in which the grating was etched. Because the simulations have shown that the effect of the surface grating strongly depends on its parameters, we varied the grating period between 0.89 and 1.25 μm to account for differences between theory and experiment and for fabrication tolerances. The etching depth of the grating is approximately 21 nm for all devices on that wafer. For the fabrication we used a self-aligning technique in which the grating and the mesa were defined in one lithographical step. A scanning electron microscopy picture of a completely processed VCSEL with a surface grating is shown on the left-hand side of Fig. 1. To achieve high single-mode output power with a well defined polarization we tried to combine the surface grating with the surface relief as is shown on the right-hand side of Fig. 1. In that case, the grating is only defined in a small circle in the middle of the outcoupling aperture of a VCSEL. Outside of the relief, the cap-layer of the VCSEL is etched down by the same amount as the grating grooves.
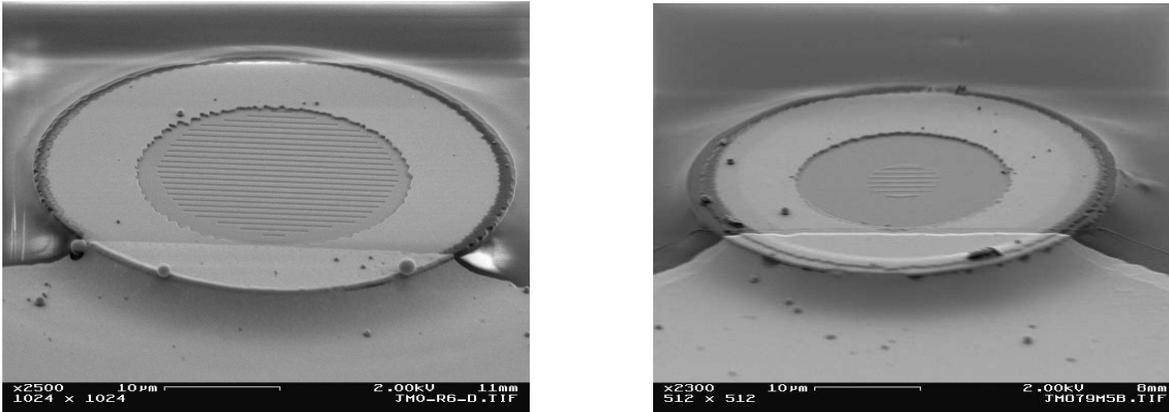
Fig. 1: Scanning electron microscope pictures of VCSELs with a dielectric surface grating. The grating is etched into the cap-layer of standard VCSELs. While the VCSEL on the left-hand side has a grating across the whole outcoupling aperture, in the case of the VCSEL on the right-hand side the grating is only defined in a circular ring in the center of its outcoupling aperture. Outside of that circle, the cap-layer is etched to the same depth as the grating grooves.

3. Defining One Stable Polarization for All Modes of a VCSEL

To be able to evaluate the effect of a dielectric surface grating we fabricated VCSELs with and without a surface grating adjacent to each other on the same sample. In Fig. 2
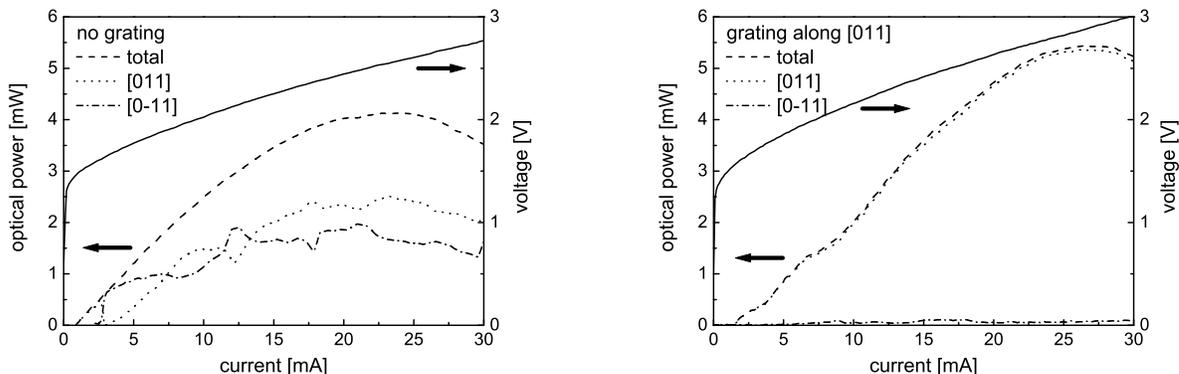
Fig. 2: Two nominally identical VCSELs fabricated adjacent to each other (separated by 250 μm) on the same sample without (left) and with (right) a dielectric surface grating. While the output power of the VCSEL without a surface grating is approximately evenly distributed between the two polarizations, the VCSEL with the dielectric surface grating has one stable polarization for all modes up to thermal rollover. Both VCSELs have an active diameter of 8 μm. The surface grating has a period of 1.0 μm and an etching depth of 21 nm.

we compare two of these nominally identical VCSELs, separated by 250 μm on the same sample. The only difference is that the VCSEL on the left-hand side has no surface grating while the VCSEL on the right hand side has one. The VCSEL without a surface grating has a threshold of 1 mA and a maximum output power of 4.1 mW. At a driving current of 2.7 mA a polarization switch occurs. For higher currents the output power of the VCSEL is approximately evenly distributed between the two polarizations. In contrast to the polarization behavior without a surface grating, the VCSEL with a dielectric surface grating on the right-hand side has one stable polarization parallel to the grating for all modes all the way up to thermal rollover. At maximum up to 14 modes are lasing. The increase of the threshold current to 1.5 mA and the increase of the maximum output power to 5.4 mW can be explained by the decrease of the overall reflectivity of the top mirror caused by the surface grating and some fabrication tolerances for the active diameter. The slight increase of the voltage is probably also due to some processing tolerances.

Six VCSELs from the same sample and with the same grating parameters but with different active diameters are shown in Fig. 3. The active diameter is varied from 3.5 to 15.5 μm. According to that, also the maximum output power varies from 2 to 10 mW. Nevertheless the orthogonal polarization suppression ratio (OPSR), which is defined as the ratio of the power of the two polarizations, exceeds 13 dB for all VCSELs up to thermal rollover. For some VCSELs it is even well above 15 dB.

4. Combination of Surface Grating and Surface Relief

To increase the maximum single-mode output power and to define and stabilize the polarization at the same time, we made first attempts to combine the surface grating with the
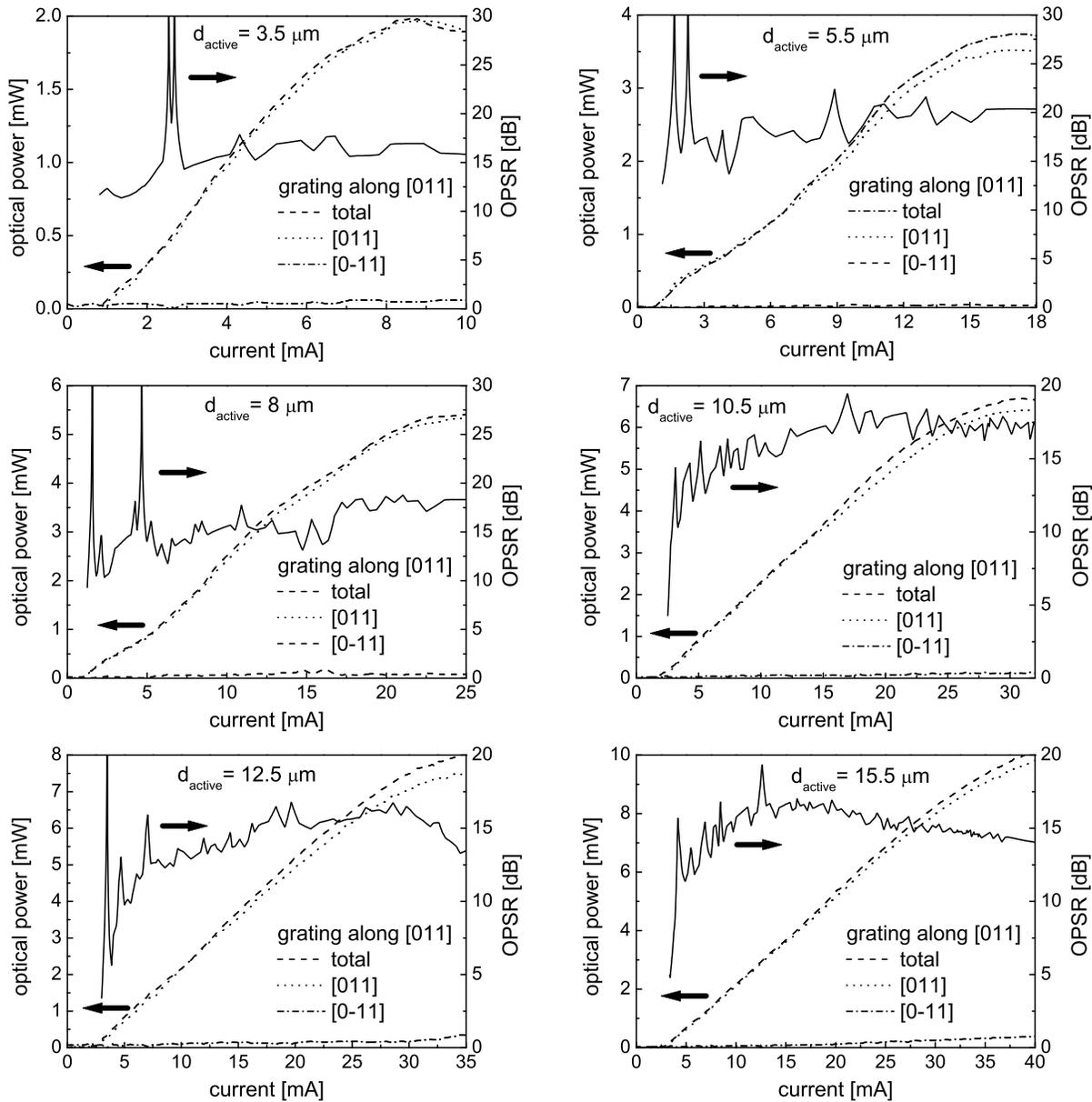
Fig. 3: Six VCSELs from the same sample having a surface grating with a grating period of $1.0\,\mu m$ and a grating depth of 21 nm. Their active diameter is varied from 3.5 to $15.5\,\mu m$. All VCSELs have an orthogonal polarization suppression ratio (OPSR) of well above 13 dB.

surface relief technique as described in Sect. 2. But due to some problems in the exposure of these structures with the electron beam microscope, these structures are not optimized and the fabrication of the grating worked only for some of these VCSELs. Nevertheless we can see a clear influence of the grating relief as is shown in Fig. 4. On the left-hand side a VCSEL with an active diameter of $5.5\,\mu m$ is shown. Its maximum single-mode output power of 1.2 mW is reached at 4.5 mA, while its polarization is parallel to the [011]
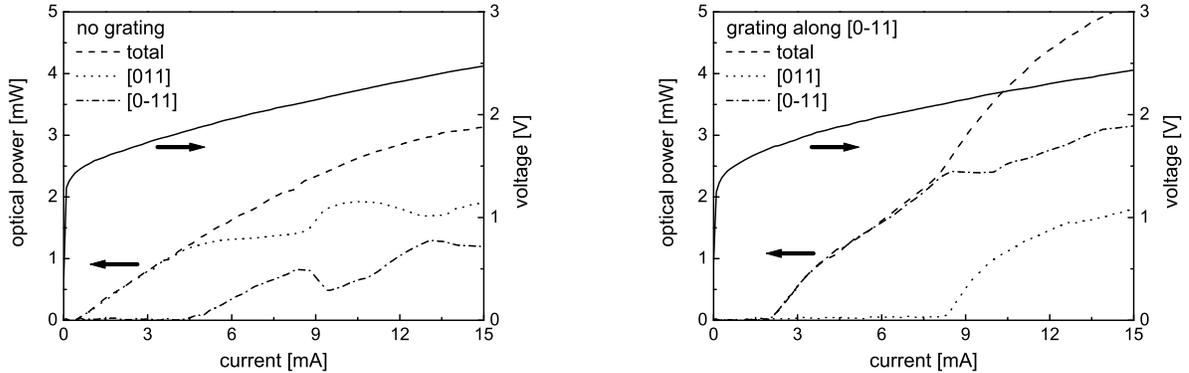
Fig. 4: In this figure we compare again a VCSEL without a surface grating (left) with a VCSEL with a surface grating (right). Both VCSELs are processed on the same sample and have the same active diameter of 5.5 µm. The VCSEL on the right-hand side has a grating relief with a diameter of 5.5 µm to increase the single-mode output power while defining and stabilizing the polarization.

crystal axis. On the right-hand side a VCSEL with the same active diameter, but with a grating relief is shown. The grooves of the grating are oriented along the $[0\bar{1}1]$ crystal axis, the period of the grating is 1 µm and its etching depth is 21 nm. The diameter of the relief is 5 µm. Through the relief, the maximum single-mode output power is doubled in comparison with the VCSEL without a grating relief to 2.4 mW at a current of 8.3 mA. While the polarization of the VCSEL without the surface grating is oriented along the [011] crystal axis, the polarization of the VCSEL with the surface grating is parallel to the grooves of the grating and therefore oriented along its direction. This is a clear evidence of the influence of the surface grating. Due to its limited extent, the surface grating has no influence on higher order modes.

5. Conclusion

We have shown that the polarization of VCSELs can be controlled by a dielectric surface grating which is etched into the outcoupling aperture of the VCSEL. With this technique one can not only inhibit polarization switches, but one can also define one stable polarization direction for all modes up to thermal rollover, even for highly multi-mode devices. No serious drawback caused by the dielectric surface grating is seen for the overall laser performance.

References

[1] M.P. van Exter, A.K. Jansen van Doorn, and J.P. Woerdman, "Electro-optic effect and birefringence in semiconductor vertical-cavity lasers," *Phys. Rev. A*, vol. 56, no. 1, pp. 845–853, 1997.

[2] J. Danckaert, B. Nagler, J. Albert, K. Panajotov, I. Veretennicoff, and T. Erneux, "Minimal rate equations describing polarization switching in vertical-cavity surface-emitting lasers," *Optics Communications*, vol. 201, no. 1–3, pp. 129–137, 2002.

[3] N. Nishiyama, A. Mizutani, N. Hatori, M. Arai, F. Koyama, and K. Iga, "Lasing characteristics of InGaAs-GaAs polarization controlled vertical-cavity surface-emitting laser grown on GaAs (311)B substrate," *IEEE J. Selected Topics Quantum Electron.*, vol. 5, no. 3, pp. 530–536, 1999.

[4] K.D. Choquette and R.E. Leibenguth, "Control of vertical-cavity laser polarization with anisotropic transverse cavity geometries," *IEEE Photon. Technol. Lett.*, vol. 8, no. 1, pp. 40–42, 1994.

[5] C.I. Wilkinson, J. Woodhead, J.E.F. Frost, J.S. Roberts, R. Wilson, and M.F. Lewis, "Electrical polarization control of vertical-cavity surface-emitting lasers using polarized feedback and a liquid crystal," *IEEE Photon. Technol. Lett.*, vol. 11, no. 2, pp. 155–157, 1999.

[6] F. Monti di Sopra, M. Brunner, and R. Hövel, "Polarization control in strained T-bar VCSELs," *IEEE Photon. Technol. Lett.*, vol. 14, no. 8, pp. 1034–1036, 2002.

[7] H.J. Unold, M.C. Riedl, R. Michalzik, and K.J. Ebeling, "Polarisation control in VCSELs by elliptic surface etching," *Electron. Lett.*, vol. 38, no. 2, pp. 77–78, 2002.

[8] C.-A. Berseth, B. Dwir, I. Utke, H. Pier, A. Rudra, V.P. Iakovlev, E. Kapon, and M. Moser, "Vertical cavity surface emitting lasers incorporating structured mirrors patterned by electron-beam lithography," *J. Vac. Sci. Technol. B*, vol. 17, no. 6, pp. 3222–3224, 1999.

[9] J.-H. Ser, Y.-G. Ju, J.-H. Shin, and Y.-H. Lee, "Polarization stabilization of vertical-cavity top-surface-emitting lasers by inscription of fine metal-interlaced gratings," *Appl. Phys. Lett.*, vol. 66, no. 21, pp. 2769–2771, 1995.

[10] G.P. Bava, P. Debernardi, and L. Fratta, "Three-dimensional model for vectorial fields in vertical-cavity surface-emitting lasers," *IEEE J. Selected Topics Quantum Electron.*, vol. 9, no. 3, pp. 905–917, 2003.

[11] P. Debernardi and G.P. Bava, "Coupled mode theory: a powerful tool for analyzing complex VCSELs and designing advanced device features," *Phys. Rev. A*, vol. 63, no. 2, pp. 023816/1–13, 2001.

Polarization-Resolved Output Characteristics of InAlGaAs VCSELs under Anisotropic Strain

Andrea Kroner and Johannes Michael Ostermann

We present a setup that enables direct examination of the correlation between wavelength, polarization suppression and induced strain in vertical-cavity surface-emitting laser (VCSEL) samples by applying a defined amount of external stress. In addition to measurements on standard oxide-confined VCSELs, devices with a dielectric surface grating have been investigated, showing an outstanding stability of the linear light output polarization.

1. Introduction

Due to anisotropies introduced by the electro-optic effect, the polarization components of most conventional VCSELs are oriented along the [011] or [0$\bar{1}$1] crystal axes [1]. However, the polarization behavior of a VCSEL is also influenced by internal strain, which has various origins and differs from device to device. Since strain modifies the band structure of a crystal material, a change of the material gain in different crystal axes has to be expected [2]. Furthermore, it leads to an anisotropy of the refractive index due to the elasto-optic effect [3].

A strong birefringence, i.e. a splitting between the refractive indices along the [011] and [0$\bar{1}$1] crystal axes, is achieved by applying a tensile strain in the [011] or [0$\bar{1}$1] direction. If strain is induced along the [011] crystal axis, the refractive index in [011] direction will increase while the refractive index along the [0$\bar{1}$1] crystal axis decreases due to the negative elasto-optic coefficient of GaAs [4]. Therefore, the [011] polarization will have a longer wavelength than the [0$\bar{1}$1] polarization. On the other hand, strain applied along the [0$\bar{1}$1] orientation will usually lead to a shorter wavelength of the [011] polarization.

To examine the impact of strain on the polarization behavior of VCSELs, mainly on polarization switches, polarization-dependent measurements under external stress have been performed in the past [5]. In the present work a special holder was designed to create reproduceable, external stress in a sample, that enables direct examinations of the correlation between wavelength, polarization suppression and induced strain.

2. Setup for Stress-Dependent Measurements

The left hand side of Fig. 1 shows a sketch of the designed sample holder. The wafer is fixed with a clamp to the bottom plate and it is possible to bend the sample at the edge
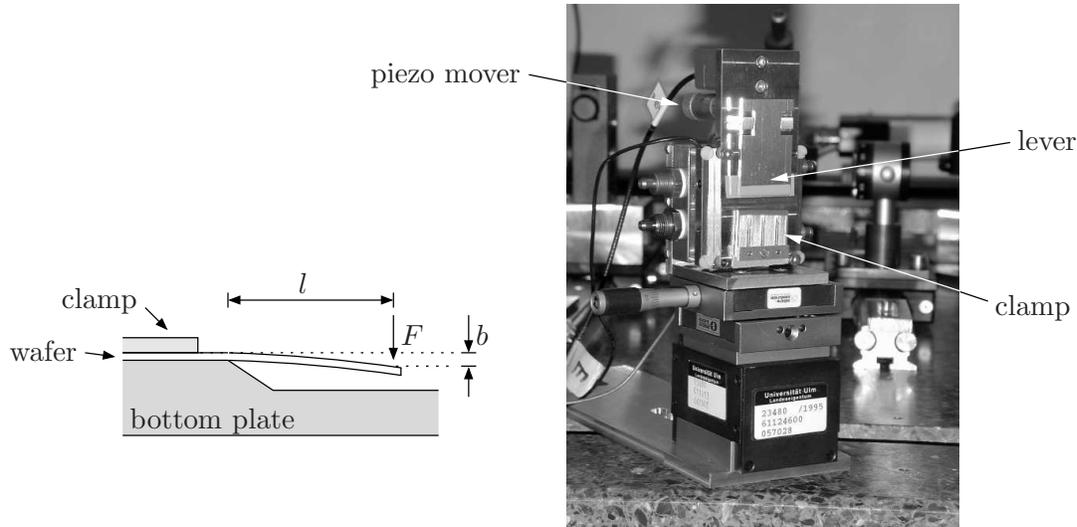
Fig. 1: Holder designed to bend a wafer sample in a reproduceable way. The wafer is fixed by a clamp and bent over an edge of the bottom plate.

of that plate. If a force F is applied at a distance l from the edge, the sample is deflected by an amount b.

The photograph on the right hand side of Fig. 1 shows the practical realization. On one side, the sample is fixed to the copper holder by a clamp, while the other side is bent by a lever. The lever can be moved from the backside by a micrometer screw or by a piezo mover that is integrated with the screw. Therefore, an exact adjustment of the bending is achieved. To control the temperature of the sample, the backside of the copper holder is connected to a water cooler and to a Peltier element.

3. Results

3.1 Variation of wavelength and output power with anisotropic strain

After suppressing the dominant polarization of the VCSEL by a polarizer, an optical spectrum analyzer is employed to examine the non-lasing polarization mode that occurs due to amplified spontaneous emission. Figure 2 shows the wavelength dependence of the two orthogonal polarizations on the bending b for a 980 nm sample with a thickness of $360\,\mu$m, where strain is applied along the [011] direction. With $l = 6$ mm in Fig. 1, the maximum bending of $73\,\mu$m creates a tensile strain at the surface of the wafer of approximately $65\,\mathrm{N/mm^2}$. This strain induces a wavelength splitting of 100 pm between the orthogonal polarization modes. Due to the elasto-optic effect, the wavelength of the [011] polarization increases linearly while the wavelength of the [0$\bar{1}$1] polarization decreases.

In Fig. 3 the light versus current (LI) characteristics of an adjacent VCSEL on the same sample are shown for different values of the bending b. The device has a surface relief with
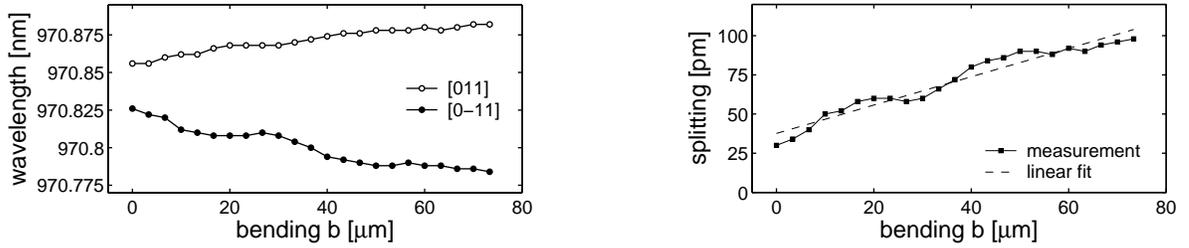
Fig. 2: Polarization-resolved emission wavelengths of a VCSEL with an oxide aperture of 7.5 µm diameter and a 5.1 µm surface relief in dependence on the bending b in [011] direction.

a diameter of 9.1 µm to enhance the single-mode output power. When no stress is applied, the VCSEL is polarization-stable within its single-mode regime and the [011] polarization dominates. However, when the sample is bent by 17 µm in the [011] direction, the laser starts to lase in [0$\bar{1}$1] polarization and switches to the [011] polarization at a current of 6.7 mA. This corresponds to a type I switch, namely a switch from the shorter to the longer wavelength. When the bending of the sample increases further, the polarization switch moves to higher currents and the [0$\bar{1}$1] polarized region becomes wider.
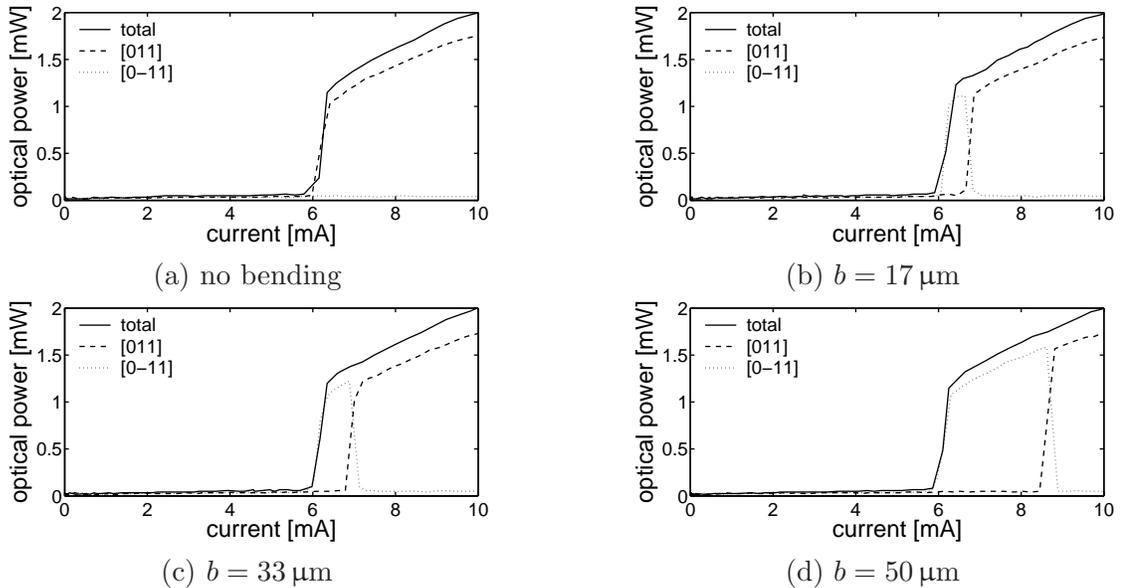
Fig. 3: LI characteristics of a VCSEL adjacent to the device in Fig. 2 for different values of the bending b in [011] direction. With increasing strain a polarization switch appears and the width of the [0$\bar{1}$1] polarized region increases. The device has a 10 µm oxide aperture and a surface relief with a diameter of 9.1 µm.

During the experiments, various VCSELs on samples with 980 as well as 850 nm emission wavelength have been examined with stress applied in different directions. It was found for all devices that the polarization parallel to the direction of the stress experiences a strong suppression, in agreement with the example in Fig. 3. Even the polarization of higher order transverse modes can be changed in this way.

3.2   Stability assessment of surface grating induced polarization control

Since the occurrence of polarization switches complicates the use of VCSELs in many applications, there are urgent needs for polarization control. In 2003, the optoelectronics department began to implement dielectric surface gratings in VCSELs, which led to outstanding results with regard to polarization control [6], [7]. To assess the stability of the induced polarization control, the polarization behavior of 850 nm VCSELs with a dielectric surface grating was examined under external induced stress.

Figure 4 shows the wavelength difference between the lasing and non-lasing mode in dependence on the bending of the sample. Positive values of the bending refer to strain in [011] direction, whereas negative values are associated with strain in [0$\bar{1}$1] direction. The 510 μm thick sample was maximally bent by 67 μm, corresponding to an induced strain of approximately 84 N/mm². When the sample exp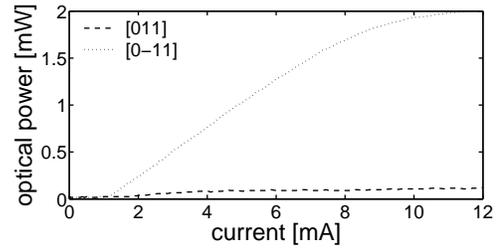eriences strain in [011] direction, the [011] polarization has a higher wavelength, associated with a positive wavelength splitting. By applying strain along the [0$\bar{1}$1] direction, the wavelength splitting becomes negative, in agreement with the elasto-optic effect. The nonlinear relation between bending and wavelength splitting for positive values of the bending may be caused by a weak fixing by the clamp in this measurement.
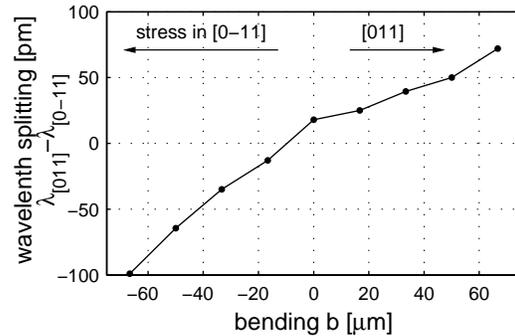
Fig. 4: Wavelength splitting $\lambda_{[011]} - \lambda_{[0\bar{1}1]}$ versus the bending b of a surface grating VCSEL sample. A positive bending b corresponds to strain in [011] direction, negative b to strain in [0$\bar{1}$1] direction.

Figure 5 shows the LI characteristics of two nominally identical VCSELs on the same sample, 250 μm apart from each other, for stress along the [0$\bar{1}$1] direction. Both VCSELs have an oxide aperture of about 6.5 μm. When no strain is applied (a), the device without a grating on the left hand side, shows a switch in polarization from the [0$\bar{1}$1] to the [011] direction. When the sample is bent by $b = -33$ μm, no switch occurs any more and the first two modes start to lase in [011] direction (see Fig. 5(b)). Also for higher order modes a dominance of the [011] polarization is observed that increases further if the strain is increased (see Fig. 5(c)). In agreement with the results of Sect. 3.1, strain along the [0$\bar{1}$1] direction thus leads to a preference of the [011] polarization.

(a) no bending
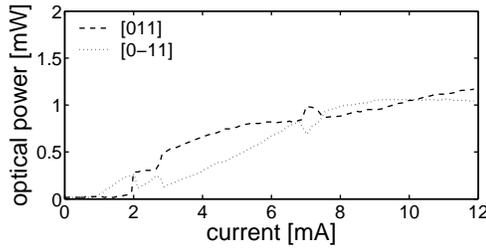
(b) bending $b = -33\,\mu\text{m}$
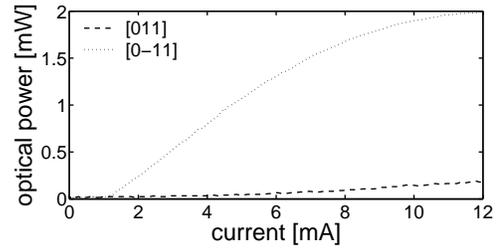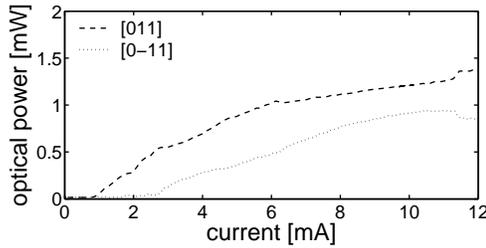
(c) bending $b = -67\,\mu\text{m}$
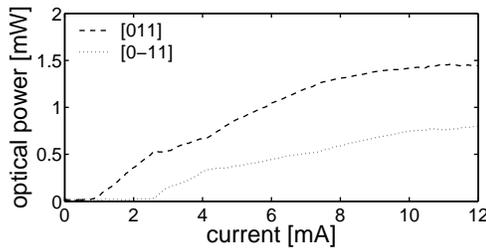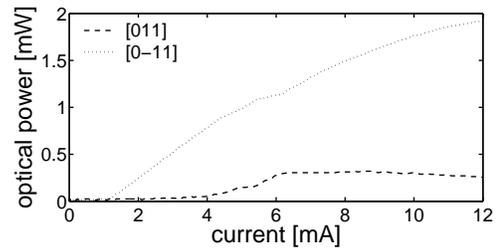
Without grating   With grating

Fig. 5: Polarization behavior of two VCSELs on a 850 nm sample under strain in $[0\bar{1}1]$ direction. The VCSEL on the left hand side has no grating, whereas the VCSEL on the right hand side has a grating in the $[0\bar{1}1]$ direction with a period of 0.7 μm and a grating depth of 39 nm.

The VCSEL on the right hand side of Fig. 5 has a surface grating in $[0\bar{1}1]$ direction with a period of 0.7 μm and a grating depth of 39 nm. Without external stress, it shows a strong suppression of the [011] polarization of more than 12 dB until thermal rollover, where 10 modes are lasing.

When strain along the $[0\bar{1}1]$ direction is applied, the orthogonal polarization suppression for higher order modes decreases. However, polarization switches can be avoided over the entire operation range. Even if the bending of the sample is increased to $b = -67\,\mu\text{m}$, the polarization of the first two modes is still fixed in $[0\bar{1}1]$ direction, although in the reference VCSEL the [011] polarization already dominates (see left hand side of Fig. 5(c)). Therefore, an outstanding stability of the induced polarization control is observed.

4. Conclusion

By applying external stress to VCSELs, a wavelength splitting of up to 100 pm has been induced. In that way, polarization switches can be enforced and the switching current can be varied. A strong preference of the polarization orthogonal to the direction of the induced strain was observed.

To assess the polarization control introduced by a dielectric surface grating, the polarization behavior of VCSELs with and without grating have been examined under external stress. Even for a strong bending, which induced a wavelength splitting of more than 60 pm, the polarization of the fundamental mode as well as that of the first higher order mode was not affected, while the polarization of the VCSEL without grating was already strongly dominated by the orthogonal polarization. Thus, a dielectric surface grating enables a stable, dependable polarization control, even under high anisotropic strain.

References

[1] M.P. van Exter, A.K. Jansen van Doorn, and J.P. Woerdman, "Electro-optic effect and birefringence in semiconductor vertical-cavity lasers," *Phys. Rev. A*, vol. 56, no. 1, pp. 845–853, 1997.

[2] K. Panajotov, J. Danckaert, G. Verschaffelt, M. Peeters, B. Nagler, J. Albert, B. Ryvkin, H. Thienpont, and I. Veretennicoff, "Polarization behavior of vertical-cavity surface-emitting lasers: experiments, models and applications," *Proc. AIP*, vol. 560, no. 1, pp. 403–417, 2001.

[3] P. Debernardi and G.P. Bava, "Effects of anisotropies on vectorial modes of vertical-cavity surface emitting lasers," *phys. stat. sol. (a)*, vol. 188, no. 3, pp. 967–977, 2001.

[4] A. Yariv and P. Yeh, *Optical Waves in Crystals*. New York: Wiley, 1984.

[5] K. Panajotov, B. Nagler, G. Verschaffelt, A. Georgievski, H. Thienpont, J. Danckaert, and I. Veretennicoff, "Impact of in-plane anisotropic strain on the polarization behavior of vertical-cavity surface-emitting lasers," *Appl. Phys. Lett.*, vol. 77, no. 11, pp. 1590–1592, 2000.

[6] J.M. Ostermann, C. Jalics, A. Kroner, M.C. Riedl, R. Michalzik, and P. Debernardi, "Polarisationskontrolle von VCSELn mit Hilfe eines monolithisch integrierten Oberflächengitters," *Photonik*, vol. 35, no. 6, pp. 42–44, 2003.

[7] J.M. Ostermann, P. Debernardi, C. Jalics, A. Kroner, M. Feneberg, M.C. Riedl, and R. Michalzik, "Monolithic polarization control of multimode VCSELs by a dielectric surface grating," in *Vertical-Cavity Surface-Emitting Lasers VIII,* C. Lei, K.D. Choquette, S.P. Kilcoyne (Eds.), SPIE Proc. 5364, San Jose, CA, USA, January 2004, in press.

Beam Properties and Quality Factor of VCSELs

Ihab Kardosh[*]

In this article, the concept of laser beam propagation and beam quality factor (M^2 factor) is described. We discuss different relations between real laser beams and the ideal Gaussian beam in terms of the M^2 factor. Measurement methods are presented which help to determine the quality factor and other beam parameters of VCSELs, such as divergence angle, Rayleigh length, and beam waist.

1. Introduction

For many industrial and scientific laser applications, such as materials processing, fiber coupling, beam collimation, and beam focusing, it is necessary to have a good laser beam quality. In general, propagating laser beams deviate from an ideal Gaussian intensity distribution. The degree of deviation can be conveniently quantified by a quality factor M^2 (called the "M-squared" factor or the "times diffraction limit number"). This factor has been defined such that $M^2 = 1$ for an ideal Gaussian beam. Real laser beams have factors greater than one. For example helium neon lasers have typically an M^2 factor of less than 1.1. The M^2 factor of single-mode laser diodes is in the range of 1.1 to 1.5. For multi-mode lasers, M^2 can be as high as 20 and more. Therefore, the beam quality is important for many laser measurements and optical designs, where the M^2 factor cannot be neglected.

2. Real Beam Propagation and M^2 Concept

Laser beam propagation can be described using the Gaussian equation

$$w(z) = w_0 \sqrt{1 + \left(\frac{z - z_0}{z_\mathrm{R}} \right)^2} \tag{1}$$

with

$$z_\mathrm{R} = \pi w_0^2 / \lambda \ , \tag{2}$$

where $w(z)$ is the beam radius, w_0 the radius of the beam waist, z_0 the beam waist location, and z_R the Rayleigh length. When propagating a distance z_R from the waist,

---

the beam radius expands by a factor of $\sqrt{2}$. This distance defines the beginning of the far-field region where the beam propagates with the constant divergence angle

$$\vartheta \approx \tan \vartheta = \frac{w_0}{z_{\mathrm{R}}} \ , \tag{3}$$

where the approximation is valid for small angles ϑ. The product of beam waist and divergence angle

$$w_0 \cdot \vartheta = \frac{\lambda}{\pi} \tag{4}$$

is a lower fundamental limit which can only be approached by an ideal Gaussian beam. To describe real laser beams, the M^2 factor should be considered and included in the product of beam waist and divergence angle as

$$W_0 \cdot \Theta = \frac{\lambda}{\pi} M^2 \ . \tag{5}$$

To distinguish between the ideal Gaussian beam and real beams, we use lower case symbols that refer to the former and upper case symbols for the latter. For the Rayleigh length we obtain

$$Z_{\mathrm{R}} = \frac{\pi W_0^2}{M^2 \lambda} \ . \tag{6}$$

Both, divergence angle as well as beam waist, must be known to obtain an accurate result for the M^2 factor. Measuring only one parameter, e.g. the divergence angle without determining the actual waist size and location, leads to different M^2 factors as seen in the theoretical plots in Fig. 1. Real laser beams of the same divergence angle as an ideal Gaussian beam have a beam waist which is enlarged by the factor M^2 (Fig. 1, left), namely for the beam waist–divergence product we may write

$$W_0 \cdot \Theta = M^2 w_0 \cdot \vartheta \implies W_0 \propto M^2. \tag{7}$$
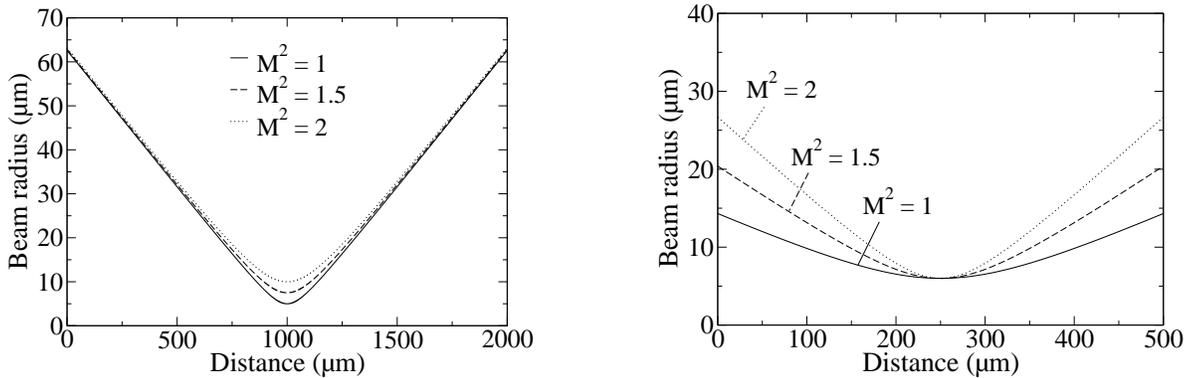
Fig. 1: Laser beams of constant divergence angle (left) and constant beam waist (right) for different M^2 factors.

If both beams have the same waist size, real beams will diverge faster by the factor M^2 (Fig. 1, right), as seen from

$$W_0 \cdot \Theta = w_0 \cdot M^2 \vartheta \implies \Theta \propto M^2. \tag{8}$$

Another relationship between real beams and the Gaussian beam is the so-called embedded Gaussian beam, illustrated in Fig. 2. This relationship [1] describes the propagation of multi-mode laser beams such that both their beam waist and divergence angle are increased over those of an ideal beam by a factor $M = \sqrt{M^2}$. Here, the product

$$W_0 \cdot \Theta = M w_0 \cdot M \vartheta \tag{9}$$

leads to the same result as in the previous relationships (7), (8) and as shown before in (5).
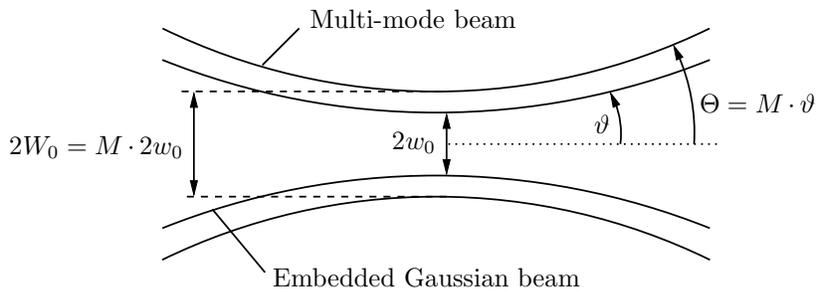
Fig. 2: The embedded Gaussian beam. It represents the relationship between the fundamental and higher order modes of a geometrically stable laser resonator.

3. Measurement Method and Setup

Figure 3 shows the experimental setup for the beam quality characterization. The laser beam of a mounted VCSEL is transformed through a lens such as to form a beam waist in the output beam. Two detectors with slits of $45°$ and $-45°$ orientation scan the beam and measure the intensity profiles in x-direction for different propagation distances. According to a procedure defined by the ISO [2], ten measurements along the propagation axis must be at least performed, where half of them should be within the Rayleigh length on both sides of the beam waist. The detector head used in the measurement setup is part of the beam analyzer *BeamScope* [3], which provides a complete M^2 measurement. In our setup only the detectors have been used to measure the intensity distribution. Other commercial instruments, e.g. the *ModeMaster* [4] use the knife-edge technique to determine the M^2 factor. In Fig. 4, intensity profiles of a multi-mode laser are shown. For Gaussian beams, the $1/e^2$ beam diameter definition is used. The beam diameter of multi-mode lasers is calculated using the second-moment definition

$$\sigma^2 = \frac{\sum y \cdot (x - \bar{x})^2}{\sum y} \quad \text{with} \quad \bar{x} = \frac{\sum y \cdot x}{\sum y} \, , \tag{10}$$

where the beam width is four times the standard deviation σ of the intensity distribution $y(x)$. Calculated beam diameters are plotted versus the propagation distance and then fitted according to (1) (while replacing z_R with Z_R from (6)) to determine the M^2 factor and other beam parameters. Another M^2 measurement method described in [5] uses just four beam diameter measurements to determine the M^2 factor.
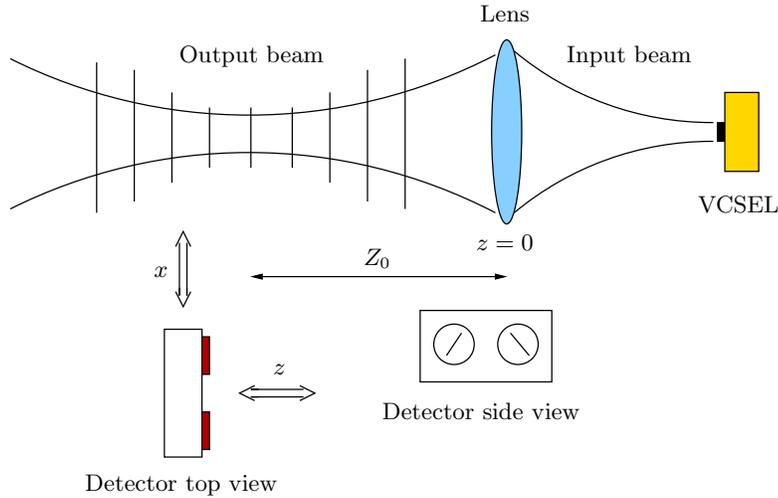
Fig. 3: Setup for the measurement of the beam quality of VCSELs.
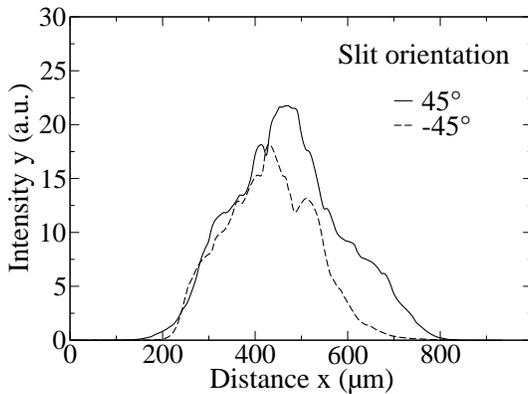
Fig. 4: Intensity profiles of a multi-mode laser. The active diameter of the VCSEL is about $36\,\mu$m.

4. Experimental Results

Beam properties of 980 nm oxide-confined multi-mode VCSELs have been investigated. In this section we present measurement results of the quality factor, waist size and divergence angle of a device with $36\,\mu$m active diameter. We started the characterization with a standard far-field measurement as shown in Fig. 5. The beam intensity of the device is plotted versus the divergence angle. The far-field angle Θ is about 5.7°, which is two times the calculated standard deviation.
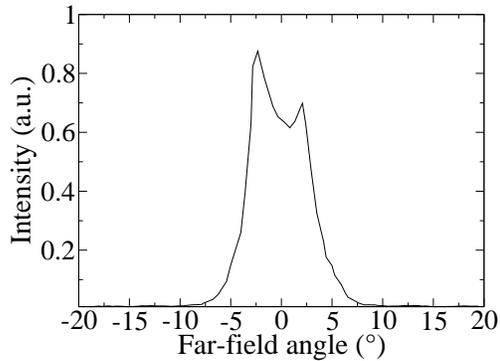
Fig. 5: Typical far-field intensity distribution of a 36 μm diameter multi-mode VCSEL emitting at 980 nm wavelength. Threshold current and driving current are ≈ 7 mA and 10 mA, respectively. The far-field angle Θ is about 5.7°.

As previously described in Sect. 3, an M^2 measurement is performed on the same VCSEL device. The beam radii are plotted versus the propagation distance in Fig. 6. The hyperbolic form of the theoretical propagation curve (1) was used to fit the data points. The fit parameters and other beam properties are listed in Table 1. The magnification factor V is calculated using

$$V = \frac{Z_0 - f}{f} , \tag{11}$$

where Z_0 is the waist location (see Fig. 3) and $f = 14.5$ mm the focal length of the lens. The M^2 factor of the measured multi-mode VCSEL is about 6.3 and the divergence angle is approximately 5.4°, which corresponds very well to the result of the far-field measurement. The results from both detectors show that the laser beam is not purely circular. The measured multi-mode device has an active radius of 18 μm, which is comparable to the calculated waist sizes of 18.0 μm and 20.7 μm, respectively.
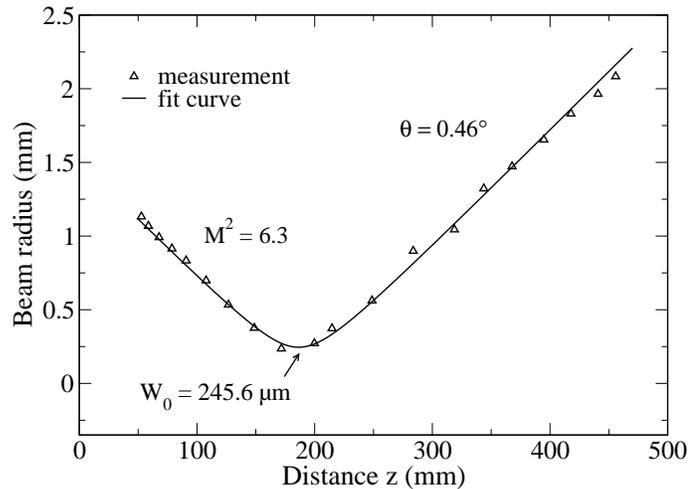
Fig. 6: Experimentally determined results of the beam radius versus propagation distance. The data points (detector at 45° position) of the 36 μm diameter multi-mode VCSEL (980 nm, $I = 10$ mA) were fitted to calculate the M^2 factor and other beam parameters.

Tab. 1: Beam parameters of a $36\,\mu$m diameter multi-mode VCSEL. The parameters in the input beam section (see Fig. 3) were calculated using the magnification factor V.

Slit orientation	Output beam		Input beam	
	$45°$	$-45°$	$45°$	$-45°$
W_0	$245.6\,\mu$m	$209.3\,\mu$m	$20.7\,\mu$m	$18.0\,\mu$m
Z_R	$30.8\,$mm	$25.5\,$mm	$219.3\,\mu$m	$189\,\mu$m
Θ	$0.46°$	$0.47°$	$5.4°$	$5.45°$
Z_0	$186.4\,$mm	$183\,$mm		
M^2	6.3	5.5		

5.   Conclusion

We have investigated the beam properties of multi-mode VCSELs. Far-field and M^2 measurements have been performed to determine beam parameters such as the beam quality factor and the divergence angle. For a $36\,\mu$m diameter multi-mode device we have obtained an M^2 factor and a divergence angle of 6.3 and 5.4°, respectively.

References

[1] T.F. Johnston, Jr, "M^2 concept characterizes beam quality," *Laser Focus World*, pp. 173–183, May 1990.

[2] International Organization for Standardization, *Lasers and laser-related equipment. Test methods for laser beam parameters, beam widths, divergence angle and beam propagation factor. ISO 11146*, 1996.

[3] DataRay, Inc., *BeamScope-P5*, 2001.

[4] Coherent, Inc., *ModeMaster PC*, 2001.

[5] T.F. Johnston, Jr, "Beam propagation (M^2) measurement made as easy as it gets: the four-cuts method," *Appl. Optics*, vol. 37, no. 21, pp. 4840–4850, 1998.

Low Thermal Resistance Flip-Chip Bonding
of 850 nm 2-D VCSEL Arrays
Capable of 10 Gbit/s/ch Operation

Hendrik Roscher*

In 2003, our well established technology of flip-chip mounted 2-D 850 nm backside-emitting VCSEL arrays evolved to bring about substantial thermal improvements. We have reduced the oxide-confined VCSEL's thermal resistance by half, to a value of about 1.3 K/mW for 10 μm devices. An optimized solder joint placement eliminates the major thermal bottlenecks within the flip-chip VCSEL structure. The thermal performance of the improved cell design is compared to the previous version for devices with 250 μm pitch in 4×8 and 8×8 arrays. Neighboring VCSELs within these arrays are also shown to be thermally isolated with thermal cross resistances of about 0.015 K/mW. Furthermore, quasi error-free (bit error rate $< 10^{-12}$) 10 Gbit/s transmission was demonstrated by feeding the signals to the flip-chip mounted VCSELs through 7 mm-long coplanar transmission lines on a silicon carrier chip.

1.   Introduction

Vertical-cavity surface-emitting lasers (VCSELs) arranged in two-dimensional (2-D) configurations of independently addressable elements hold great potential for short-reach fiber-optic as well as free-space networking applications. Given the continuous growth of required data rates in networks, parallel optical interconnects (POIs) based on VCSEL arrays are expected to be found more and more at increasingly deeper network levels in the future.

First 2-D arrays were InGaAs quantum well based, emitting at wavelengths around 980 nm. While readily allowing backside emission through the GaAs substrate, low-cost Si based photodetectors have extremely poor sensitivities for wavelengths approaching 1 μm. Today's short-reach optical interconnect applications therefore rely on the standardized 850 nm emission wavelength regime. As far as single devices or linear arrays are concerned, wire bonding is typically used for contacting and top side emission is perfectly acceptable. Yet, for 2-D solutions high-speed electrical signals often cannot be fed to the VCSELs from external contacts and flip-chip bonding is the solution of choice to provide low parasitics electrical interconnects. Bottom side emitting VCSELs particularly lend

themselves to the flip-chip integration of large 2-D arrays. They naturally direct the electrical and optical domains to opposite sides of the VCSEL chip. Hence, the optics do not get in the way of the electronics and the benefits of the flip-chip approach are therefore best utilized with bottom-emitting VCSELs. The GaAs substrate, however, is opaque at 850 nm and the need to completely remove or replace it does add additional complexity to the fabrication of 850 nm bottom-emitting VCSEL arrays.

The details of flip-chip assembly and substrate removal were given in last year's report. In what follows, the focus is placed on design changes leading to thermal improvements along with the implications of these changes for crucial device characteristics such as spectral red shift and optical output power. Error-free 10 Gbit/s data transmission will also be demonstrated.

2.   Low Thermal Resistance Device-Level Packaging

In the early stages of development of this flip-chip technology, a lateral offset was introduced between the VCSEL mesa and the bond pads in order to keep the solder joints away from the active structures. This offset-bonded design illustrated in the left half of Fig. 1 ensures that no stresses arising from coefficient of thermal expansion mismatches between the joined substrates would adversely affect the VCSEL performance. The lateral offsets necessitate three levels of metallization and separate polyimide layers functioning both as planarization and non-wettable layer. The additional complexity of this design enables a simple incorporation of a plating base required for electroplating metal layers which is a more cost efficient way of metal deposition than evaporation or sputtering. The offset-bonded design also ensures that the bond pads are at exactly the same elevation and on a perfectly even surface.
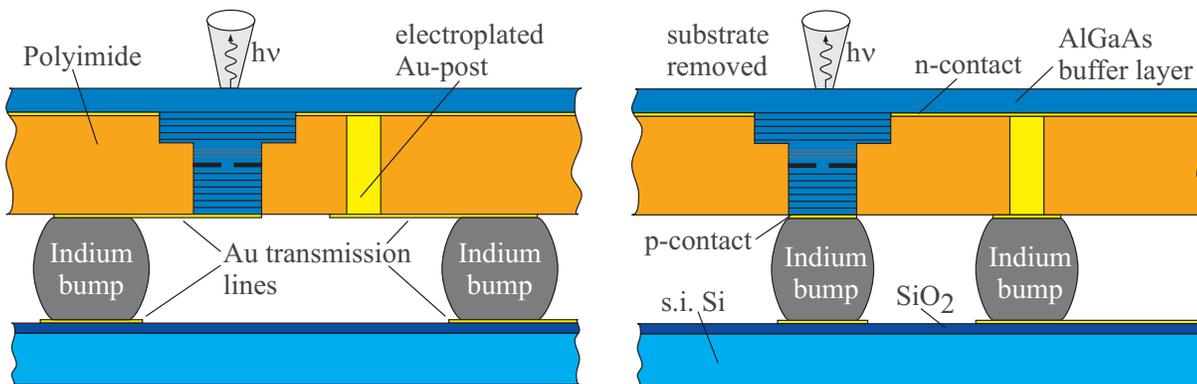
Fig. 1: Illustration of the offset-bonded (*left*) and the direct-bonded (*right*) VCSEL design.

The development of stable bond pads serving as foundation for the solder joints, the use of soft indium solder, and precise bump size control permitted direct mesa bonding as indicated in the right-hand schematic of Fig. 1. This design involves different bump sizes for the n- and p-solder joints and can thus accommodate uneven bond pads at different mean elevations (omitted in the figure).

The indium solder is deposited by evaporation and structured by lift-off since, in contrast to electroplating which is also available for indium, it offers a tight control of the deposited heights as well as the additional freedom to vary the bump sizes by utilizing more or less of the area between the bond pads. The footprints of the evaporated solder deposits can have many different shapes, such as in Fig. 2, and with a given difference in footprint area the standoff difference between the p- and n-solder joints is adjusted by the applied solder thickness. Indium lift-off was done for thicknesses ranging from 3 to 12 µm. The structured deposits in Fig. 2 have a thickness of only 4 µm and side lengths of about 100 µm. Despite of this relatively high aspect ratio, the indium reliably flows to form evenly shaped balls on subjecting it to high temperatures above its melting point of approximately 160 °C. The visible dents become more pronounced with shorter cool-down cycles after reflow. Fortunately, they do not seem to have a negative effect on the bonding yield.
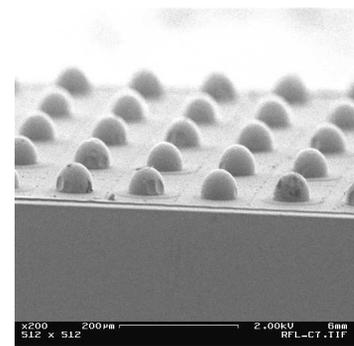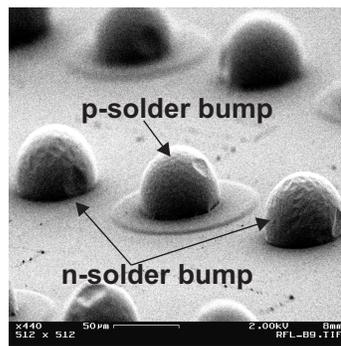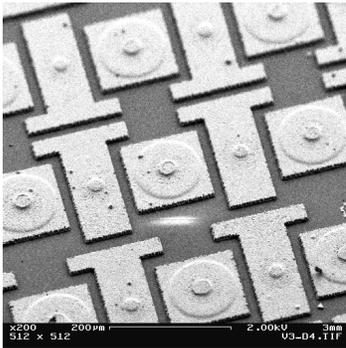
Fig. 2: Evaporated indium deposits after lift-off structuring.

Fig. 3: Indium solder balls after reflow. The p-solder ball sits on top of the n-mesa, and the p-mesa is inside the solder ball.

Indium solder, being a pure metal, has high thermal and electrical conductivities. Furthermore, no alloy related problems like decomposition leading to brittle high resistivity connections can occur. Its particular softness allowed the p-part of the VCSEL mesa to actually be fully inside the solder ball which partially sits on top of the n-mesa as the left half of Fig. 3 shows. To completely enclose the low mobility p-side of the VCSELs, where most of the heat is generated, is a possibility that is only available to bottom-emitting VCSELs. By eliminating some major thermal bottlenecks, the direct-bonded design leads to a substantially improved thermal performance of the VCSELs which will be further discussed in the following section.

3. Static Characteristics

Figure 4 compares the thermal performance of the two flip-chip bondable VCSEL designs discussed so far. The lateral paths in the offset-bonded VCSELs hamper the heat transport within the structure and result in a rather high thermal resistance R_T of $2.6\,\mathrm{K/mW}$ for the $10\,\mu\mathrm{m}$ diameter lasers which is the only size available for this design. We measured a sample of 15 VCSELs in each of three 8×8 arrays and found the value highly reproducible with about $0.05\,\mathrm{K/mW}$ standard deviation. The large R_T leads to a drastic junction temperature (T_j) rise during operation, e.g. $\Delta T_j \approx 50\,\mathrm{K}$ at $10\,\mathrm{mA}$ laser current, which causes a pronounced red-shift of the output spectra displayed in the upper part of Fig. 5. Higher internal temperatures generally shorten the lifetime of these devices.
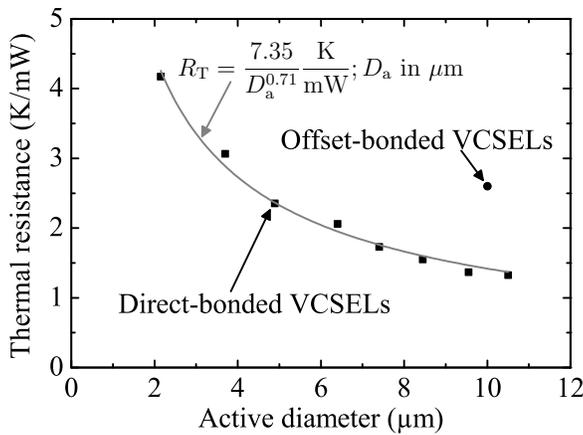
Fig. 4: Measured thermal resistances for various sizes of the direct-bonded VCSELs, and for $10\,\mu\mathrm{m}$ offset-bonded VCSELs.
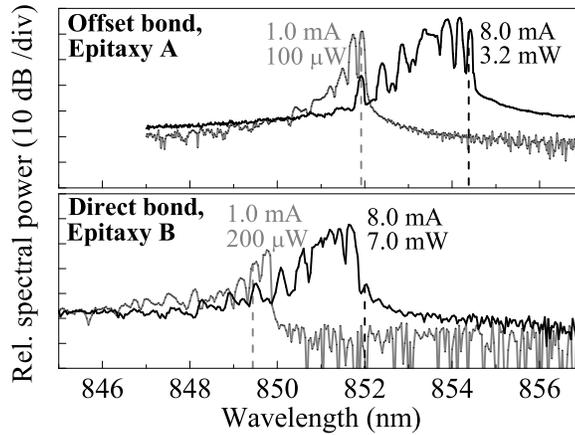
Fig. 5: Comparison of the spectral red shifts of different wafers in offset-bonded (*top*) and direct-bonded (*bottom*) configuration.

For the direct-bonded VCSELs, there were 8 different aperture sizes fabricated within 4×8 element arrays. The data in Fig. 4 demonstrate the thermal resistance was cut by half to about $1.3\,\mathrm{K/mW}$ for 10 to $10.5\,\mu\mathrm{m}$ devices merely through elimination of thermal bottlenecks in the signal path within the cell design. Of course the high-frequency performance is expected to also benefit from streamlining the signal path.

In a real world application, all channels of the arrays are intended to be operated in parallel. It is therefore essential, besides having low thermal resistances, to ensure minimal thermal crosstalk between immediate neighbors not only to prevent signal degradation, but chiefly to prevent thermal breakdown during operation. If a VCSEL would use additional paths through neighboring cells for heat extraction, the array with all cells operating would quickly overheat. Hence, it is important that the thermal resistances presented above account only for heat paths within one cell.

In the current design, the VCSELs are thermally connected only through a very thin semiconductor layer over a distance of $250\,\mu\text{m}$. The resulting thermal cross resistances $R_{\text{T,X}}$ are $0.016\,\text{K/mW}$ and $0.013\,\text{K/mW}$ for the offset-bonded and direct-bonded VCSELs, respectively. For extremely closely spaced VCSELs that are supposed to be operated simultaneously, a good thermal isolation would have to be maintained by completely separating the VCSELs from one another.
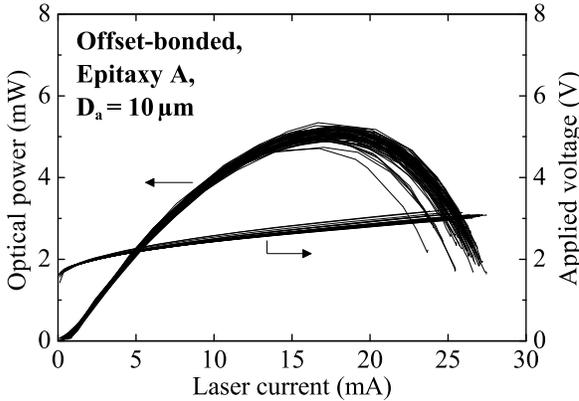
Fig. 6: Complete LIV curves for a 64-channel VCSEL demonstrator. All VCSELs in the 8×8 offset-bonded array have $10\,\mu\text{m}$ aperture size.
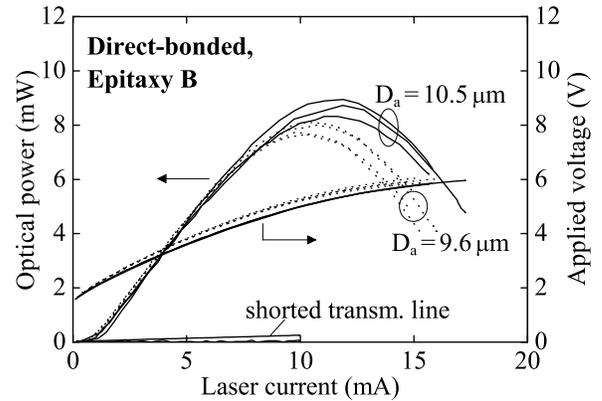
Fig. 7: LIV curves of two sizes of direct-bonded VCSELs. The shorted VCSEL is caused by a visibly shorted transmission line on this early fabricated carrier.

Figure 5 compares the spectral red shifts of VCSEL arrays made from different epitaxial material. The magnitude of the spectral shift $\Delta\lambda$ is approximately $2.5\,\text{nm}$ for both the offset-bonded and direct-bonded configurations. At the same operating point, the internal temperature rise is the same for both designs. The reason for this is that epitaxy B of the direct-bonded VCSELs was optimized for a high differential quantum efficiency η_{d}. As Fig. 7 reveals, the optical field benefited from the optimization resulting in an η_{d} as high as $75\,\%$, but at the expense of inferior electrical properties. The electrical resistance was drastically increased to about $350\,\Omega$ leading to twice the dissipated power.

Nevertheless, a much higher maximum output power is obtained from those VCSELs as compared to the offset-bonded VCSELs in Fig. 6 due to their thermally optimized packaging. Enhanced heat extraction in the direct-bonded configuration makes it possible to turn the high η_{d} into a high maximum wallplug efficiency $\eta_{\text{c,max}}$ of $28\,\%$ at $3\,\text{mA}$ and a maximum output power of $9\,\text{mW}$ at $12\,\text{mA}$. Figure 6 displays the complete light–current–voltage (LIV) curves of an offset-bonded array where epitaxy A was used. The differential resistance of those devices has a more typical value of $40\,\Omega$ leading to much less dissipated power. But due to the doubled thermal resistance these devices heat up quickly as well and with a low differential quantum efficiency of $30\,\%$ the maximum wallplug efficiency is reached with $20\,\%$ at $5\,\text{mA}$ and the output power levels off at $5\,\text{mW}$ and $18\,\text{mA}$.

4. Dynamic Performance of Flip-Chip VCSEL Demonstrators

The modulation characteristics of the flip-chip bonded VCSELs have been measured with a microwave probe placed at the far ends of the about 7 mm-long coplanar transmission lines on the fanout chip as indicated by the inset of Fig. 8. The parasitics of the lines are superimposed on the VCSEL resonant curves and the transfer functions therefore have maximum small-signal 3-dB and 10-dB bandwidths of 7 GHz at 6 mA and 9.4 GHz at 10 mA of operating current, respectively. Note that the photoreceiver has a 3-dB bandwidth of 8 GHz.
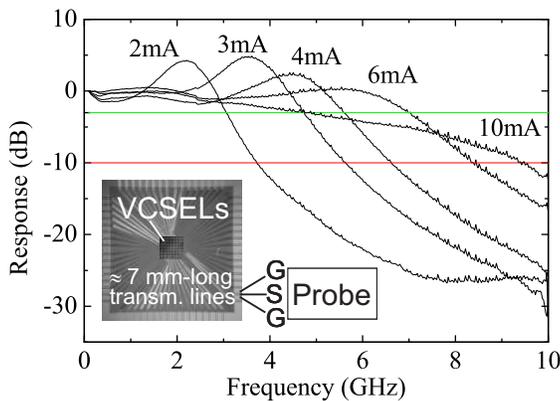
Fig. 8: Bias-dependent transfer functions of the flip-chip VCSEL demonstrator shown as inset.
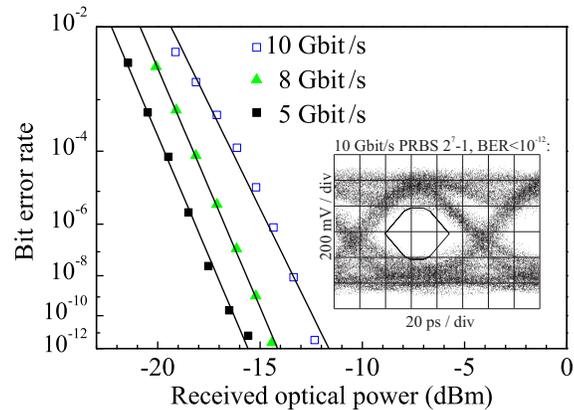
Fig. 9: Bit error rate (BER) characteristics of the offset-bonded VCSELs and eye diagram at 10 Gbit/s data rate.

Digital data transmission experiments were conducted using that same setup. The curves in Fig. 9 demonstrate that quasi error-free (bit error rate $< 10^{-12}$) 10 Gbit/s transmission was achieved. Although the present eye opening does not entirely conform to the indicated mask according to the IEEE 802.3ae 10-Gigabit Ethernet standard, there is much room for improvement through optimization of the fanout design and VCSEL dynamics.

5. Conclusion

Low thermal resistance direct mesa flip-chip bonding of VCSEL arrays was explained. The elimination of thermal bottlenecks by this approach cuts the thermal resistance by half to about 1.3 K/mW for 10 μm devices as compared to the offset-bonded devices. Neighboring cells (250 μm pitch) within the arrays are thermally isolated with thermal crosstalk values of about 0.015 K/mW.

To judge the dynamic performance, microwave signals are fed to the high-speed VCSELs through about 7 mm long low-loss coplanar transmission lines incorporated in the VCSEL demonstrator. The parasitics of the lines are superimposed on the VCSEL resonant curves which results in transfer functions exhibiting 3-dB and 10-dB corner frequencies of 7.0 and 9.4 GHz, respectively. Quasi error-free (bit error rate $< 10^{-12}$) 10 Gbit/s digital data transmission was achieved.

10 Gbit/s 850 nm VCSEL Based Data Transmission over 100 m-long Multimode Photonic Crystal Fibers

Martin Stach*

Quasi error-free 10 Gbit/s data transmission is demonstrated over a novel type of 50 µm core diameter photonic crystal fiber with as much as 100 m length. Combined with 850 nm VCSEL sources, this fiber is an attractive alternative to graded-index multimode fibers for datacom applications. Comparative numerical simulations suggest that the high bit rate may be partly explained by inter-modal diffusion.

1.   Introduction

Optical datacom as employed for the high-speed interconnection of electronic sub-systems has rapidly gained importance over the past years. Vertical-cavity surface-emitting lasers (VCSELs) emitting in the 850 nm wavelength regime and simple step-index fibers or graded-index fibers are preferred key components for low-cost link solutions [2]. Whereas, due to strong inter-modal dispersion, the use of the former fiber type is limited to link lengths of some meters at Gbit/s data rates, fabrication of the latter requires supreme control over the refractive index profile, especially in optimized 50 µm core diameter fibers enabling up to 300 m serial transmission of 10 Gbit/s signals. Since optical interconnect requirements move toward higher speed over shorter distances, the availability of an easily manufacturable, yet high-speed capable fiber medium would be very beneficial. This contribution reports on the properties of a new type of multimode photonic crystal fiber (PCF) fabricated by Crystal Fibre A/S. It features a simple waveguide geometry and allows 850 nm data transmission at 10 Gbit/s over a length of $L = 100$ m. For a recent review of photonic crystal fibers, the reader is referred to Ref. [3] and references therein.

2.   Fiber Design

The design of the new multimode photonic crystal fiber is illustrated in the insets of Fig. 1 which show optical micrographs of the fiber cross-sections. The fibers are made from a single material (light regions), and they comprise a solid, pure silica core suspended in air (dark regions) by narrow silica bridges of width b. The waveguiding properties of the fiber may accurately be tailored by adjusting parameters such as the size and shape of the core, the dimensions and number of silica bridges, or the fiber material. The numerical

---

*Work performed in collaboration with Crystal Fibre A/S, Denmark; www.crystal-fibre.com; see [1]

aperture (NA) of this type of PCF is essentially determined by the width of the silica bridges relative to the wavelength λ, as numerically demonstrated in Fig. 1. Here, we focus on two fibers with $33\,\mu m$ and $50\,\mu m$ core diameter and bridge widths of $b = 4.8\,\mu m$ and $7.0\,\mu m$, respectively, yielding NAs of around 0.07 and 0.05 at a wavelength of $850\,nm$. Despite the zero-index step between the core and the bridges, the fiber is capable of guiding light with good confinement to the multimode core. This is illustrated by the near-field intensity distribution for the $33\,\mu m$ core PCF displayed in Fig. 5. The fibers can be cleaved with commercially available equipment and they have an attenuation of the order $50\,dB/km$ at $850\,nm$ for typical bending radii such as $16\,cm$.
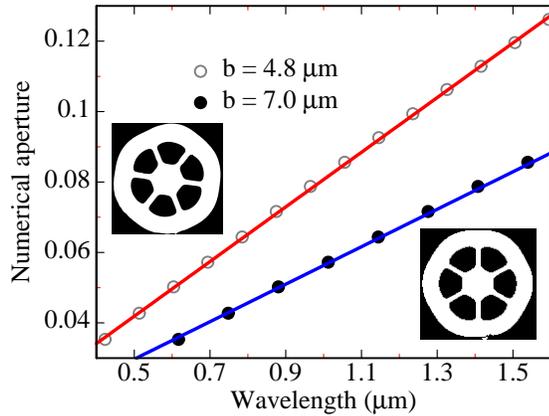
Fig. 1: Simulated NA for the $33\,\mu m$ core PCF (upper left inset) with bridges of width $b \simeq 4.8\,\mu m$ and the $50\,\mu m$ core PCF (lower right inset) with bridges of width $b \simeq 7.0\,\mu m$. Note the different scale for the two insets.

3.   Transmission Experiments

Assuming worst-case conditions [4], from the above NAs one can estimate a bit rate–length product of around $350\,Mbit/s \cdot km$ for the $50\,\mu m$ fiber, whereas the $33\,\mu m$ sample should have around $180\,Mbit/s \cdot km$. In what follows the transmission properties of such PCFs with a length of $L = 100\,m$ are examined.

3.1   Small-Signal Transfer Function and DMD

In order to get a first indication of the fibers' expected transmission bandwidths, we have determined the small-signal frequency responses with a scalar network analyzer. As optical source, standard $850\,nm$ GaAs based VCSELs have been employed. The $12\,\mu m$ active diameter, oxide-confined devices show transverse multimode emission with a root mean square spectral width of less than $0.4\,nm$ even under modulation. The lasing threshold current amounts to $1.8\,mA$ and the bias current for the small-signal as well as data transmission experiments was chosen as $9\,mA$, where the 3-dB bandwidth is $8.6\,GHz$. At the receiving end, a multimode fiber pigtailed InGaAs pin-type photoreceiver with above $8\,GHz$ bandwidth was used.

The left-hand side of Fig. 2 depicts the relative responses of both PCF samples. The 33 and $50\,\mu m$ core diameter fibers show a bandwidth–length product of 200 and $430\,MHz \cdot km$,
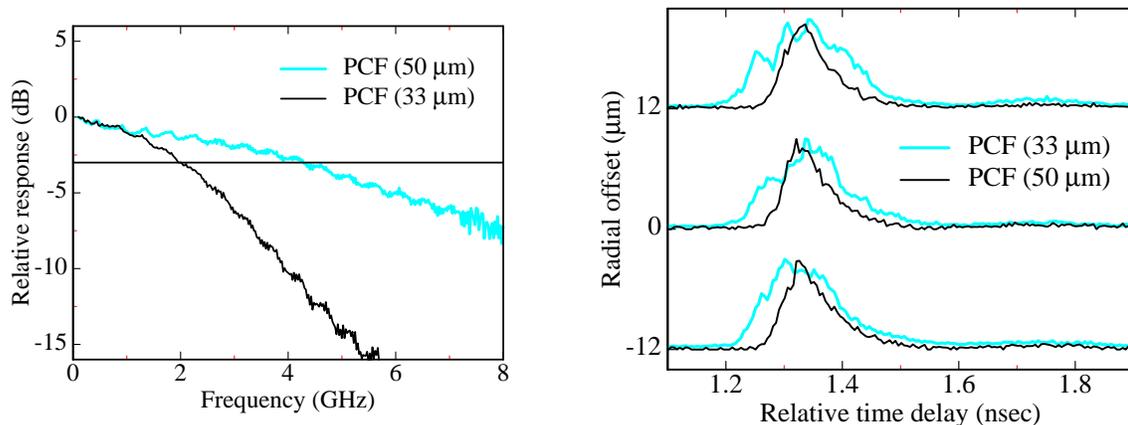
Fig. 2: Small-signal frequency responses at 850 nm for the two 100 m-long PCFs illustrated in Fig. 1 (left) and normalized DMD plots for both fibers at offset positions of −12, 0, and 12 μm (right).

respectively. These figures are significantly larger than expected from the corresponding NAs. In the next section we extend the NA estimations and show simulations of the modal time delays for the two PCFs.

In order to get quantitative insight into the modal delay properties, we have determined the PCFs differential mode delay (DMD) characteristics, see the right-hand side of Fig. 2. Here, a singlemode fiber is scanned over the PCF input and the impulse response at the output end is recorded for each offset position. A gain-switched 850 nm singlemode VCSEL delivering pulses with less than 40 ps full width at half maximum is employed for this purpose [5]. It is seen that the output pulses of the 50 μm fiber are rather narrow and virtually independent of the offset position. On the other hand, those of the 33 μm sample show larger variability and are up to twice as broad, which well supports the above observations.

3.2 Digital Data Transmission

Data transmission experiments have been carried out under non-return-to-zero $2^7 - 1$ word length pseudo-random bit sequence modulation using the aforementioned multimode VCSEL driven with 0.9 V peak-to-peak voltage. Figure 3 summarizes obtained bit error rate (BER) curves. With the smaller core diameter fiber, up to 5 Gbit/s could be transmitted without indication of a BER floor. The power penalty versus back-to-back (BTB) operation is about 3 dB at a BER of 10^{-12}. On the other hand, the 50 μm fiber even enables 10 Gbit/s transmission over $L = 100$ m length with only 2.9 dB power penalty. The observed increase in data rate is in full agreement with the small-signal and DMD measurement results.
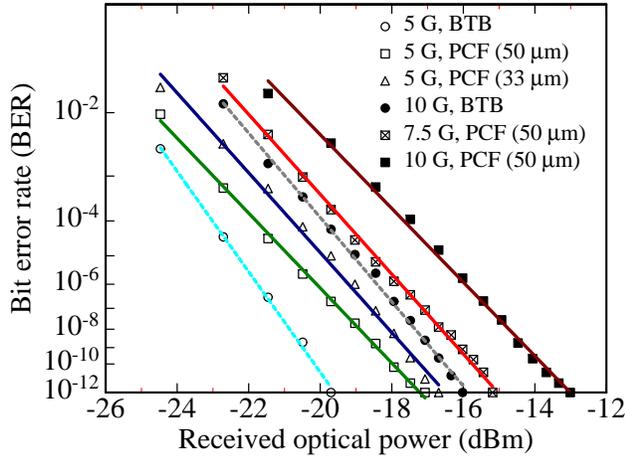
Fig. 3: BER characteristics for both 100 m-long PCFs at data rates of 5, 7.5, and 10 Gbit/s.

4. Simulations

A plane-wave method [6] is used to calculate the propagation constants $\beta_m = n_m \omega/c$ of the eigenmodes with index m, where n_m is the effective index, ω the angular frequency, and c the vacuum velocity of light. For the refractive index profile, optical micrographs are transformed to a one-bit format representing the two-component composite air–silica structure and for the refractive index a Sellmeier expression for $n(\omega)$ in silica and $n = 1$ in air is used. The simulation of Maxwell's equations for a given ω delivers sets of propagation constants $\{\beta_m\}$ and eigenfields $\{E_m\}$ where $m = 1, 2, 3, \ldots M$ with M as the number of guided eigenmodes. M is determined from the experimentally measured NA which is transformed to an effective cladding index n_{cl}. The number of guided eigenmodes M then follows from the requirement that $c\beta_M/\omega \geq n_{\mathrm{cl}}$.
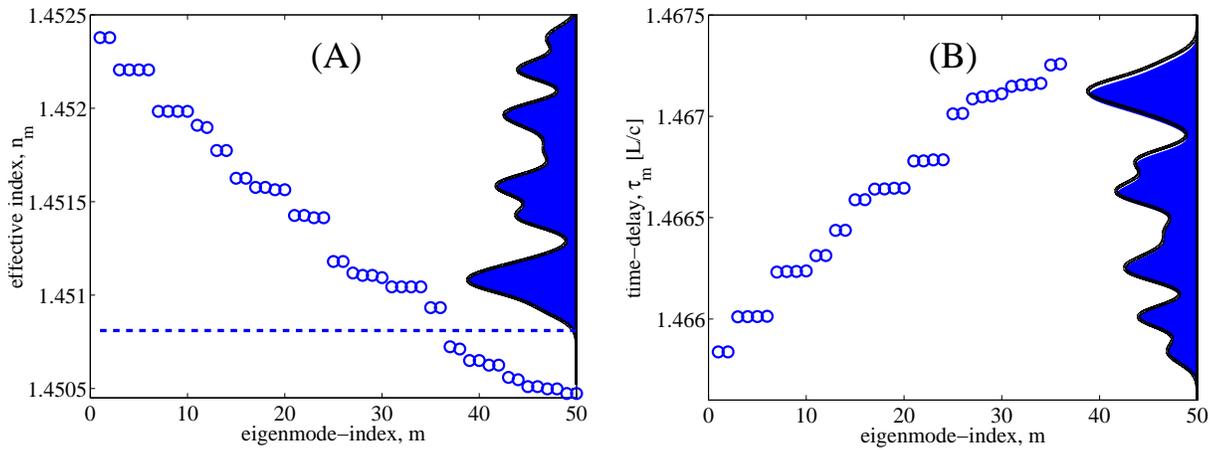
Fig. 4: Effective indices of the $M = 36$ guided eigenmodes at $\lambda = 850$ nm in a PCF with a 33 μm core (A; see upper left inset of Fig. 1). The horizontal dashed line indicates the cladding index n_{cl} corresponding to the experimentally measured NA. Corresponding time delays τ_m and the distribution $P(\tau_m)$ (B).
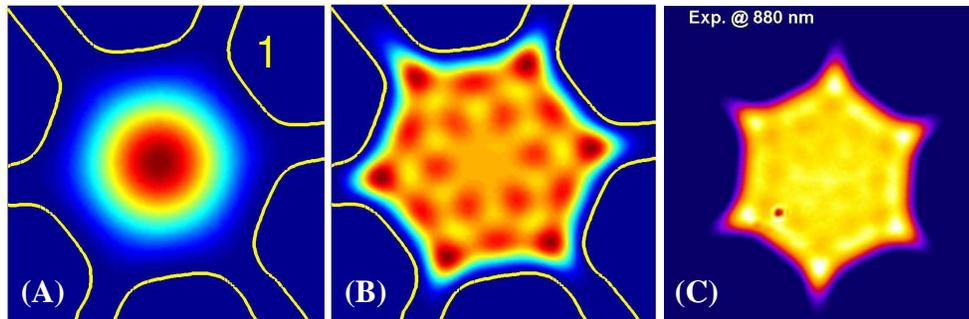
Fig. 5: Intensity distribution at $\lambda = 850\,\text{nm}$ in the $33\,\mu\text{m}$ PCF (see upper left inset in Fig. 1). Diagram (A) depicts the first ($m = 1$) eigenmode and diagram (B) shows the average eigenfield intensity which agrees well with the experimentally observed near-field intensity depicted in diagram (C). In diagrams (A) and (B), the contour lines indicate the air–silica interfaces.

The time delays (or group delays) are given by $\tau_m = L\partial\beta_m/\partial\omega$, where the group velocity is calculated by the approach described in Ref. [7]. The variation with m usually sets the limit on the bit rate and in that case the bit rate–length product is given by [4, 8]

$$B_T \cdot L \simeq L/\Delta T \ , \ \ \Delta T \approx \max\{\tau_m\} - \min\{\tau_m\}, \tag{1}$$

where ΔT is the width of the distribution $P(\tau_m)$ of the time delays. In the ray-optical picture, $\max\{\tau_m\}$ can be expressed in terms of the NA [4] and in this respect the expression is analogous to our estimations in Sect. 3 based on the NA. However, for a sufficiently low number of guided modes, quantitative differences caused by the beginning break-down of geometrical optics can be expected.

Figure 4 shows results at $\lambda = 850\,\text{nm}$ for a PCF with a $33\,\mu\text{m}$ core (see upper left inset in Fig. 1). Experimentally, this fiber is found to have NA $\simeq 0.07$ and the corresponding effective cladding index is indicated by the dashed line in the left diagram. For the given core size this results in $M = 36$ guided eigenmodes. Figure 4 (right) illustrates the time delays with the filled curve showing the distribution $P(\tau_m)$ (the projection of the data onto the y-axis) calculated from a superposition of Gaussians with a width given by the mean level spacing $(\tau_M - \tau_1)/(M - 1)$. We have $\Delta T \simeq 0.00087 \cdot L/c$ corresponding to $B_T \cdot L \simeq 344\,\text{MHz} \cdot \text{km}$ which, as expected, is somewhat larger than the NA estimate.

The total electric field E guided by the fiber is constructed by a linear combination of the eigenfields. For a not too narrow linewidth of the light source, cross-terms in $|E|^2$ might be neglected and for uniform (with respect to eigenmode index m) launch and attenuation an intensity distribution proportional to the average eigenfield intensity, i.e., $|E|^2 \approx M^{-1} \sum_m^M |E_m|^2$ is supposed to be measured. The same will be the case for arbitrary launch and strong mode mixing. As an example, Fig. 5 (A) shows the eigenfield intensity of the fundamental mode $m = 1$. The average eigenfield intensity (diagram B) compares well to the experimentally measured near-field intensity (C). This can be mainly attributed to the close-to-uniform launch of the fiber by a VCSEL since the good agreement for the bit

rate suggests that the effect of mode-mixing (inter-modal diffusion) is limited.

The eigenmodes fall into different groups with different degeneracies (these degeneracies are slightly lifted due to a weakly broken symmetry in the real fiber) as evident from both the effective indices in Fig. 4 as well as the corresponding intensity plots (not shown here; see [1]). The first two eigenmodes ($m = 1, 2$) are the doubly degenerate fundamental mode corresponding to the two polarization states of the fundamental mode in standard fibers and from a practical point of view they can be considered polarization states though the "x-polarization" in principle has a very small y-component and vice versa.

5. Conclusion

For the first time, quasi error-free transmission of $10\,\mathrm{Gbit/s}$ digital data signals over a multimode photonic crystal fiber with $50\,\mu\mathrm{m}$ core diameter and as much as $100\,\mathrm{m}$ length has been demonstrated. With some optimizations concerning design and fabrication, these PCFs show good prospects as an alternative to graded-index fibers in optical datacom environments. Comparing to simulations, good agreement is found with the measured fiber bandwidths.

References

[1] N.A. Mortensen, M. Stach, J. Broeng, A. Petersson, H.R. Simonsen, and R. Michalzik, "Multi-mode photonic crystal fibers for VCSEL based data transmission," *Opt. Express*, vol. 11, pp. 1953–1959, 2003.

[2] R. Michalzik, K.J. Ebeling, M. Kicherer, F. Mederer, R. King, H. Unold, and R. Jäger, "High-performance VCSELs for optical data links," *IEICE Trans. Electron.*, vol. E84-C, pp. 629–638, 2001.

[3] P. Russell, "Review: photonic crystal fibers," *Science*, vol. 299, 2003.

[4] G.P. Agrawal, *Fiber-Optic Communication Systems*. New York: Wiley & Sons, 1997.

[5] R. Michalzik, F. Mederer, H. Roscher, M. Stach, H. Unold, D. Wiedenmann, R. King, M. Grabherr, and E. Kube, "Design and communication applications of short-wavelength VCSELs," *Proc. SPIE*, vol. 4905, pp. 310–321, 2002.

[6] S.G. Johnson and J.D. Joannopoulos, "Block-iterative frequency-domain methods for Maxwell's equations in a planewave basis," *Opt. Express*, vol. 8, pp. 173–190, 2001.

[7] J. Lægsgaard, A. Bjarklev, and S.E.B. Libori, "Chromatic dispersion in photonic crystal fibers: fast and accurate scheme for calculation," *J. Opt. Soc. Am. B*, vol. 20, 2003.

[8] A.K. Ghatak and K. Thyagarajan, *Introduction to Fiber Optics*. Cambridge: Cambridge University Press, 1998.

DFB Laser Integrated Electroabsorption Modulators

Philipp Gerlach*

The modulation bandwidth of traditional lumped electroabsorption modulators (EAMs) is usually limited by the RC time constant, but the effective resistance R and capacitance C are not easily extracted for advanced device geometries [1]. In this contribution, we investigate the modulator section of a 1.3 μm wavelength InP based distributed feedback (DFB) laser integrated EAM device fabricated by Infineon Technologies. The measured electro-optical response fits well with the result of a finite-difference simulation, allowing optimizations of the RC behavior.

1. Introduction
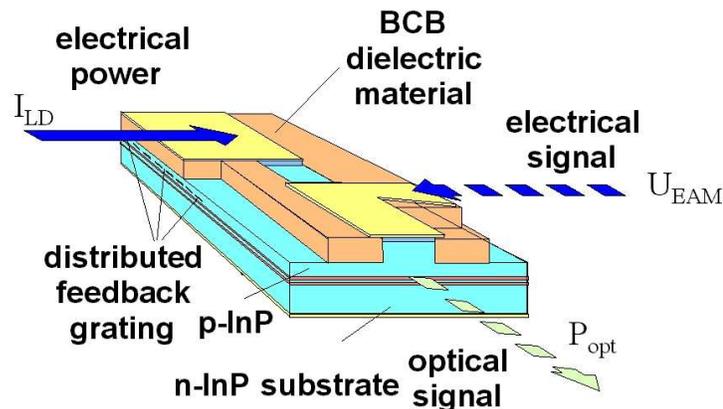
Fig. 1: Schematic illustration of a monolithically integrated DFB–EAM.

Because of the dispersion minimum of standard silica optical fibers, high-speed light sources at 1.3 μm wavelength are attractive especially for metropolitan area networks. DFB lasers monolithically integrated with EAMs are promising devices for this application space owing to their potential for high-speed operation at data rates in excess of 10 Gbit/s as well as low-cost fabrication capability [2]–[6].

The investigated device is a ridge-waveguide structure that consists of a laser section and a modulator section which are electrically isolated by etched trenches, as shown in Fig. 1. Both contain the same active region which has two different types of multiple
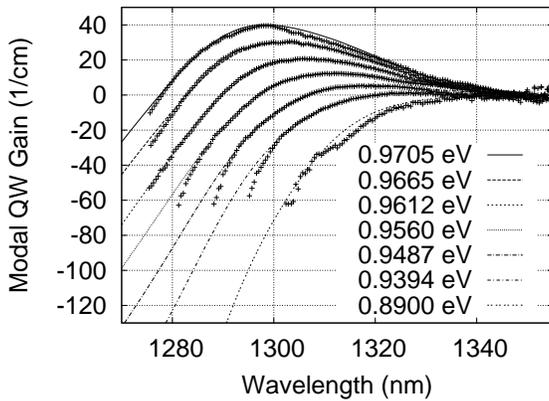
Fig. 2: Simulated (lines) and measured (crosses) modal gain spectra of the MQW structure for different quasi Fermi level separations.
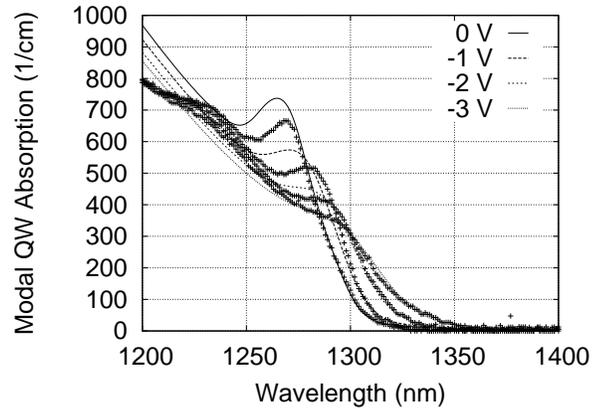
Fig. 3: Simulated (lines) and measured (crosses) absorption spectra of the MQW structure for different reverse bias voltages.

quantum wells (MQWs) [7]. Within the laser section the MQWs provide gain under forward bias. Simulations and measurements of the modal gain are illustrated in Fig. 2 [8]. The quantum-confined Stark effect enables absorption within the same MQWs in the modulator section under reverse bias, as demonstrated in Fig. 3.

The optical power

$$P_{\text{out}} = P_{\text{in}} \exp\left\{-\alpha_{\text{mod}} l_{\text{mod}}\right\}$$

which leaves the modulator section depends on the incoming optical power P_{in} that is generated in the laser section, the modulator length l_{mod} and the absorption coefficient α_{mod} which can be influenced by the reverse bias. Figure 4 demonstrates the typical static behavior of the single-mode fiber coupled optical output power of the combined device.
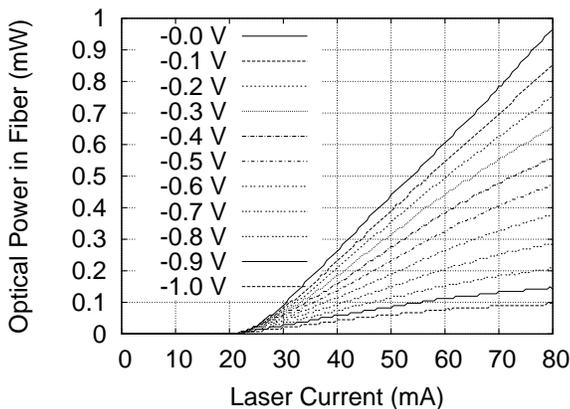
Fig. 4: Typical static behavior of a DFB–EAM. The optical power decreases with increasing reverse modulator voltage.
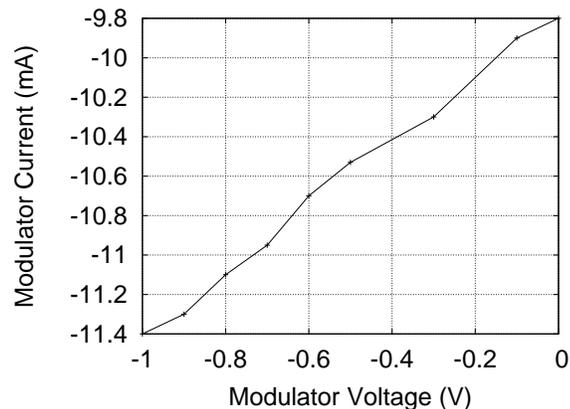
Fig. 5: Absorption current within the modulator section as a function of reverse modulator voltage.

The laser curves flatten with rising absorption due to increasing modulator reverse voltage. The optical power

$$P_{\mathrm{in}} - P_{\mathrm{out}} = P_{\mathrm{in}} \left(1 - \exp\left\{-\alpha_{\mathrm{mod}} l_{\mathrm{mod}}\right\}\right)$$

is absorbed in the modulator and generates the photocurrent

$$I_{\mathrm{mod}} = \eta_{\mathrm{mod}} \left(P_{\mathrm{in}} - P_{\mathrm{out}}\right) \frac{q}{\hbar\omega} = \eta_{\mathrm{mod}} P_{\mathrm{in}} \left(1 - \exp\left\{-\alpha_{\mathrm{mod}} l_{\mathrm{mod}}\right\}\right) \frac{q}{\hbar\omega} \,.$$

Parasitic losses of generated carriers are considered with the efficiency η_{mod}. The amount of light which is absorbed in the modulator section and therefore the absorption current I_{mod} increases with the reverse modulator voltage as shown in Fig. 5.

2. Electro-Optical Response
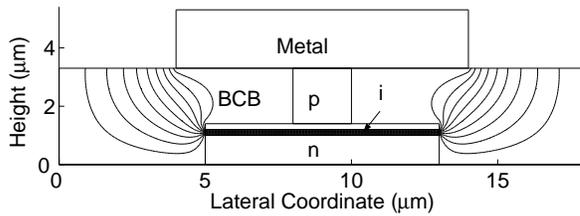
Fig. 6: Evenly spaced equipotential lines within the modulator section at 1 GHz modulation frequency.
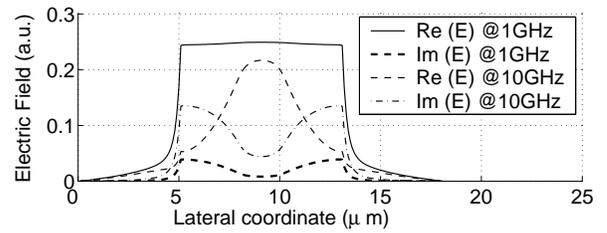
Fig. 7: Vertical component of the complex electric field in the intrinsic region of the modulator section at 1 and 10 GHz modulation.

In order to understand the modulation behavior of the EAM, two-dimensional simulations based on the finite-difference method have been performed to numerically solve the well-known continuity (Laplace) equation

$$\nabla_T \circ \vec{j} = \nabla_T \circ \left(\bar{\sigma}\vec{E}\right) = \nabla_T \circ \left(-\bar{\sigma}\nabla_T V\right) = 0$$

with complex conductivity $\bar{\sigma} = \sigma + \mathrm{i}\omega\epsilon_0$, current density $\vec{j} = (j_x,\, j_y)^T$, electric field $\vec{E} = (E_x,\, E_y)^T$ and quasi-static electric potential V. Assuming all values to be independent of the longitudinal coordinate z, the 2-D nabla operator $\nabla_T = (\partial/\partial x\,, \partial/\partial y)^T$ is used[*]. For a given voltage U_{mod}, the solution yields the electric field distribution $\vec{E}(\vec{r},\omega)$ and the impedance $Z_{\mathrm{mod}} = U_{\mathrm{mod}}/I$ with the Gaussian integral

$$I = \oint \vec{j} \circ \mathrm{d}\vec{A} = l_{\mathrm{mod}} \oint \vec{j} \circ \mathrm{d}\vec{s}$$

over the current density $\vec{j}$. Both $\vec{E}(\vec{r},\omega)$ and Z_{mod} are required to identify the limitations of the electro-optical response.

---

[*]Note that even at 10 GHz the wavelength of the modulating wave is about 1 cm and thus much longer than the typical length of the EAM.
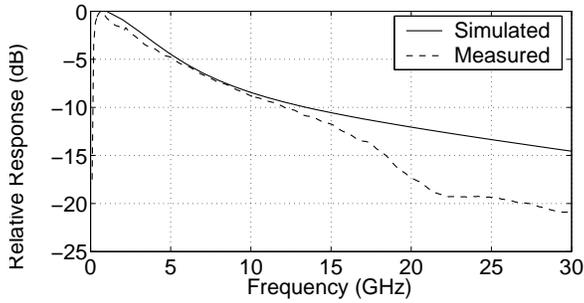
Fig. 8: Simulated and measured electro-optical responses of the EAM.
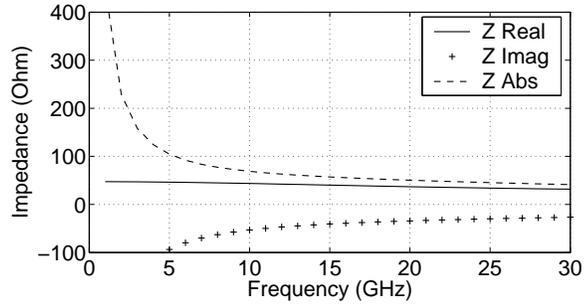
Fig. 9: Simulated complex impedance of the EAM.

In the present work, a $100\,\mu$m-long EAM with an $8\,\mu$m wide intrinsic region shown in Fig. 6 is analyzed. Simulated evenly spaced equipotential lines at $1\,$GHz modulation frequency pass through the intrinsic area and are drawn in the same diagram. The electric field in the intrinsic area is plotted in Fig. 7. As expected, at low frequencies, the electric field is rather homogeneous. With increasing frequency, the field concentrates in the center and phase shifts occur at the edges. The modulation phase is equal to the phase of the electric field and is thus not uniform across the intrinsic region. Overall, this strongly affects the shape of the modulation response (see Fig. 8), which is calculated with a Gaussian lateral optical intensity distribution and a detailed absorption model for the quantum wells.

Impedance variations shown in Fig. 9 (which are included in Fig. 8) in addition cause a decay of the response function since the modulator voltage

$$U_{\mathrm{mod}} = U_0 \, \frac{Z_{\mathrm{mod}}}{Z_{\mathrm{mod}} + 50\,\Omega}$$

approximately equals the generator voltage U_0 for $|Z_{\mathrm{mod}}| \gg 50\,\Omega$ but decreases by $3\,$dB for $|Z_{\mathrm{mod}}| \approx 50\,\Omega$, when assuming a commonly used $50\,\Omega$ system. None of these effects can be neglected.
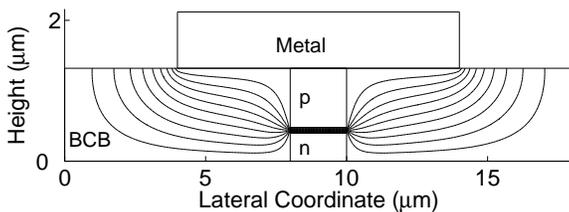
Fig. 10: Evenly spaced equipotential lines within optimized modulator section at $1\,$GHz modulation frequency.
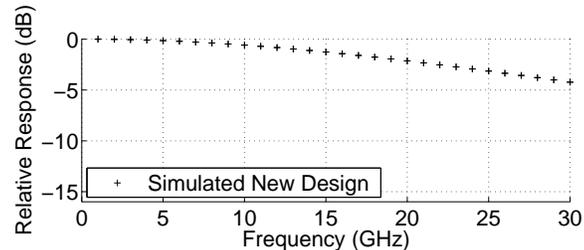
Fig. 11: Simulated electro-optical response of electroabsorption modulator with new design.

As shown in Fig. 8, measured and simulated electro-optical responses deviate by less than 2 dB for frequencies up to 15 GHz, indicating that the main reasons for the rapid decay of the response are included in the model. A distinct improvement is expected with a new design (see Fig. 10) incorporating a narrow intrinsic region. According to the simulated electro-optical response in Fig. 11, the 3 dB corner frequency should increase from 3 GHz in Fig. 8 to about 25 GHz, which could enable 40 Gbit/s operation [9].

3.   Conclusion

Monolithically integrated laser modulator structures fabricated by Infineon Technologies have been extensively investigated. The basic mode of operation has been verified and fits well to theoretical considerations. The optical output power and the absorption current can be controlled by the modulator voltage through the quantum-confined Stark effect. As Fig. 5 shows, the absorption current depends on the modulator voltage U_{mod}, but the residual absorption at present is rather high, as evidenced by the high current for $U_{\mathrm{mod}} = 0$. Since many carriers pile up and the electric field is screened, the modulation bandwidth degrades at higher laser currents [10, 11]. To avoid high residual absorption, a stronger detuning of the laser with respect to the bandgap of the MQWs in the modulator section is necessary. The measured modulation behavior of the investigated EAM is consistant with the simulation, indicating that the main reasons for the rapid decay of the response are included in the model. The flatness of the response curve is drastically affected by the capacity of the rather wide intrinsic region. Some possible solutions for this problem would be to decrease its width (as suggested in Figs. 10 and 11), shorten the length of the modulator section (which could reduce the achievable on-off ratio for digital modulation) or to increase the thickness of the undoped layers (which might incur limitations due to carrier transport times).

A future goal is to build a device with a narrow intrinsic region and larger detuning to decrease the residual absorption. According to simulation results, a significantly better modulation performance is then expected.

References

[1] R. Lewén, S. Irmscher, and U. Eriksson, "Microwave CAD circuit modeling of a traveling-wave electroabsorption modulator," *IEEE Trans. Microwave Theory Tech.*, vol. 51, no. 4, pp. 1117–1127, 2003.

[2] B. Stegmueller, E. Baur, and M. Kicherer, "1.55 µm and 1.3 µm DFB lasers integrated with electroabsorption modulators for high-speed transmission systems," in Proc. *Second Joint Symposium on Opto- and Microelectronic Devices and Circuits, SODC 2002*, pp. 95–99. Stuttgart, Germany, March 2002.

[3] R. Lewén, S. Irmscher, U. Westergren, L. Thylén, and U. Eriksson, "Ultra high-speed segmented traveling-wave electroabsorption modulators," in Proc. *Optical Fiber Communications Conf., OFC 2003*, Postdeadline paper PD38. Atlanta, GA, USA, February 2003.

[4] H. Kawanishi, Y. Yamauchi, N. Mineo, Y. Shibuya, H. Murai, K. Yamada, and H. Wada, "EAM-integrated DFB laser modules with more than 40-GHz bandwidth," *IEEE Photon. Technol. Lett.*, vol. 13, no. 9, pp. 954–956, 2001.

[5] M. Shirai, H. Arimoto, K. Watanabe, A. Taike, K. Shinoda, J. Shimizu, H. Sato, T. Ido, T. Tsuchia, M. Aoki, S. Tsuji, N. Sasada, S. Tada, and M. Okayasu, "40 Gbit/s electroabsorption modulators with impedance-controlled electrodes," *Electron. Lett.*, vol. 39, no. 9, pp. 733–735, 2003.

[6] B. Stegmueller, E. Baur, and M. Kicherer, "15 GHz modulation performance of integrated DFB laser diode EA modulator with identical multiple quantum well-double stack active layer," *IEEE Photon. Technol. Lett.*, vol. 14, no. 12, pp. 1647–1649, 2002.

[7] B. Stegmueller and C. Hanke, "High-frequency properties of $1.3\,\mu m$ and $1.55\,\mu m$ electro-absorption modulators integrated with DFB lasers based on identical MQW-double stack active layer," in Proc. *Lasers and Electro-Optics Society Ann. Meet., LEOS 2002*, vol. 1, pp. 115–116. Glasgow, Scotland, UK, November 2002.

[8] M. Peschke, T. Knoedl, and B. Stegmueller, "Simulation and design of an active MQW layer with high static gain and absorption modulation," in Proc. *Numerical Simulation of Semiconductor Devices, NUSOD 2003*, pp. 15–16. Tokyo, Japan, October 2003.

[9] P. Gerlach, M. Peschke, and R. Michalzik, "High-frequency performance optimization of DFB laser integrated electroabsorption modulators," in Proc. *Semiconductor and Integrated Opto-Electronics Conference, SIOE 2004*, paper 41. Cardiff, Wales, UK, April 2004.

[10] T. Ido, H. Sano, S. Tanaka, and H. Inoue, "Frequency-domain measurement of carrier escape times in MQW electroabsorption optical modulators," *IEEE Photon. Technol. Lett.*, vol. 7, no. 12, pp. 1421–1423, 1995.

[11] B. Stegmueller and C. Hanke, "Integrated $1.3\,\mu m$ DFB laser electroabsorption modulator based on identical MWQ double-stack active layer with 25 GHz modulation performance," *IEEE Photon. Technol. Lett.*, vol. 15, no. 8, pp. 1029–1031, 2003.

Thermal Crosstalk in Integrated Laser Modulators

Martin Peschke[*]

A monolithically integrated distributed feedback laser with an electroabsorption modulator has been investigated which shows a red-shift of the emission wavelength with applied modulator bias voltage. This leads to an adiabatic chirp parameter α_H of up to 0.13 that usually equals zero for decoupled devices like hybrid integrations of laser and modulator. By means of measurements and corresponding simulations, the phenomenon has been identified to be caused by thermal coupling between the sections.

1. Introduction

Integrated distributed feedback (DFB) laser diodes and electroabsorption modulators (EAMs) are an attractive alternative for building electrooptical converters for 1300 nm and 1550 nm wavelength as they combine the benefits of a stand-alone EAM with those of a directly modulated solitary laser. High modulation frequencies, low or even negative chirp parameters [1] and low driving voltages [2] compared to other modulator types can be achieved without the problems of high insertion loss, high packaging costs [3] and polarization dependence.

In contrast to hybrid laser modulator solutions, the different sections of an integrated device cannot be considered to be independent of each other in general. Due to the strong optical coupling between laser and EAM, reflections from the EAM can cause optical feedback. The electrical separation of the sections is usually done by ion implantation [4], etched trenches [5] or local zinc diffusion [6], but insufficient longitudinal ohmic resistances may lead to electrical crosstalk. Finally, the spatial proximity of the sections can result in thermal crosstalk [7], meaning a temperature change in one section caused by heat generation in the other.

All these effects may reduce the static and dynamic performance drastically compared to decoupled devices. For example, the adiabatic chirp parameter of a stand-alone EAM is zero. This advantage over directly modulated lasers is diminished in integrated DFB–EAM devices where a finite wavelength shift is observed with applied modulator bias voltage, as illustrated in Fig. 1.

This contribution investigates the effect of wavelength shift with modulator voltage by measurement and simulation. Special emphasis is put on the measurement method that was chosen in order to evaluate the different feedback and crosstalk mechanisms. After identifying the phenomenon as thermal crosstalk, a suitable model was developed to confirm this idea.
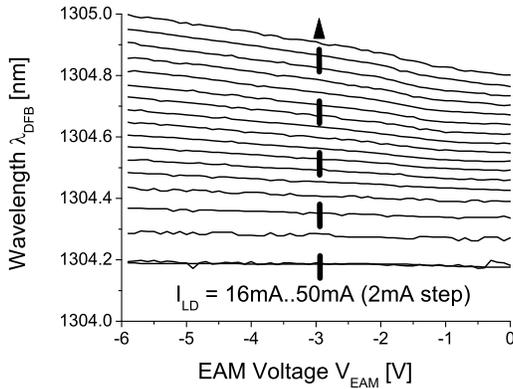
Fig. 1: DFB peak wavelength for different laser currents versus modulator voltage under continuous wave operation at room temperature.
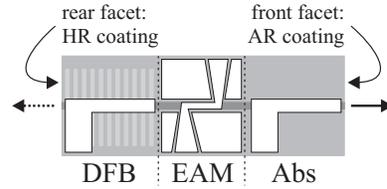
Fig. 2: Top view of the contact design of the device under test. Separations between device sections are indicated by dashed lines.

2.   Device and Measurement Setup

The investigations have been carried out on a monolithically integrated DFB–EAM with an absorber section. The device's contact layout is displayed in Fig. 2. A detailed report on the fabrication steps is given in Ref. [6]. The active area consists of an epitaxially grown AlGaInAs on InP double QW stack that is able to deliver high gain for forward current injection and high absorption swing with reverse voltage at 1305 nm operation wavelength [8]. A local buried grating is introduced in the DFB section. Three different contacts that are indicated as DFB (length $L_{\mathrm{DFB}} = 370\,\mu\mathrm{m}$), EAM ($L_{\mathrm{EAM}} = 130\,\mu\mathrm{m}$) and Abs (500 μm long) are aligned along a ridge waveguide. Etched trenches at the dashed lines separate the sections electrically [5]. The rear facet is high-reflection (HR) coated, the front facet anti-reflection (AR) coated. Under standard operation, the absorbing region is either omitted in simplified devices or forward biased to act as an additional semiconductor optical amplifier (SOA). Intensity modulated light is emitted at the front facet.

In this work, the peak wavelength λ_{DFB} is measured at the rear facet where the intensity level is independent of the EAM bias and always well above the noise margin. Furthermore, the long absorbing section avoids reflections from the front facet.

3.   Measurement Results

In order to explain the results of Fig. 1 and to evaluate the dominating influence, at first the separation resistances between the segments were measured. They were well above 25 kΩ for all trenches. For a 0 to −5 V voltage change at the EAM, the laser current is reduced by less than 0.2 mA. From Fig. 1, a constant wavelength reduction of 0.01 nm

would be expected. In contrast, a positive wavelength shift was measured exhibiting a steeper slope of $\lambda_{\mathrm{DFB}} = \lambda_{\mathrm{DFB}}(V_{\mathrm{EAM}})$ with rising laser current.

The second source for DFB tuning could be an optical reflection with altering magnitude and phase due to the change of refractive index and absorption coefficient in the EAM section. However, there are arguments objecting optical feedback. First, the combination of absorber and AR coating is expected to provide at least 80 dB reflection suppression. Second, the optical power level at the rear facet is independent of the modulator voltage.

To examine the thermal issues, the same measurement was done again but this time driving the laser in pulse rather than in continuous wave (CW) mode. The pulse length was 1 µs, the duty cycle 1:100. The result is shown in Fig. 3. Now, the voltage dependence of the DFB wavelength has vanished. Note that the pulse length is rather long, which leads to a slight shift of the laser wavelength with laser current. This laser self-heating takes place on much faster time scales than thermal crosstalk due to the limited thermal spreading velocity. From the absorption change in the EAM and the maximum wavelength shift in the DFB, an adiabatic chirp parameter $\alpha_{\mathrm{H},0-6\mathrm{V}} = \Delta n_{\mathrm{r,DFB}}/\Delta n_{\mathrm{i,EAM}} = 0.13$ is obtained for the device, with $n_{\mathrm{r,DFB}}$ and $n_{\mathrm{i,EAM}}$ being the real and imaginary part of the complex refractive index in the DFB and EAM sections, respectively.

4.   Thermal Crosstalk Model

The thermal crosstalk phenomenon was simulated by a 3D finite element method (FEM) using the commercial software FEMLAB. The cross-section of the InP substrate with a thermal conductivity of $\kappa = 68\ \mathrm{W/(Km)}$ [9] was 130 µm thick and 100 µm wide.

The underlying differential equation was the standard heat transport equation for the
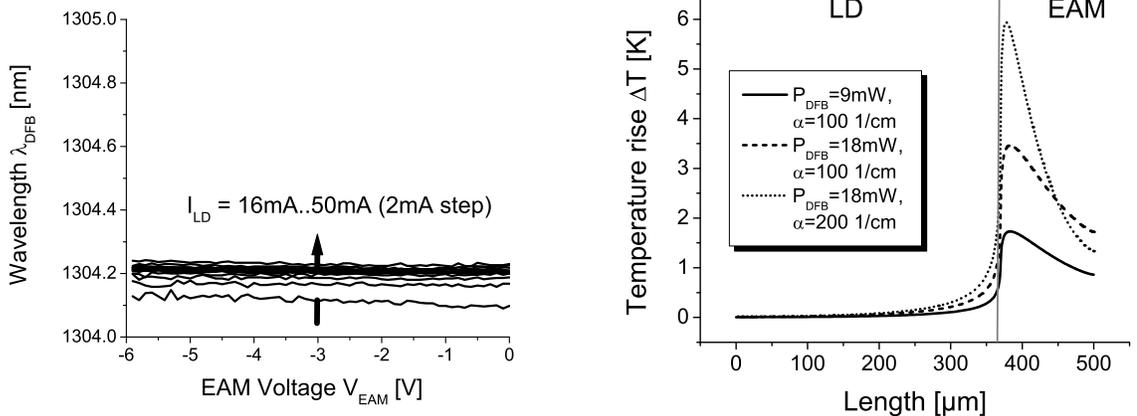
Fig. 3: The same measurement as in Fig. 1, here in pulsed operation.

Fig. 4: Temperature rise along the DFB–EAM axis by EAM heating.

temperature T [10], namely

$$-\nabla \left(\kappa \nabla T \right) = Q_i \tag{1}$$

with $i \in [\mathrm{DFB}, \mathrm{EAM}]$ for the laser and modulator sections, respectively. The dissipated heat power densities are

$$Q_{\mathrm{DFB}} = \frac{1}{d_{\mathrm{pn}}} \left(V_{\mathrm{DFB}} j_{\mathrm{DFB}} - \frac{P_{\mathrm{DFB}}}{w \, L_{\mathrm{DFB}}} \right) , \tag{2}$$

$$Q_{\mathrm{EAM}} = \frac{1}{d_{\mathrm{pn}}} \left(V_{\mathrm{EAM}} + \frac{\hbar\omega}{q} \right) j_{\mathrm{EAM}} , \tag{3}$$

assuming a constant power density within the DFB section. Here, V_i are the voltages across the intrinsic region of thickness d_{pn}, j_i are the corresponding current densities, P_{DFB} is the total emitted light from the laser diode and $w = 4\,\mu\mathrm{m}$ is the width of the active region. Equation (3) takes into account that after their creation by an absorption process, carriers lose the combined energy of bandgap plus external voltage due to scattering processes while escaping the undoped region.

The current density in the laser j_{DFB} is assumed to be constant while the current in the EAM section j_{EAM} reduces exponentially with the light intensity as

$$j_{\mathrm{EAM}}(x) = \frac{q}{\hbar\omega} \frac{1}{w} \, \alpha \, P_{\mathrm{DFB}} \, e^{-\alpha x} , \tag{4}$$

where the absorption coefficient α depends on the applied voltage. For simplicity, all light generated in the DFB is assumed to couple into the EAM.

In order to separate self-heating and thermal crosstalk effects, two different simulations were done with only one heat source Q_i active at a time. In both cases, the average temperature rise ΔT_i in the heating section was monitored as well as the average temperature rise in the passive section due to heat transfer. Figure 4 shows the temperature along the active area for different parameters with the modulator as heat source. Higher optical input and higher absorption increase the temperature in particular close to the DFB–EAM interface.

Thermal "scattering parameters" were defined, describing the self-heating of the sections as well as the thermal crosstalk in terms of

$$\begin{pmatrix} \Delta \bar{T}_{\mathrm{DFB}} \\ \Delta \bar{T}_{\mathrm{EAM}} \end{pmatrix} = \begin{pmatrix} s_{11} & s_{12}(\alpha) \\ s_{21} & s_{22}(\alpha) \end{pmatrix} \begin{pmatrix} I_{\mathrm{DFB}} V_{\mathrm{DFB}} - P_{\mathrm{DFB}} \\ (qV_{\mathrm{EAM}}/\hbar\omega + 1) \, \alpha \, P_{\mathrm{DFB}} \end{pmatrix} \quad \text{with} \tag{5}$$

$$s_{11} = 84 \text{ K/W} , \tag{6}$$

$$s_{21} = 13 \text{ K/W} , \tag{7}$$

$$s_{22} = \left(0.325 + 2.01 \cdot e^{-\alpha \cdot \mathrm{cm}/139} \right) \frac{\mathrm{K\,cm}}{\mathrm{W}} , \tag{8}$$

$$s_{12} = \frac{s_{22}}{7.75 + 14.75 \cdot e^{-\alpha \cdot \mathrm{cm}/288}} . \tag{9}$$

After deriving the thermal scattering matrix from the 3D simulation, the result was used (together with a simple laser model) to generate graphs similar to Fig. 1. Parameters for the characteristic equations are the threshold current $I_{\text{th}} = 18\,\text{mA}$, the slope efficiency at the DFB–EAM intersection $\Delta P/\Delta I = 0.4\,\text{W/A}$, the kink voltage $V_0 = 0.95\,\text{V}$, the laser series resistance $R_{\text{S}} = 8\,\Omega$, the voltage-dependent absorption coefficient $\alpha \cdot \text{cm} = 600 - 450\,\text{V}/(V_{\text{EAM}} + 1\,\text{V})$ and the thermal wavelength shift $\Delta\lambda_{\text{DFB}}/\Delta T = 0.1\,\text{nm/K}$. They were taken from measurement data of the integrated DFB-EAM, material simulation and large-area test devices for absorption measurements [8].

As Fig. 5 indicates, the simulation is in good agreement with the measurement results. Higher average laser temperatures are caused by higher optical output power as well as higher absorption. However, the calculated wavelength shift is smaller than in reality by about 25 %. This discrepancy is attributed to non-ideal thermal coupling of the chip to the heat sink and the lack of self-consistency of the simulation. In the experiment, higher EAM temperatures lead to higher absorption, further amplifying the thermal heating. This positive feedback can even lead to the destruction of integrated devices in the EAM section.
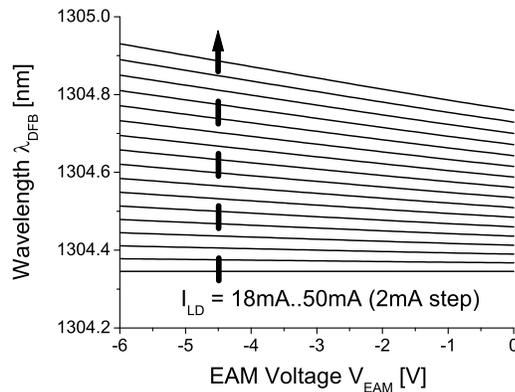
Fig. 5: Simulated wavelength shift due to modulator-induced heating and laser self-heating.

5. Conclusion

Measurements on an integrated laser modulator were presented showing a shift of the DFB wavelength with applied modulator bias. This leads to a non-zero adiabatic chirp parameter compared to stand-alone laser modulator solutions. By measurement and simulation, the behavior was identified to be caused by thermal crosstalk. Increasing the EAM bias leads to a super-linear rise of dissipated power in the EAM, heating up the modulator and reaching out into the laser section. There, the refractive index and consequently the DFB wavelength is altered due to the average temperature rise. As

thermal crosstalk takes place on much longer timescales (above $1\,\mu$s) compared to the typical modulation speed in the GHz regime, the effect is expected to disappear under high-frequency operation.

References

[1] R. Salvatore, R. Sahara, M. Bock, and I. Libenzon, "Electroabsorption modulated laser for long transmission spans," *IEEE J. Quantum Electron.*, vol. 38, no. 5, pp. 464–476, 2002.

[2] K. Wakita and I. Kotaka, "Multiple-quantum-well optical modulators and their monolithic integration with DFB lasers for optical fiber communications," *Microwave and Optical Technol. Lett.*, vol. 7, no. 3, pp. 120–128, 1994.

[3] H. Takeuchi, K. Tsuzuki, K. Sato, M. Yamamoto, Y. Itaya, A. Sano, M. Yoneyama, and T. Otsuji, "Very high speed light source module up to $40\,$Gb/s containing an MQW electroabsorption modulator integrated with a DFB laser," *IEEE J. Selected Topics Quantum Electron.*, vol. 3, no. 2, pp. 336–343, 1997.

[4] A. Ramdane, F. Devaux, N. Souli, D. Delprat, and Ougazzaden, "Monolithic integration of multi-quantum-well lasers and modulators for high-speed transmission," *IEEE J. Selected Topics Quantum Electron.*, vol. 2, no. 2, pp. 326–335, 1996.

[5] R. Schreiner, P. Nagele, M. Korbl, A. Groning, J. Gentner, and H. Schweizer, "Monolithically integrated tunable laterally coupled distributed-feedback lasers," *IEEE Photon. Technol. Lett.*, vol. 13, no. 12, pp. 1277–1279, 2001.

[6] B. Stegmueller and C. Hanke, "Integrated $1.3\,\mu$m DFB laser electroabsorption modulator based on identical MQW double-stack active layer with $25\,$GHz modulation performance," *IEEE Photon. Technol. Lett.*, vol. 15, no. 8, pp. 1029–1031, 2003.

[7] M. Suzuki, H. Tanaka, H. Taga, S. Yamamoto, and Y. Matsushima, "$\lambda/4$ shifted DFB laser / electroabsorption modulator integrated light source for multigigabit transmission," *IEEE J. Lightwave Technol.*, vol. 10, no. 1, pp. 90–95, 1992.

[8] M. Peschke, T. Knoedl, and B. Stegmueller, "Simulation and design of an active MQW layer with high static gain and absorption modulation," in Proc. *Numerical Simulation of Semiconductor Devices, NUSOD 2003*, pp. 15–16. Tokyo, Japan, October 2003.

[9] J. Piprek, *Semiconductor Optoelectronic Devices.* San Diego, CA, USA: Academic Press, 2003.

[10] S. Murata, H. Nakada, and T. Abe, "Theoretical and experimental evaluation of the effect of adding a heat bypass structure to a laser diode array," *Jpn. J. Appl. Phys.*, vol. 32, no. 3A, pp. 1112–1119, 1993.

Investigations of the Carrier Gas Composition for HVPE of GaN

Frank Habel

We upgraded our HVPE (Hydride Vapor Phase Epitaxy) system for GaN by adding a hydrogen line so that not only pure nitrogen can be used as carrier gas but also a mixture of nitrogen and hydrogen. This modification lead to a significant improvement of the layer quality. The grown layers are 140 μm thick, crack-free and show a mirror like surface. A width of the XRD rocking curve of 115 arcsec was determined. Hall measurements showed a carrier concentration of $7 \times 10^{15} \, cm^{-3}$ and a mobility above $700 \, cm^2/V\,s$ at room temperature.

1. Introduction

The development of substrates for GaN based devices is a topic of increasing importance as the lifetime and performance of recent devices like laser diodes, UV emitting LEDs or FETs require high-quality substrates. Usual GaN layers grown on foreign substrates have a high dislocation density in the order of 10^8-$10^{10} \, cm^{-2}$ thus reducing the carrier mobility, the efficiency in optoelectronic devices and the homogeneity of the grown structures. A big improvement can be achieved by applying methods to reduce the dislocation density like the epitaxial growth on structured substrates. However, the perfect solution is the homoepitaxial growth on GaN substrates. For the production of GaN substrates the Hydride Vapor Phase Epitaxy (HVPE) is the most promising technique due to it's capability to grow high-quality GaN layers with a growth rate of up to $100 \, \mu$m/h.

2. Basics of Hydride Vapor Phase Epitaxy

For HVPE gallium metal is used as group III precursor. At a temperature between $800 \, °$C and $900 \, °$C the liquid gallium reacts with hydrogen chloride (HCl) and forms gallium chloride (1). On the wafer gallium chloride and the group V precursor ammonia (NH_3) react to gallium nitride (2).

$$Ga(l) + HCl(g) \rightleftharpoons GaCl(g) + \frac{1}{2}H_2(g) \tag{1}$$

$$NH_3(g) + GaCl(g) \rightleftharpoons GaN + HCl(g) + H_2(g) \tag{2}$$
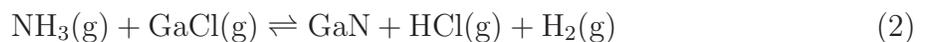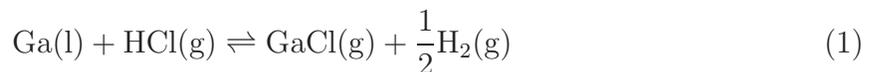
The growth temperature is between $1000 \, °$C and $1100 \, °$C. A commercially available Aixtron hot wall quartz reactor with a horizontal gas flow was used.
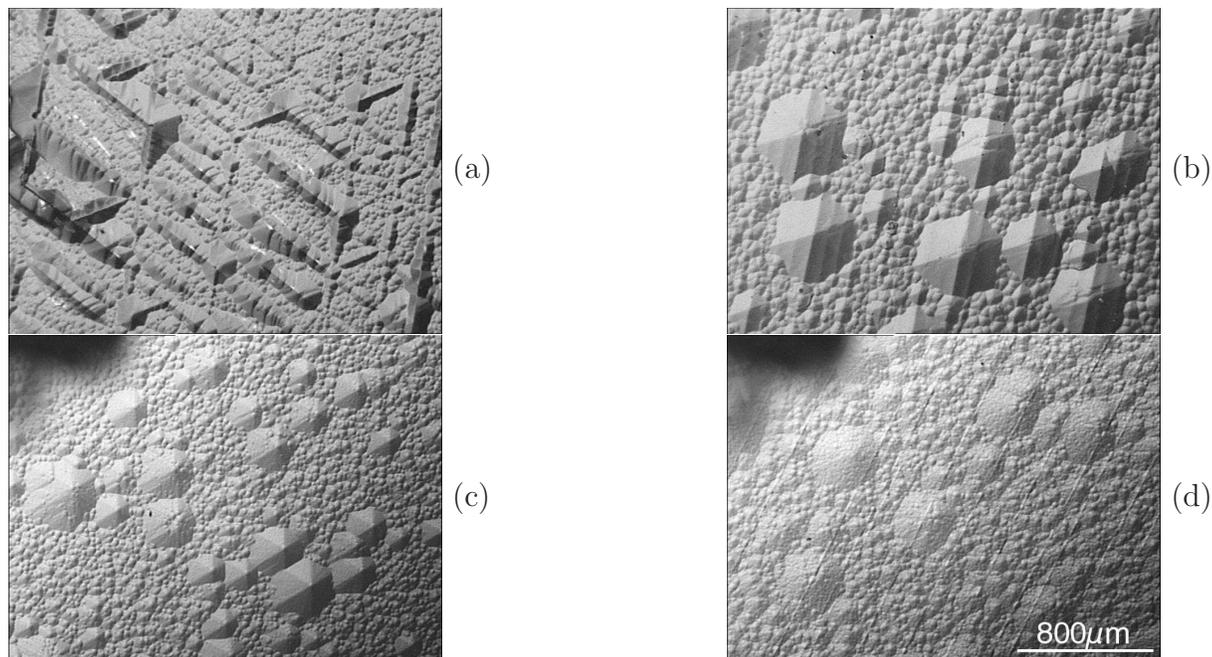
Fig. 1: Effect of the carrier gas composition on the surface morphology for a hydrogen concentration of 0% (a), 25% (b), 51% (c) and 80% (d). Only sample (c) is crack free.

3.   Experiments

For all growth runs a $1.5\,\mu$m thick MOVPE GaN layers on sapphire were used as templates. The growth temperature was kept at $1060\,°$C and the reactor pressure was 900 mbar unless noted otherwise.

3.1   Carrier gas composition

For MOVPE nitrogen and hydrogen are used as carrier gas and it is a well known fact that the choice of the carrier gas affects the properties of the grown layer. For HVPE hydrogen must not be regarded as an inert carrier gas because hydrogen is directly involved in the growth reactions as Chlorine is removed from the crystal surface by a reaction to HCl (see equation 2). Therefore a strong impact of the carrier gas composition must be expected.

In our HVPE system nitrogen is used as standard carrier gas. A new hydrogen line was added allowing to vary the gas composition inside the reactor. Figure 1 shows a series of samples grown with different carrier gas composition. The growth time was kept constant at 30 minutes. With pure nitrogen a severe cracking of the GaN layer occurs (Fig. 1a). Cracking can be reduced by adding hydrogen. On the sample with a hydrogen concentration of 51% no cracks were found at all (Fig. 1c). For even higher hydrogen concentrations the cracks reappear (Fig. 1d). Another effect on the sample morphology is that the number and size of hexagonal pyramids on the surface is reduced with increasing

hydrogen concentration. The growth rate on the other hand was reduced from $74\,\mu$m/h for pure nitrogen to $30\,\mu$m/h for 80% hydrogen (Fig. 2).
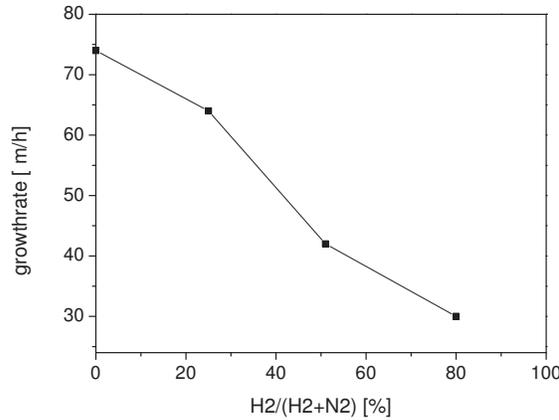
Fig. 2: Decreasing growth rate with increasing hydrogen content.
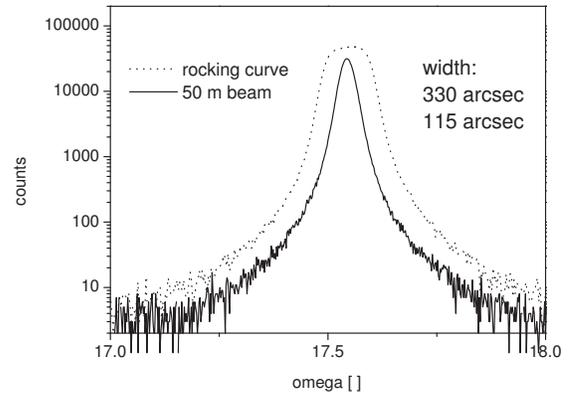
Fig. 3: XRD rocking curve.

3.2 V-III ratio

After the optimization of the carrier gas composition, the V-III ratio was re-adjusted. A sample series with V-III ratios of 15, 45 and 100 was grown by varying the ammonia flow. This parameter has a significant impact on the growth rate, which changed from $16\,\mu$m/h to $30\,\mu$m/h and $38\,\mu$m/h. For the higher V-III values the surface morphology remained almost constant, whereas for the lowest value an upcoming coarse pattern replaced the typical fine structure.

3.3 Reactor pressure

The effect of the reactor pressure was also investigated. Samples were grown at 900 mbar, at 500 mbar and at 200 mbar. Again a decrease in the growth rate was found. The corresponding values were $20\,\mu$m/h, $17\,\mu$m/h and $12\,\mu$m/h. A roughening of the surface was found for decreasing reactor pressure.

3.4 Overall results: high-quality thick GaN layers

Based on the described experiment we increased the growth time to 2 hours and realized completely crack free 2 inch HVPE GaN layers with a thickness of $140\,\mu$m and a mirror like surface (Fig. 4). Because of the mismatch in the thermal expansion coefficients a bowing of the structure was found. In the middle of the wafer a rise of $530\,\mu$m was measured, corresponding to a bowing radius of about 2.5 m. In figure 3 the XRD rocking
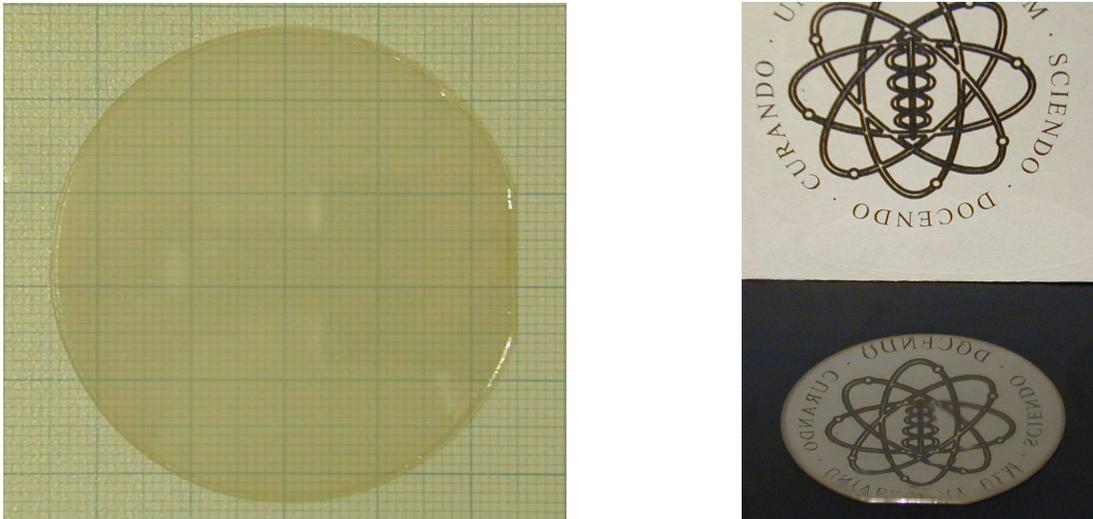
Fig. 4: 140μm thick crack-free HVPE sample with mirror-like surface.

curve of such a sample is plotted. The width is 330 arcsec. This plot is broadened by the bowing of the wafer, as the x-ray beam has a certain spot size. Using a 1 mm x-ray beam a broadening of almost 100 arcsec has to be taken into account. Therefore the XRD measurement was repeated with x-ray beam width of 50 μm, leading to a reduced width of 115 arcsec. The samples show also excellent electrical properties. At 300 K a carrier concentration of $7.2{\times}10^{15}$ cm^{-3} and a mobility of 719 cm^2/Vs was measured, at 77 K the carrier concentration was $2.8{\times}10^{15}$ cm^{-3} and the mobility was 1780 cm^2/Vs. A low dislocation density of 9×10^7cm^{-2} was determined by HCl etching technique [1], although no special method was used to reduce the dislocation density so far.

4.   Conclusion

The use of a combination of hydrogen and nitrogen as carrier gas lead to a significant improvement of the HVPE grown GaN layers. Up to now crack free 2 inch samples with a thickness of 140 μm have been realized and the critical thickness has not been reached in contrast to a critical thickness of about 20 μm for growth in pure nitrogen atmosphere. The samples show a mirror like surface and excellent properties like XRD rocking curve width of 115 arcsec, a background carrier concentration of $7.2{\times}10^{15}$ cm^{-3} and a mobility of 719 cm^2/Vs.

References

[1] F. Habel and M. Seyboth, "Determination of dislocation density in epitaxially grown GaN using an HCl etching process," *phys. stat. sol. (c)*, vol. 0, no. 7, p. 2448, 2003.

Microsecond Timescale Lateral-Mode Dynamics in a Narrow Stripe InGaN-Laser

Christoph Eichler

Time-resolved measurements of spectra and far-fields of InGaN-based laser diodes show lateral mode changes and gradual tilting of the far-field on a microsecond timescale. Numerical simulations based on a microscopic theory are in good agreement with the measurements. The observed effects are attributed to lateral carrier diffusion in combination with thermal lensing.

1.   Introduction

For violet-blue diode lasers, there exist several important applications, such as optical storage and laser printing, requiring lateral mode stability. While the design of single-mode lasers is an ongoing problem, the underlying physical mechanisms leading to stable fundamental-lateral mode operation in conventional semiconductor lasers is, in principle, well understood. However, this understanding may not apply to the wide-bandgap group-III nitride (III-N) material system because of its drastically different physical properties [1]. That this is indeed the case is demonstrated in our recent observation of lateral-mode instabilities on a microsecond time scale in a narrow ($2.25\,\mu$m wide) ridge-waveguide InGaN laser.

2.   Experimental

The investigated laser diodes were fabricated by OSRAM Opto Semiconductors. They were grown on SiC-substrate without ELO-techniques by metal organic chemical vapor deposition and consist of a $560\,$nm thick AlGaN:Si cladding, followed by a $120\,$nm GaN:Si lower waveguide layer, three $2\,$nm $In_{0.1}Ga_{0.9}N$/GaN quantum wells with GaN:Si barriers, an $Al_{0.2}Ga_{0.8}N$ electron blocking layer, a $100\,$nm thick GaN:Mg upper waveguide layer, and a $400\,$nm thick AlGaN:Mg upper cladding layer. Contacts are deposited on a p-GaN cap layer on top of the ridge and on the n-SiC backside. The cleaved facets are coated with high reflectivity coating (R$\sim$98%/70%) [2]. The devices are operated in junction side up configuration, which is possible due to the SiC substrate. Since we use short pulses in the microsecond range, the back contact of the device does not see a temperature increase during the pulse, as shown in Ref. [3]. After each pulse, the laser has enough time to cool down again due to the very low duty cycle. Thus, the kind of mounting the device onto the heatsink has only negligible influence on the effects described in this letter.
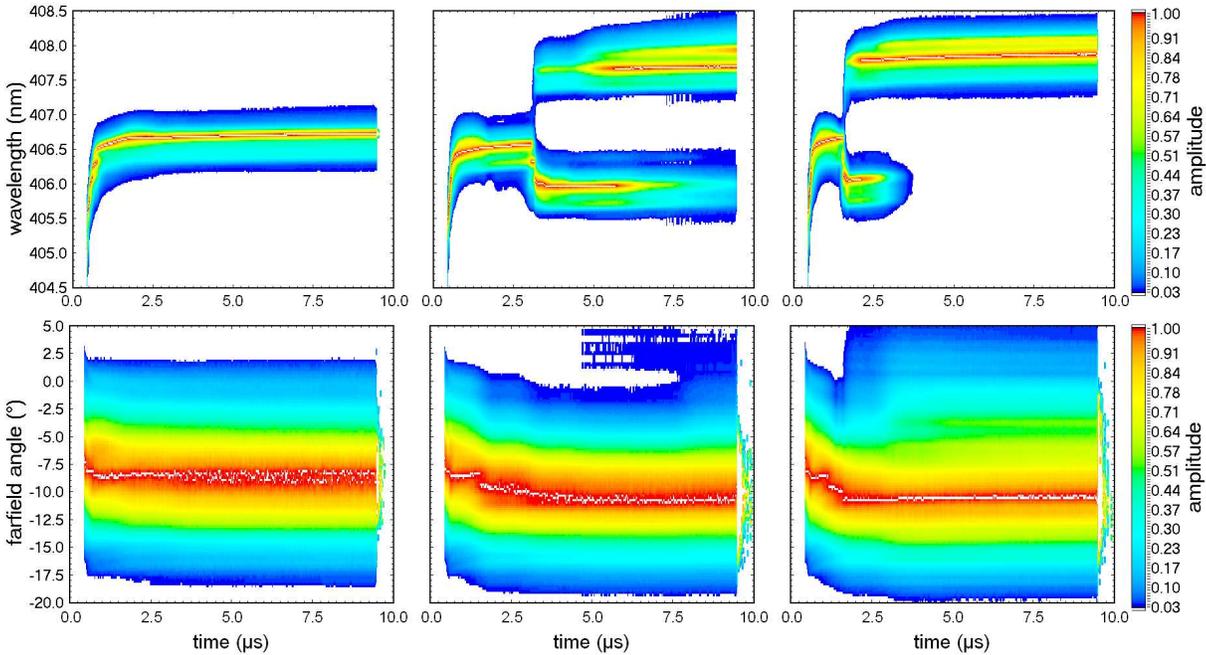
Fig. 1: A $2.25\,\mu$m wide InGaN-laser diode at injection currents of $1.08\cdot I_{\mathrm{th}}$ (left), $1.16\cdot I_{\mathrm{th}}$ (middle), and $1.20\cdot I_{\mathrm{th}}$ (right). The spectrum becomes bi-modal at higher currents and the far-field shows a pronounced beam-steering effect.

For measurements of the time-resolved optical spectrum, the light of the temperature stabilized laser diode is collimated and then focussed on the entrance slit of a grating monochromator. At the output slit, the light of the actually selected wavelength is collected by a fast photomultiplier tube. Thus, for this particular wavelength the intensity distribution versus time can be observed on an oscilloscope connected to the photomultiplier tube. Scanning the selected wavelength of the monochromator over the range of the emission spectrum of the laser diode yields therefore a 3-dimensional graphics with time and wavelength as x- and y-axis, respectively, and optical intensity as z-axis (color encoded). This plot which is shown in figure 1 (top) allows to observe the evolution of the laser spectrum during a current pulse. The corresponding time-resolved far-field is measured in the same manner. The only difference to the previous measurement is that the monochromator is now replaced by a step motor controlled arm which moves the pigtail of a multimode fiber on a circular path around the emitting facet of the laser diode. The light collected by the fiber is again measured by the photomultiplier tube. An example of such a far-field measurement is shown in figure 1 (bottom).

In order to get some insight into the mechanism of their modal behavior, we analyzed laser diodes with different ridge widths and at different measurement conditions. A typical spectrum and far-field of a $2.25\,\mu$m wide stripe laser is shown in figure 1. In this case, current pulses of $9\,\mu$s length at a very low duty cycle of $0.1\,\%$ were used to excite the laser. Let us first concentrate on figure 1 (left). It is evident that the laser turns on

and immediately starts to heat up, as indicated by the large wavelength shift. After approximately $1\,\mu$s, the wavelength shift slows down indicating that the laser diode has reached an almost constant temperature distribution. Beyond this point, the effect of the heat capacity of the materials round the active area becomes less important and the temperature increase is dominated by the internal thermal resistance of the device [3]. The far-field also shows a small change within the first microsecond, but then stays constant for the rest of the pulse. For slightly higher currents (figure 1 middle) and after approximately $1\,\mu$s the laser enters a transition regime: A second wavelength starts to appear and an increasingly asymmetric far-field distribution is observed. After a certain time $(2.66\,\mu$s$)$ which is characteristic for this particular injection current density, the laser shows an abrupt change in both the spectral and the far-field behavior. Beyond this point, it lases suddenly in two lateral modes. This behavior is even more pronounced when the current density is further increased. As shown in figure 1 (right), the splitting into two modes occurs already after $1.11\,\mu$s. In pulsed L-I-curves, this mode switching is clearly visible as a kink.

3. Modelling

There exist two possible explanations for the mode switching: one is the temperature induced change of the refractive index. Since the number of guided modes m depends on the difference between the refractive index of the waveguide n_f and the surrounding material n_s [4], a temperature raise underneath the ridge results in an increase of the refractive index, leading to a better guiding of higher order modes. However, since the highest temperature is found in the center of the ridge, the resulting refractive index change alone is not sufficient to explain the tilting of the far-field.

To explore as to whether the experimental observations can also originate from intrinsic properties of the III-nitride material system, the laser structure is modeled using the coupled Maxwell-semiconductor-Bloch equations. These equations treat the wave-optical (diffractive) aspect of the intracavity laser field, and provide a microscopic description of InGaN quantum-well susceptibility [1]. We numerically solve these equations simultaneously with a partial differential equation $(x$, z and $t)$ that accounts for carrier diffusion effects on the total carrier density spatial distribution. Figure 2 shows (from left to right) the changes in the laser field with increasing injection current. The top two rows depict the lateral laser field intensity and phase at the output facet. Note the abrupt transition from a plane phase front to one with appreciable tilt. A consequence of the phase-front tilt is beam steering as evident from the lateral displacement of the far-field intensity maximum (see third row, Fig. 2).

The theoretical results may be traced to the co-existence of carrier-induced refractive index change and lateral carrier diffusion. Basically, an increase in injection current gives rise to a broader pumped region at the quantum well because of increased lateral carrier diffusion. The effects of this active region broadening is accentuated by spatial hole burning, which in a semiconductor causes an increase in the index guiding of the intracavity mode. The
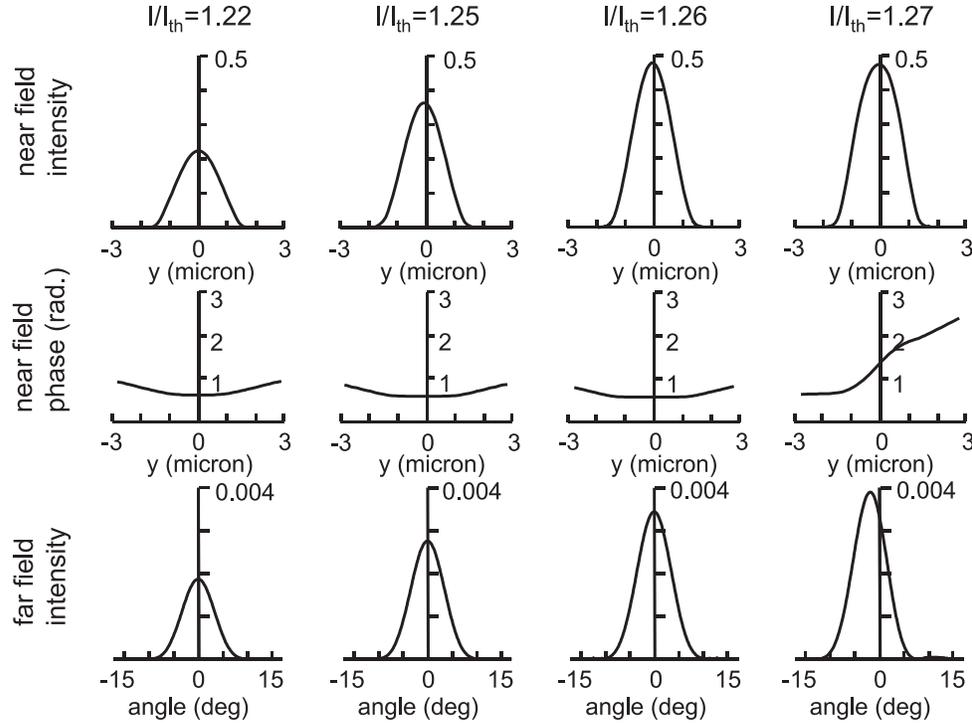
Fig. 2: Near field intensity, near field phase, and far-field distribution of InGaN laser diodes at different currents. In the far-field, a tilt of about -2 degrees is clearly visible for a current of $1.27 \cdot I_{\text{th}}$. For smaller currents, no tilt can be observed.

combination of a wider gain region and a stronger index confinement leads to the transition from operation with the fundamental mode to one with a tilted single-lobe mode. Our simulations show that the onset of tilted mode operation depends on the filamentation (self-focusing) strength of the quantum-well gain structure. Compared to typical near-infrared QW lasers, the antiguiding (self-focusing) factor R in 2 nm InGaN quantum wells is a factor of three higher, primarily because of the significantly heavier electron and hole effective masses in nitride semiconductors [1].

We also find a direct correspondence between beam steering and the effective pumped width as indicated in Fig. 3. The effective pumped width is the full width at half maximum of the computed carrier distribution at the quantum well, where the difference between this width and the stripe width is due to lateral carrier diffusion during carrier transport from the electrodes to the quantum well. The curve shows qualitative agreement with the experiment (compare with inset), and that beam steering occurs only when the pumped width exceeds a certain critical value. For a too small pumped region ($1.5 \, \mu\text{m}$ for our laser structure), the waveguide loss of the tilt mode is too large; therefore such a mode cannot survive. Note also that beyond a certain width there exists no stable solution, which marks the onset of multimode operation. The time-averaged tilt angle is unlikely to further increase with multimode operation. Correspondingly, in the experiment, we observed a saturation of the far-field tilt.
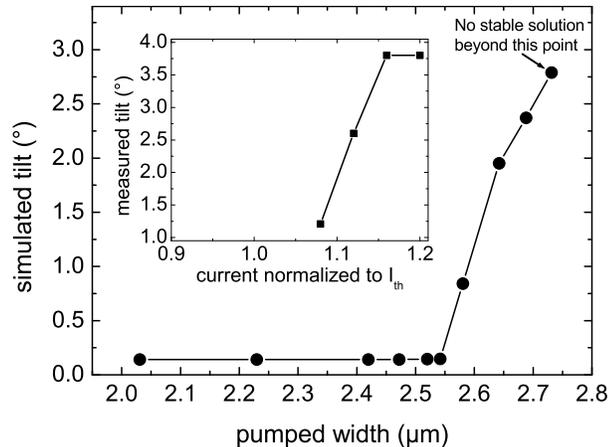
Fig. 3: Simulated far-field tilt as a function of effectively pumped width. Beyond a pumped width of about $2.5\,\mu$m, a tilt can be observed. The inset shows measured tilt values as a function of current.

Further experiments have shown that if the stripe width is much larger than the critical value, the laser starts already to oscillate in a higher order lateral mode and shows multiple mode transitions during a pulse. In agreement with literature data, we found that for single mode operation the ridge width has to be smaller than $2\,\mu$m [5, 6]

4.   Conclusion

In conclusion, we have presented time-resolved emission spectra and far-field distributions along with theoretical computations which show that local self heating of InGaN-based violet-blue diode lasers together with carrier diffusion effects can result in lateral mode switching and beam steering of the far-field on a microsecond timescale. This unwanted behavior can be avoided if the ridge width is reduced to $1.5\,\mu$m.

References

[1] W.W. Chow and H. Amano, "Analysis of Lateral-Mode Behavior in Broad-Area In-GaN Quantum-Well Lasers," *IEEE J. Quantum Electron.*, vol. 37, no. 2, pp. 265–273, 2001.

[2] V. Kümmler, G. Brüderl, S. Bader, S. Miller, A. Weimar, A. Lell, V. Härle, U.T. Schwarz, N. Gmeinwieser, and W. Wegscheider, "Degradation Analysis of InGaN Laser Diodes," *phys. stat. sol. (a)*, vol. 194, no. 2, pp. 419–422, 2002.

[3] C. Eichler, S.S. Schad, M. Seyboth, F. Habel, M. Scherer, S. Miller, A. Weimar, A. Lell, V. Härle, and D. Hofstetter, "Time resolved study of GaN-based laser diode characteristics during pulsed operation," *phys. stat. sol. (c)*, vol. 0, no. 7, pp. 2283–2286, 2003.

[4] K.J. Ebeling, *Integrierte Optoelektronik: Wellenleiter, Photonik, Halbleiter*. Springer-Verlag, second ed., 1992.

[5] S. Nakamura, M. Senoh, S. Nagahama, N. Iwasa, T. Yamada, T. Matsushita, H. Liyoku, Y. Sugimoto, and T. Kozaki, "InGaN/GaN/AlGaN-Based Laser Diodes Grown on GaN Substrates with a Fundamental Transverse Mode," *Jpn. J. Appl. Phys.*, vol. 37, no. 9A/B, pp. L1020–L1022, 1998.

[6] T. Tojyo, S. Uchida, T. Mizuno, T. Asano, M. Takeya, T. Hino, S. Kijima, S. Goto, Y. Yabuki, and M. Ikeda, "High-Power AlGaInN Laser Diodes with High Kink Level and Low Relative Intensity Noise," *Jpn. J. Appl. Phys.*, vol. 41, no. 3B, pp. 1829–1833, 2001.

Diode-Pumped Intra-Cavity Frequency-Doubled Semiconductor Disk Laser Based on GaAsSb/GaAs

Eckart Gerster and Susanne Menzel

Up to now, GaAs and InGaAs has been commonly used as quantum-well material for diode-pumped semiconductor disk lasers. Using InGaAs quantum wells, maximum emission wavelengths of 1100 nm can be achieved. With intra-cavity frequency doubling, the coverage of the blue and green spectral range was demonstrated. To extend the range to yellow and red colors, longer emission wavelengths are necessary. The material system GaAsSb/GaAs allows fundamental emission wavelengths in the 1100–1300 nm range, frequency-doubled it would be possible to cover the yellow to red wavelength range. In this article, we report on a diode-pumped intra-cavity frequency-doubled GaAsSb/GaAs disk laser which is emitting orange.

1. Introduction

For the the red and infrared spectral range, semiconductor lasers generally are known to be highly efficient, low-cost, and reliable laser sources. Up to now, the red, orange, and yellow wavelength regime is mainly covered by dye lasers and argon/krypton ion lasers. But not only dye lasers are sources for laser radiation in the range from 580 nm to 630 nm. HeNe lasers using their discrete emission lines at 594 nm and 612 nm are also available, but the power is limited to a few mW only. Elaborate diode-pumped solid-state lasers are reported to emit yellow and orange at 580 nm and 598 nm using stimulated Raman scattering (SRS) in combination with second harmonic generation (SHG) [1],[2], frequency-doubled Nd:YAG pumped LiF:F$_2^-$ lasers have been demonstrated [3], and expensive multi-stage optical parametric oscillators (OPOs) emitting in this frequency range are available [4]. Consequently, there is a large demand for replacements of these expensive, large-size, and power consuming lasers.

Semiconductor disk lasers, also referred to as VECSELs (Vertical External Cavity Surface Emitting Lasers) are known to be power scalable laser sources, that demonstrate very high beam quality [5]. This, combined with their external cavity, makes disk lasers very well suitable for intra-cavity harmonic generation (SHG) [6],[7]. To cover the visible spectrum using frequency doubling, a fundamental wave in the range of 900–1300 nm is necessary. The lower wavelength range is well covered by the semiconductor material system InGa(Al)As. For the higher wavelengths, Ga(Al)AsSb and GaInNAs are suitable systems. Based on the GaAsSb/GaAs material system, we presented an orange-emitting

intra-cavity frequency-doubled semiconductor disk laser [8]. The second harmonic generation (SHG) is done using a Lithium-Triborate crystal (LBO) as the nonlinear material. The infrared fundamental wavelength of $\lambda = 1220\,\text{nm}$ corresponds to a second harmonic wavelength of $\lambda = 610\,\text{nm}$.
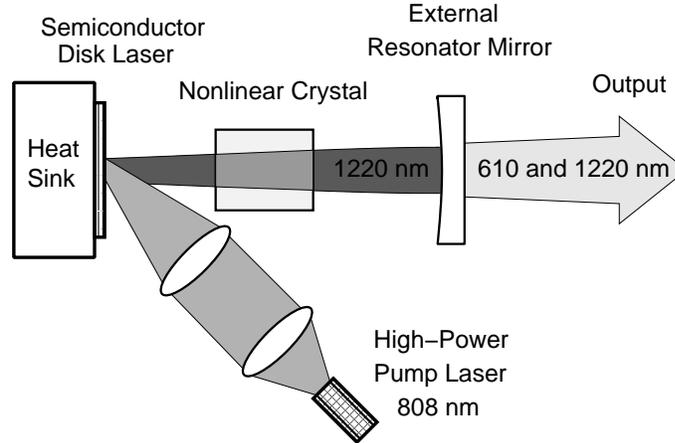
Fig. 1: Setup of a diode-pumped intra-cavity frequency-doubled semiconductor disk laser based on GaAsSb which shows orange emission at 610 nm.

As shown in Fig. 1, the semiconductor chip is mounted on a heat sink and forms a resonator together with an external concave mirror. The laser pump beam is focused onto the chip at an angle of about $45\,°$ and should ideally result in a round spot. A nonlinear optical crystal can be placed inside the external cavity for frequency doubling. The laser cavity is formed by an AlAs/GaAlAs Bragg mirror (distributed Bragg reflector, DBR) which is grown directly on the GaAs substrate and an external concave dielectric mirror. Because of the short gain medium length, the external mirror reflectivity has to be $\sim 99\,\%$. The Bragg mirror should exceed $99.9\,\%$ to avoid additional losses. A stable concentric (hemispheric) resonator configuration is used here. The length of the laser cavity is variable and is mainly given by the mirror radius.

2. Epitaxial Design

The epitaxial structure is grown by solid-source molecular beam epitaxy (MBE) on a GaAs substrate. As shown in Fig. 2, the etch stop layer is the first layer which is grown onto the substrate, followed by the window layer, the quantum wells, the absorbing layers, and completed by the AlGaAs/AlAs Bragg mirror layers. The gain is provided by six $7\,\text{nm}$-thick compressively strained $GaAs_{0.74}Sb_{0.26}$ quantum wells in the antinodes of the standing wave pattern, separated by (Al)GaAs pump light absorbing layers. Electron-hole pairs are generated by absorption of the pump light in the (Al)GaAs absorbing layers and relax into the GaAsSb quantum wells where they undergo stimulated emission. The very strong absorption coefficient of the semiconductor material yields to short absorption

lengths for the pump light of only a few microns. The absorbing layers are realized as GRaded-INdex (GRIN) areas to support carrier movement into the quantum wells. A standing wave builds up within the resonator with the intensity maxima located in the quantum-well regions. A surface barrier made of AlGaAs with an Al content of 30 % prevents excited carriers from recombining at the wafer surface. This surface barrier layer is transparent for the pump wavelength. Optical free-carrier absorption (of photons at the emission wavelength) is kept to a minimum since the epitaxial layers are not intentionally doped.
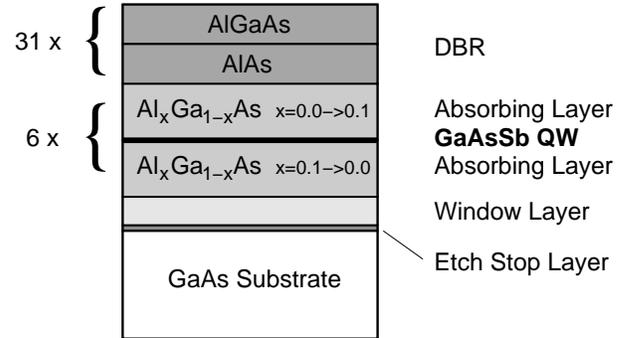
Fig. 2: Schematic layer structure of the semiconductor disk laser. The inverted layer sequence allows a complete substrate removal.

The monolithically grown Bragg mirror consists of 62 AlGaAs/AlAs layers. The Al content of the AlGaAs mirror layers was chosen to be 20 % to avoid absorption of the pump wavelength in the mirror layers. The double-band Bragg mirror is designed to reflect the laser wavelength of 1220 nm at normal incidence and additionally the 805 nm pump beam under an angle of 45 ° back into the absorbing layers to enhance the absorption rate. Thus, heat generation in the Bragg mirror is almost avoided. The calculated Bragg reflectivity is 99.96 % at 1220 nm and 95.7 % at 805 nm. Figure 3 shows both, the calculated and measured Bragg mirror reflectivity. The two curves are in good agreement, the center reflectivity is near 1220 nm and the reflectivity peaks at 805 nm in both cases. Note, that simulation and measurement in Fig. 3 was done under an angle of 10 ° but the design for the layer sequence was optimized for high reflectivity at 1220 nm under 0 ° and 805 nm under 45 °.

The AlAs etch stop layer allows the complete removal of the substrate in a wet-chemical etching process. After substrate removal, the etch stop layer is also removed in a additional etching step. The $Al_{0.3}Ga_{0.7}As$ window layer prevents excited carriers from recombining at the wafer surface and is transparent for the pump wavelength.

3. Processing and Mounting

For semiconductor disk lasers, no lateral (lithographic) patterning is necessary. The efficient extraction of unavoidable heat is an essential issue for disk lasers. Considering the significantly higher quantum defect (difference in quantum energy between pump and emission photons) compared to 980 nm devices, the heat generation for GaAsSb based
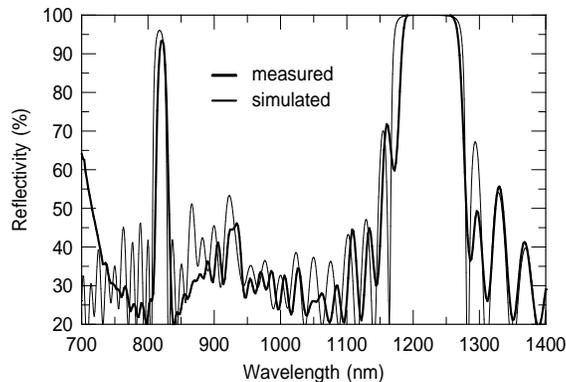
Fig. 3: Comparison of the simulated and measured reflectivity spectrum of the Al-GaAs/AlAs Bragg mirror. Note the additional reflectivity peak for the pump wavelength slightly above 800 nm.
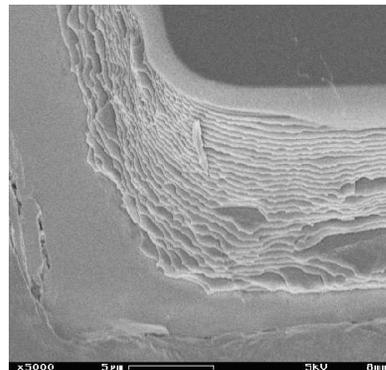
Fig. 4: SEM micrograph of the edge of a disk laser structure after complete substrate removal, showing the sophisticated layer structure at the edge of the chip and a smooth semiconductor surface.

devices is even higher. Hence, a complete substrate removal yields to a substantial reduction of the thermal resistance. This can be achieved by etching the GaAs substrate. In this case, mounting has been done before the etching and an inverted layer structure with a built-in etch stop layer has been used. The wafer surface has been metallized with a Ti/Pt/Au layer sequence. Chips with the desired size are cleaved and directly bonded to a copper heat sink using indium solder. The substrate has been selectively etched away using a H_2O_2/NH_4OH wet etch. The etching process stops at the AlAs stop layer which is removed by HF etching in a subsequent step. Figure 4 shows a SEM micrograph of the edge of a semiconductor disk laser structure after complete substrate removal. The total remaining layer thickness is about 7.5 μm. The smooth semiconductor surface can be seen in the upper right corner of the image.

4.   Experimental Results

For the laser resonator, an external dielectrically coated mirror is used, whose reflectivity is about $R = 99.9\%$ for the fundamental wavelength and the transmission is about $T = 95\%$ for the second harmonic. The radius of curvature is 75 mm. The output power was measured with calibrated InGaAs and Si photodetectors for the fundamental and second harmonic wavelengths, respectively. All the measurements shown in this article have been done in TEM$_{00}$ fundamental mode operation. For our intra-cavity frequency doubling experiments, Lithium Triborate, (LiB$_3$O$_5$, LBO) has been chosen. A 3 mm-long type-I critically phase-matched LBO crystal has been adjusted near the semiconductor chip into the laser cavity. We achieved 30 mW of orange continuous-wave laser radiation with a wavelength of 610 nm at a temperature of $-15\,^\circ$C. The transmitted fundamental power was measured to be 68 mW at the same temperature [8]. In Fig. 5, the continuous-wave output power characteristics at a temperature of $-15\,^\circ$C of the transmitted fundamental

and the second harmonic is plotted.

At room temperature, up to 12 mW of orange light has been measured. In operation, not only second harmonic emission but also undesired residual fundamental radiation is emitted. For the power measurements, suitable optical filters have been used to either block the fundamental or the second harmonic. The transmission of these filters was considered for the calibration of the power values shown in Fig. 5. The disk laser is pumped by a commercial 3 W 805 nm high-power broad-area laser diode. The diameter of the laser-active area is estimated to be 80 μm. Part of the pump power is reflected on the surface of the laser disk. For the pump power listed in the diagram in Fig. 5, only the absorbed portion was taken into account. The fundamental and second harmonic peak wavelengths are around 1220 nm and 610 nm as shown in Fig. 6. The spectral width (FWHM) of the second harmonic is measured to be about 1 nm.
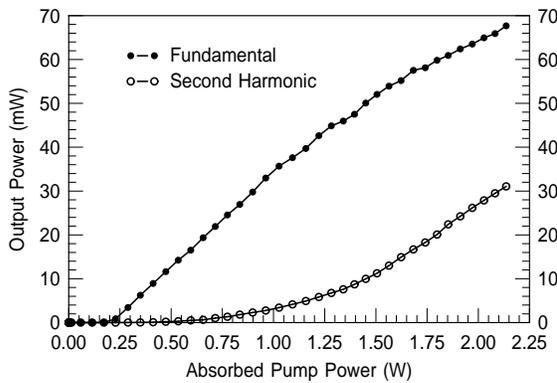
Fig. 5: Fundamental and second harmonic continuous-wave output power characteristic of a GaAsSb/GaAs semiconductor disk laser.
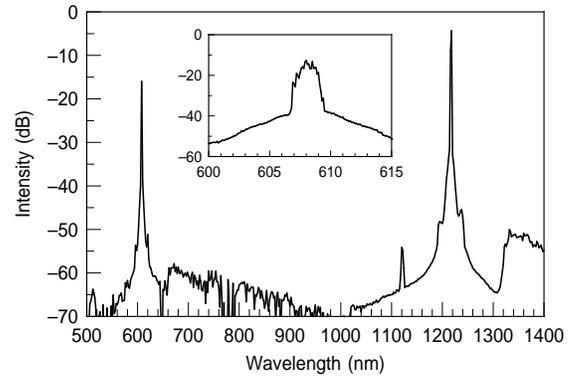
Fig. 6: Fundamental (1220 nm) and second harmonic (610 nm) output power characteristic of a frequency-doubled GaAsSb/GaAs semiconductor disk laser.

Beside of the orange emitting laser we demonstrated a yellow-orange emitting disk laser emitting 15 mW at 589 nm in the TEM_{00} mode. The corresponding fundamental wavelength is 1178 nm. Therewith, this laser system can act as source for sodium absorption spectroscopy.

For this work, a linear resonator configuration has been used. In this case, no focus is located in the external resonator. A location of a focus inside the crystal using a different resonator configuration would increase the optical power density and thus the doubling efficiency significantly. Moreover, the SHG process is not yet optimized.

5. Conclusion

An inverted GaAsSb/GaAs semiconductor disk laser has been grown, processed with complete substrate removal and characterized. The transmitted second-harmonic generated

optical power in continuous-wave operation has been measured to be 30 mW at a wavelength of 610 nm. This orange laser radiation was emitted in the fundamental transverse mode. The corresponding fundamental wavelength has been 1220 nm. Additionally, a frequency-doubled disk laser has been demonstrated emitting yellow-orange at a wavelength of 589 nm, hitting the sodium spectral lines.

To our knowledge, we have demonstrated intra-cavity second-harmonic generation (SHG) of a semiconductor disk laser in the wavelength range beyond 500 nm for the first time. Moreover, we successfully operated the first continuous-wave GaAsSb disk laser at room temperature.

References

[1] H. M. Pask and J. A. Piper, "All-solid-state yellow laser source with 1 W average power," in *Proc. Conference on Lasers and Electro Optics (CLEO) 1999*, Baltimore, MD, p. 2, May 1999.

[2] J. Simons, H. M. Pask, P. Dekker, and J. A. Piper, "Compact diode-pumped 598-nm laser source," in *Proc. Solid State Lasers XI*, San Jose, CA, pp. 57–64, January 2002.

[3] S. M. Giffin, I. T. McKinnie, and V. V. Ter-Mikirtychev, "Tunable visible solid-state lasers based on second-harmonic generation of $LiF:F_2^-$ in potassium titanyl phosphate," *Opt. Lett.*, vol. 23, no. 3, pp. 192–194, 1998.

[4] T. Petelski, R. S. Conroy, K. Bencheikh, J. Mlynek, and S. Schiller, "All-solid-state, tunable, single-frequency source of yellow light for high-resolution spectroscopy," *Opt. Lett.*, vol. 26, no. 13, pp. 1013–1015, 2001.

[5] M. Kuznetsov, F. Hakimi, R. Sprague, and A. Mooradian, "Design and characteristics of high-power (> 0.5-W CW) diode-pumped vertical-external-cavity surface-emitting semiconductor lasers with circular TEM_{00} beams," *IEEE J. Sel. Top. Quantum Electron.*, vol. 5, no. 3, pp. 561–573, 1999.

[6] T. D. Raymond, W. J. Alford, M. H. Crawford, and A. A. Allerman, "Intracavity frequency doubling of a diode-pumped external-cavity surface-emitting semiconductor laser," *Opt. Lett.*, vol. 24, no. 16, pp. 1127–1129, 1999.

[7] E. Schiehlen, M. Golling, and P. Unger, "Diode-pumped semiconductor disk laser with intra-cavity frequency doubling using lithium triborate (LBO)," *IEEE Photon. Technol. Lett.*, vol. 14, no. 6, pp. 777–779, 2002.

[8] E. Gerster, I. Ecker, S. Lorch, C. Hahn, S. Menzel, and P. Unger, "Orange-emitting frequency-doubled GaAsSb/GaAs semiconductor disk laser," *J. Appl. Phys.*, vol. 94, no. 12, pp. 7397–7401, 2003.

Absorption in InGaN-on-Sapphire Based Light-Emitting Diodes

Sven-Silvius Schad and Barbara Neubert

In this work, we investigate the absorption distribution in InGaN-on-sapphire based light-emitting diodes (LEDs). We observed by transmission measurements that most of the absorption takes place in a thin layer close to the sapphire substrate. The lateral intensity distribution in the surrounding of LED emitters is determined by the photocurrent measurement method. Based on the observations by transmission, a model for the lateral light propagation in the LED-wafer containing also a thin, strong absorbing layer is presented. It is shown that interference of the mode profiles with the absorbing layer leads to different modal absorption which explains the non-exponential intensity distribution. We are able to estimate the optical thickness of the absorbing layer to be 75 nm. Furthermore, this layer may be one of the major loss mechanism in InGaN-LEDs grown on sapphire substrate due to the large absorption coefficient which is effective at the emission wavelength.

1. Introduction

The high performance of state of the art light-emitting diodes opened a variety of new lighting applications. Besides the AlGaInP-material system, the group III-nitrides gained a lot of attraction. The large output power and the short emission wavelength made it possible to pump luminescence converters to generate white light. The efficiency of today's white LED devices can reach up to 30 lm/W [1] and is superior to conventional incandescent lamps ($\approx$ 7 lm/W) but still less than fluorescent lamps ($\approx$ 36 lm/W). Besides improvement of epitaxial methods and device processing, the problem of light extraction attracts more and more attention. It is well known, that the presence of absorption can significantly alter the external quantum efficiency. Therefore, we want to give a profound insight into the absorption distribution which is important to understand the light extraction in InGaN-on-sapphire based LED devices. Moreover, we will point out that the initially grown GaN exhibits significant absorption losses. This means in particular that the suppression of lateral guided modes and the resulting reduction of absorption losses might play a key role for the efficiency improvement.

1.1 Photocurrent Measurement Method

To determine the absorption in LED structures, we the photocurrent measurement method (PMM) which is an integrated optical experiment [2]. In contrast to other common mea-

surement methods, the sample itself is used for excitation and detection. A set of waveguides with different lengths each having a separate emitter and detector is fabricated from the investigated LED wafer by means of lithography, mesa etching and metal evaporation.

The emitter and detector are of same mesa size ($20 \times 100 \, \mu m^2$) and exhibit a fully covered p-metallization on top (see Fig. 1). An n-type contact beneath the mesa is used to access the p–n-junction. In between one emitter and the respective detector, a waveguide is formed in the same mesa etching process ($100 \, \mu m$ width) which is electrically and optically separated from both the emitter and detector mesa by a small trench. A second larger mesa going down to the substrate and including all three elements (again $100 \, \mu m$ width) is then dry-etched. This enables a true semiconductor-air interface over the whole thickness of the epitaxial stack. A set of such cells with different waveguide lengths (length 200–$3000 \, \mu m$) is fabricated and used for the determination of the intensity decay.

At each cell, the photocurrent is measured while the emitter is driven at constant current which is the same for all cells. The photocurrent vs. length shows the intensity decay found in the surrounding of an emission center in LEDs. At first guess, this dependence should be exponential; however, it is found not to be. Therefore, we tried to model this behavior by taking scattering at the large amount of dislocations present in the buffer layer into account. Using ray-trace-simulations [2] we could describe the intensity behavior. In this work, we will give a new, different interpretation of this behavior which agrees with other independent measurement techniques like the transmission measurement.

First, we investigated the spectral dependence of the intensity decay. A series of LED wafers was grown by MOVPE which exhibit different emission wavelengths. The layer structure is reported in [3]. The different emission wavelength of the samples S1 ($\lambda = 404 \, nm$), S2 ($\lambda = 431 \, nm$), and S3 ($\lambda = 433 \, nm$) was achieved by adjusting the growth time of the quantum wells. Conventional LEDs made out of the wafer material exhibit output powers larger than $1 \, mW$ at a current of $20 \, mA$ for on-wafer-measurements using
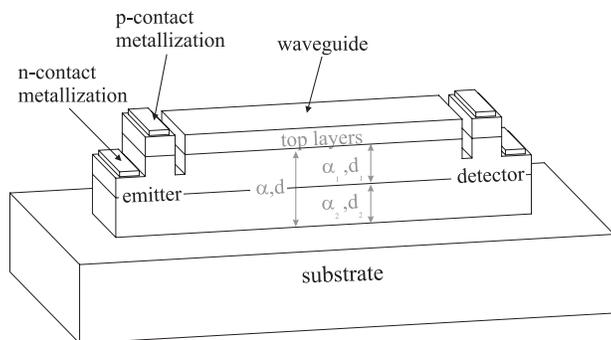
Fig. 1: Arrangement of emitting LED, waveguide and detector LED used for PMM.
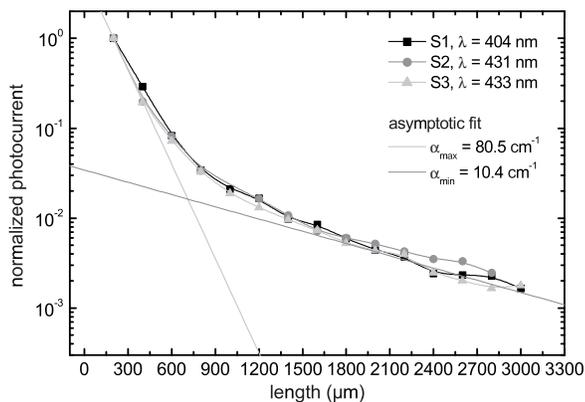
Fig. 2: Dependence of the intensity distribution on the emission wavelength.

thickness (nm)	material	n	α
250	p-GaN:Mg	2.5410	
20	Al$_{0.3}$Ga$_{0.7}$N:Mg	2.3847	
5	GaN	2.5410	0
5x { 4	InGaN	2.5410	
5	GaN	2.5410	
$d=1500$ { d_1	n-GaN:Si	2.5410	α_1
d_2	absorbing GaN	2.5410	α_2
300000	sapphire	1.7866	0
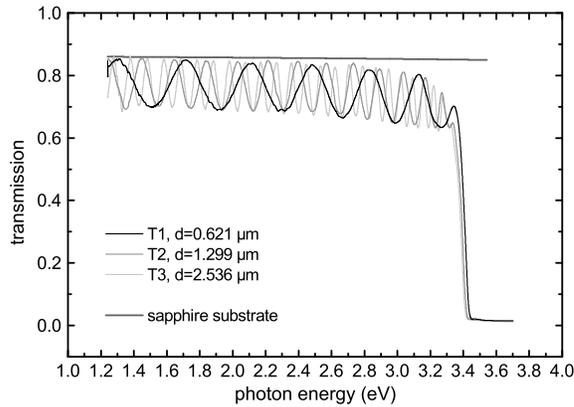
Fig. 3: Transmission curves for GaN on double side polished sapphire. As can be seen, the thickness does not influence the envelopes and a significant difference in the region 2–3 eV to the sapphire transmission is observable.

Fig. 4: Layer structure used for the calculation of modal absorption coefficients if a bottom layer absorption is assumed (see Fig.1). d_2 denotes the thickness of the absorbing layer and $d_1 + d_2 = 1500$ nm.

an integrating sphere. A part of these LED wafers has been processed for the PMM and evaluated. We obtained the intensity distribution which is depicted in Fig. 2. No significant wavelength dependence of the lateral intensity decay can be observed. Further optical investigations have been carried out, which we presented in [3]. It can be shown that a significant de-tuning of the absorption edge and the emission edge of the emitting LED structures exists due to the Quantum Confined Stark effect. The shift is larger than the spectral width of the spontaneous emission and thus, the absorbance of the wells does not influence the intensity distribution. Thus, only the GaN absorption properties are measurable by the PMM.

Our previous investigations [2] about the lateral intensity distribution was based on a ray-trace model which also included scattering . If this model is applied, an absorption coefficient of $\alpha = 7\,\mathrm{cm}^{-1}$ can be determined. This value is low compared to literature data. Brunner et al. [4] report a value of $\alpha = 200\,\mathrm{cm}^{-1}$ at 400 nm for GaN using photothermal deflection spectroscopy (PDS). On the other hand, the modal absorption found in InGaN laser diodes is in the range of 37–54 cm^{-1} and much lower [6, 7]. Therefore, further absorption investigations have been carried out.

Another series of samples was grown on double side polished sapphire consisting only of a single GaN-buffer-layer, each sample with different film thickness. The samples were grown in the same manner as the buffer layer of our LED wafers. Then, a transmission measurement was carried out which is depicted in Fig. 3. The observed modulation in the transmission is due to the Fabry-Pérot-modes of the GaN-layer. If no absorption in the layer was present, the envelope of the maxima would be identical to the transmission curve of sapphire [8]. The decrease is obviously due to the absorption present in the layers. However, the envelope of the transmission maxima is the same for all the samples T1,T2,

and T3 despite the significantly different film thicknesses. If the GaN-layer absorption contributed to the transmission, the envelope transmission would decrease with increasing film thickness. This is obviously not the case. Thus, it is concluded that the absorption of the last grown, uppermost GaN is low. This behavior is also measurable by photothermal deflection studies [3]. Therefore, we explain the absorbance behavior by a thin, highly absorbing GaN-layer and a thick, weakly absorbing GaN-layer. If the thickness of the thin absorbing layer is lower than the thickness of sample T1, then the transmission gets independent of the total sample thickness. Moreover, it is possible to explain the reduced transmission of the samples compared to sapphire (Fig. 3) by a large band tail caused by the high dislocation density and grain boundaries of the initially grown GaN. The low absorption of the top layer would then be due to the improved material quality which exhibits no significant band tail.

For further evaluation, the thickness of the three samples has been determined by the interference fringes of the transmission spectra. T1,T2, and T3 exhibit $0.621\,\mu m$, $1.299\,\mu m$, and $2.536\,\mu m$ layer thickness. We numerically analyzed the transmission of a three layer stack for our proposed absorption distribution consisting of a sapphire substrate, an absorbing bottom layer, and a weakly absorbing GaN-layer. The model takes all interference effects into account including the influence of the substrate. Since the mode spacing of the substrate Fabry-Pérot-modes is narrow, a spectral averaging over one interference period of the substrate was carried out. The simulated transmission curves were adjusted to the experimental data of the samples using the layer thickness and the absorption as fitting parameters. For the fit, we used the spectral dependence found by PDS [3]. We assumed that the complete band-tail absorbance takes place in the absorbing layer. For the weakly absorbing GaN-layer, a constant absorption has been chosen. With the simulated transmission curves, we achieved nearly a perfect fit to the transmission measurement. Since no thickness dependence was observed in the transmission data, it is possible to determine the amount of absorbed light only, but no absorption coefficient. Therefore, only the product αd is really meaningful. In the next section, we predict limits for the bottom layer thickness by PMM which then enables a determination of the absorption distribution and its absorption coefficients.

1.2   Model for light propagation in the Photocurrent Measurement Method

Based on these results, the light propagation in the PMM is reviewed. We focus on the effect of the absorbing bottom layer on the mode propagation. In contrast to our earlier model, we assume that no scattering is present in our structure.

Since the photocurrent of the detector LED is proportional to the intensity, one has to consider all contributions to the intensity at the detector to obtain the photocurrent in dependence of the waveguide length. This can be quite complicated since the light propagates through a multi-mode waveguide and the modes exhibit different absorption properties as we show below. It is assumed that each mode propagates separately within

the waveguide and contributes independently from the others to the photocurrent. We solved the Helmholtz-Equation

$$\Delta E_y + k_0^2 E_y = 0 \tag{1}$$

with the transfer-matrix method, using

$$E_y = \left(E_y^{(+)} \mathrm{e}^{ik_z z} + E_y^{(-)} \mathrm{e}^{-ik_z z} \right) \mathrm{e}^{ik_x x} \qquad . \tag{2}$$

for each layer as trial solution and applied the boundary conditions. This leads to a characteristic equation from which the eigenvalues of the layer structure are calculated and the effective indices $n_{\mathrm{eff}} = k_x/k_0$ are obtained. The imaginary part of the effective index contains the extinction from which the modal absorption is calculated. To gain insight into the light propagation, we studied two models for the LED: a homogenous absorption distribution and a layer structure where the buffer is divided into a non-absorbing and a highly absorbing region according to our proposition. For both models, literature data [9] are taken for the refractive index at an emission wavelength of 400 nm. The homogeneous absorption distribution is discussed in detail in [3]. For the proposed inhomogeneous absorption distribution, the mode profile interferes with the absorbing layer and causes that the modal absorption coefficients are sinusoidal modulated versus the effective index. For the uppermost effective indices, the mode profile does not penetrate into the absorbing layer. Thus, a few modes exist which exhibit a quite low absorption [3]. These modes are just the modes which are required to describe the lateral intensity distribution. For a detailed analysis, we consider next which modal absorption coefficients are necessary to describe the intensity decay of the PMM. Therefore, we determined the slopes of the tangents to the intensity decay presented in Fig. 2 to limit the number of modes. Modes with a large modal absorption have already decayed in the observed range. Therefore, only modes which lie in between $\alpha_{\mathrm{min}} = 10.5\,\mathrm{cm}^{-1}$ and $\alpha_{\mathrm{max}} = 80.5\,\mathrm{cm}^{-1}$ are of considerable interest. As already mentioned, only the αd product can be determined from the transmission measurement. Thus, it is possible to distribute the absorption into the bottom layer d_1 and the remaining GaN-layer d_2 according to

$$\alpha d = \alpha_1 d_1 + \alpha_2 d_2 \qquad . \tag{3}$$

Besides the thickness degree of freedom, the relative composition of absorption can be changed. We used

$$\alpha_2 d_2 = p \cdot \alpha d \tag{4}$$

with $0 \leq p \leq 1$ to calculate the absorption coefficients α_1 and α_2. p denotes the relative absorbed power for normal incidence on the sample which is the fraction of power absorbed in the bottom layer for the transmission and the PDS measurement. For the intensity decay of PMM, the thickness of d_1 and d_2 are also important due to the interference of the modal field profile with the two layers. Both parameters, p and d_1 of the buffer layer have been varied for an αd-product of 0.030 which was determined from the previous transmission measurement. Before we present the fit of the lateral intensity decay, we shortly discuss the dependencies of the introduced parameters on the modal absorption.
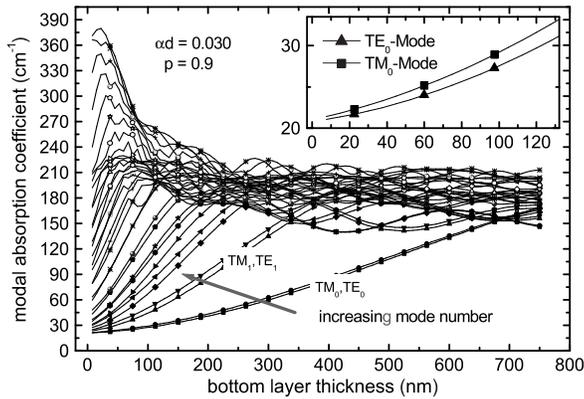
Fig. 5: Modal absorption coefficients vs. bottom layer thickness for $\alpha d = 0.030$, $p = 0.9$ and the layer structure of Tab. 4. As can bee seen, the modal absorption spreads with decreasing bottom layer thickness (Inset depicts magnified curves with same units).
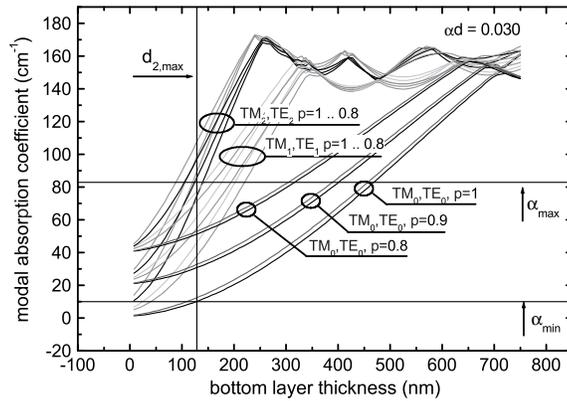
Fig. 6: Influence of the fraction of absorbed power p in the bottom layer on the first three TE and TM-modes for the structure of Tab. 4. Limits for the absorption coefficients are taken from Fig. 2. From α_{min}, the maximal thickness of the absorbing layer $d_{2,max}$ can be estimated to be 130 nm.

In Fig. 5 the modal absorption coefficients for all modes are shown for an absorbance distribution factor of $p = 0.9$ versus the buffer thickness. To get low absorption coefficients of about α_{min}, it is necessary to have a thin absorbing bottom layer. The dependence of p is shown in Fig. 6 where the number of depicted modes was limited to six. As can be seen, the modal absorption coefficient drops below α_{min} for a thickness of $d_{2,max} = 130$ nm. This can be regarded as the maximum layer thickness since α_{min} has been the minimal observed absorption of the lateral intensity decay. To obtain a better estimation of the absorbing layer thickness, a fit of the PMM intensity distribution is desirable. The excitation of the lateral modes should be proportional to the confinement factor of the mode. However, the gap between the exciting LED structure and the waveguide as well as the scattering at dislocations and grain boundaries can significantly modify the relative mode contribution to the overall intensity distribution. Therefore, we used the modal excitation b_i as fitting parameters for the intensity distribution function

$$I = I_0 \sum b_i e^{-\alpha_i x} \tag{5}$$

where the α_i are the modal absorption coefficients for both TE and TM modes and x denotes the propagation distance. The large amount of modes (16 TE and 15 TM) suggests that there are more degrees of freedom for the fit than in the measurement data. However, as already mentioned, the large modal spreading with decreasing thickness causes that most of the modes exhibit such a large attenuation that they are not observable in the investigated range. Thus, only the first eight TE and TM modes really contribute to the intensity distribution. Both parameters, p and d_2 where varied; and (5) was fitted to the
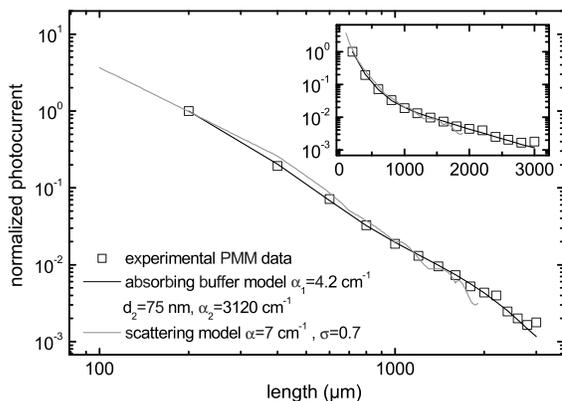
Fig. 7: Comparison between PMM measurement data and both, the absorbing buffer model and the scattering model [2]. The absorbing buffer model fits better to the observed intensity decay. The inset depicts the same data but on linear scale for the length as in Fig. 2.

experimental data using the Levenberg-Marquardt algorithm. As can be seen in Fig. 7, a perfect agreement even in logarithmic scale across three orders of magnitude has been achieved. Additionally, the intensity curve of the previous scattering model is shown. As can be seen, the absorbing buffer model gives a much better fit to the observed intensity distribution than the previous scattering model, especially at longer distances. From the fit, we obtained $d_2 = 75\,\text{nm}$ and $p = 0.98$. Using (3) and (4), the bottom layer absorption $\alpha_2 = 3920\,\text{cm}^{-1}$ and the weak layer absorption $\alpha_1 = 4.2\,\text{cm}^{-1}$ can be calculated.

The most important result of this analysis, however, is the small thickness of the absorbing bottom layer. This can only be attributed to the poor quality GaN, probably the nucleation layer and a part of the buffer layer. Due to the large amount of absorption, this layer may be one of the major optical loss mechanisms which is effective at the emission wavelength of InGaN-LEDs grown on sapphire.

2.   Conclusion

In this work, we investigated the lateral intensity distribution by an integrated optical waveguide experiment. By using transmission measurements and photothermal deflection spectroscopy, we showed that the complete absorption measured in the vertical direction takes place in a thin layer close to the substrate interface. We presented a new model for the lateral intensity distribution based on this bottom layer absorption and could successfully show that the observed intensity decay can be explained by modes which exhibit different modal absorption caused by interference with this absorbing layer. Based on this model, detailed parameters such as thickness and absorption coefficient of the absorbing layer could be determined. Furthermore, if the thickness of 75 nm of the absorbing layer is compared with the growth recipe of the GaN layer, we conclude that the initially grown, poor quality GaN is the origin of most of the absorption measured by PDS and transmission. This is remarkable because this layer may be one of the major optical loss mechanisms which is effective at the emission wavelength of today's InGaN-LEDs grown on sapphire besides the contact absorption.

References

[1] D. Steigerwald, J. Bhat, D. Collins, R. Fletcher, M. Holcomb, M. Ludowise, P. Martin, and S. Rudaz, "Illumination With Solid State Lighting Technology," *IEEE J. Select. Topics Quantum Electron.* **8**(2), pp. 310–320, 2002.

[2] S. Schad, B. Neubert, M. Seyboth, F. Habel, C. Eichler, M. Scherer, P. Unger, W. Schmid, C. Karnutsch, and K. Streubel, "Absorption of guided modes in light emitting diodes," *Proc. SPIE* **4996**, pp. 10–17, 2003.

[3] S. Schad, B. Neubert, J. Brüning, C. Eichler, F. Habel, F. Scholz, P. Unger, and D. Hofstetter "Absorption in InGaN-on-sapphire LED-structures: Comparison between Photocurrent Measurement Method (PMM) and Photothermal Defelection Spectroscopy (PDS)," submitted to *Proc SPIE*, 2004.

[4] D. Brunner, H. Angerer, E. Bustarret, F. Freudenberg, R. Höpler, R. Dimitrov, O. Ambacher, and M. Stutzmann, "Optical constants of epitaxial AlGaN films and their temperature dependence," *J. Appl. Phys.* **82**(10), pp. 5090–5096, 1997.

[5] G. Yu, G. Wang, H. Ishikawa, M. Umeno, T. Soga, T. Egawa, J. Watanabe, and T. Jimbo, "Optical properties of wurtzite structure GaN on sapphire around the fundamental absorption edge (0.78-4.77) eV by spectroscopic ellipsometry and the optical transmission method," *Appl. Phys. Lett.* **70**(24), pp. 3209–3211, 1997.

[6] S. Nakamura, M. Senoh, S. Nagahma, N. Iwasa, T. Yamada, T. Matsushita, Y. Sugimoto, and H. Kiyoku, "Optical gain and carrier lifetime of InGaN multi-quantum well structure laser diodes," *Appl. Phys. Lett.* **69**(11), pp. 1568–1570, 1996.

[7] A. Abare, M. Mack, M. Hansen, J. Speck, L. Coldren, S. DenBaars, G. Meyer, S. Lehew, and G. Cooper, "Measurement of gain current relations for InGaN multiple quantum wells," *Appl. Phys. Lett.* **73**(26), pp. 3887–3889, 1998.

[8] R. Swanepoel, "Determination of the thickness and optical constants of amorphous silicon," *J. Phys. E: Sci. Instrum.* **16**, pp. 1214–1222, 1983.

[9] G. Laws, E. Larkins, I. Harrison, C. Molloy, and D. Somerford, "Improved refractive index formulas for the AlGaN and InGaN alloys," *J. Appl. Phys.* **89**(2), pp. 1108–1115, 2001.

Ph.D. Theses

1. Safwat William Zaki Mahmoud,
   Static and Dynamic Transverse Mode Characteristics of Vertical-Cavity Surface-Emitting Semiconductor Lasers,
   10.06.2002.

2. Thomas Knödl,
   Mehrstufige Halbleiterlaserdioden mit Vertikalresonator,
   17.03.2003.

3. Franz Eberhard,
   InGaAs/AlGaAs-Laserdioden mit trockengeätzten Resonatorspiegeln,
   16.05.2003.

4. Eckard Deichsel,
   Design, Herstellung und Charakterisierung von kantenemittierenden Hochleistungs-Laserdioden mit verbesserten Strahleigenschaften,
   04.07.2003.

5. Heiko Unold,
   Mode Control in Vertical-Cavity Surface-Emitting Laser Diodes,
   26.11.2003.

6. Veit Schwegler,
   Herstellung und Charakterisierung von lichtemittierenden Dioden im AlGaInN-Materialsystem,
   03.12.2003.

7. Felix Mederer,
   Optische Datenübertragung mit Vertikallaserdioden im Wellenlängenbereich von 650 bis 1550 nm,
   15.12.2003.

Diploma and Master Theses

1. Serge Eric Thiam Nkuiguieng,
   Herstellung und Charakterisierung von optischen Beschichtungen für Laserfacetten hergestellt mittels Ionenstrahlsputterdeposition.
   Diploma Thesis, Optoelectronics Department, January 2003.

2. Lothar Schlafer,
   Intra-Entangled Quantum Solitons in Quantum Information Processing,
   Diploma Thesis, Department of Quantum Physics, May 2003.

3. Philipp Gerlach,
   Charakterisierung von integrierten Laser-Modulator-Bauelementen für die hochbit-ratige optische Datenübertragung,
   Diploma Thesis, Optoelectronics Department, July 2003.

4. Cristina Goya Herrera,
   Thermal and Dynamic Characterization of 2-D Vertical Cavity Laser Diode Arrays,
   Master Thesis at the Universidad de Cantabria, Spain an the Optoelectronics Department, July 2003.

5. Peter Engelhart,
   Halbleiter-Laserverstärker mit trapezförmiger Gewinnzone,
   Diploma Thesis, Optoelectronics Department, August 2003.

6. Christian Hahn,
   Optisch gepumpter GaAsSb/GaAs Halbleiter-Scheibenlaser,
   Diploma Thesis at the Fachhochschule Aalen and the Optoelectronics Department, September 2003.

7. Christoph Neureuther,
   Entwicklung eines Schnelltests für die elektro-optische Charakterisierung von GaN basierenden LEDs auf Saphir-Substraten,
   Master Thesis, Osram Opto Semiconductors, September 2003.

8. Andrea Kroner,
   Investigation of Polarization Switches in VCSELs and Methods to Avoid Them,
   Diploma Thesis, Optoelectronics Department, November 2003.

9. Jens Brüning,
   Absorption in LED-Strukturen auf Indium-Gallium-Nitrid- und Aluminium-Gallium-Indium-Phosphid-Basis,
   Master Thesis, Optoelectronics Department, December 2003.

Semester Projects

1. Peter Engelhart,
   Wellenleitergeometrie und Strahleigenschaften von Laserdioden,
   January 2003

2. Christoph Neureuther,
   Erstellung und Einführung eines Messaufbaus zur Erfassung von Single-Mode und Multi-Mode VCSEL-Dioden in beiden Polarisationsrichtungen,
   Osram Opto Semiconductors, February 2003

3. Jens Christian Brüning,
   Aufbau eines Messplatzes zur Absorptionsmessung an LED-Strukturen mittels der photothermischen Deflektionsspektroskopie,
   May 2003

4. Christof Jalics,
   Herstellung von VCSELn mit dielektrischem Oberflächengitter,
   July 2003

5. Wolfgang Schwarz,
   Aufbau, Inbetriebnahme und Charakterisierung einer Multiplexeranordnung zur Erzeugung elektrischer 40 Gbit/s-Signale,
   September 2003

Talks

[1] E. Deichsel and P. Unger, "Curved mirror and tapered devices," *High-Power Laser Workshop*, Würzburg, Germany, Jan. 2003.

[2] E. Deichsel, "High-power laser diodes," *Seminar at the Laboratory of Nanostructures, EPFL*, Lausanne, Switzerland, May 2003.

[3] E. Deichsel and P. Unger, "Design, fabrication and characterization of high-power laser diodes," *Tutorial at BACHOTEK 2003*, Brodnica, Poland, May 2003.

[4] C. Eichler, D. Hofstetter, W.W. Chow, F. Scholz, S. Miller, A. Weimar, A. Lell, and V. Härle, "Zeitaufgelöste Untersuchungen an Nitrid-Laserdioden," Lehrstuhlseminar *Optik, Spektroskopie und Laserphysik*, University of Regensburg, Regensburg, Germany, Oct. 2003.

[5] R. Michalzik, "New high-speed laser diode trends" (in German), *Optical Communications* Forum, Photonics BW Association, Stuttgart, Germany, Nov. 2003.

[6] R. Michalzik, "Vertical-cavity surface-emitting laser diodes — current research and development" (in German), Working Group *Optical Metrology* within the Photonics BW Association, Ulm, Germany, July 2003.

[7] R. Michalzik, "VCSELs — research activities and state-of-the-art" (in German), Working Group *Optical Communications* within the Photonics BW Association, Stuttgart, Germany, May 2003.

[8] R. Michalzik, "Optical backplane interconnections," Sandia National Laboratories, Albuquerque, NM, USA, May 2003.

[9] R. Michalzik, "Optical interconnects: ready for intra-box applications?", University of New Mexico, Center of High Technology Materials, CHTM, Albuquerque, NM, USA, May 2003.

[10] J.M. Ostermann, P. Debernardi, C. Jalics, A. Kroner, M.C. Riedl, R. Michalzik, and G. Bava, "Polarization control of VCSELs with a dielectric surface grating," *European Semiconductor Laser Workshop*, Torino, Italy, Sep. 2003.

[11] J.M. Ostermann, P. Debernardi, C. Jalics, A. Kroner, M.C. Riedl, R. Michalzik, and G. Bava, "Polarization control of VCSELs," *EC COST 288 Meeting*, Torino, Italy, Sep. 2003.

[12] E. Schiehlen, "Diodengepumpte Halbleiter-Scheibenlaser (VECSEL)," Toptica Photonics AG, Munich, Germany, Feb. 2003.

[13] P. Unger, "Optisch gepumpte Halbleiter-Scheibenlaser," *Seminar at the Walter-Schottky-Institute of the Technical University of Munich*, Munich, Germany, Jan. 2003.

[14] P. Unger, "Halbleiterlaser und optoelektronische Systeme," Seminar *"Technische Physik"* der Universität Kassel, Kassel, Germany, July 2003.

[15] P. Unger, "Technology of high-power lasers," *5th Int.'l Workshop on MBE and VPE Growth Physics and Technology, European Materials Research Society Fall Meeting (E-MRS 2003)*, Warsaw, Poland, Sep. 2003.

Publications and Conference Contributions

[1] E. Deichsel and P. Unger, "High-power laser diodes with improved beam quality," in Proc. *WOCSDICE 2003*, Fürigen, Switzerland, pp. 71–72, May 2003.

[2] C. Eichler, S.S. Schad, D. Hofstetter, W.W. Chow, S. Miller, A. Weimar, A. Lell, and V. Härle, "Microsecond timescale lateral mode dynamics in a narrow stripe InGaN-laser," in Proc. *Conf. on Lasers and Electro Optics, CLEO 2003*, Baltimore, MA, USA, paper CMQ5, 2003.

[3] C. Eichler, S.S. Schad, M. Seyboth, F. Habel, M. Scherer, S. Miller, A. Weimar, A. Lell, V. Härle, and D. Hofstetter, "Time resolved study of GaN-based laser diode characteristics during pulsed operation," *5th Int.'l Conf. on Nitride Semiconductors, ICNS 5*, Nara, Japan, *Phys. Stat. Sol. (C)*, vol. 7, pp. 2283–2286, 2003.

[4] E. Gerster, C. Hahn, S. Lorch, S. Menzel, and P. Unger, "Frequency-doubled GaAsSb/GaAs semiconductor disk laser emitting at 589 nm," in Proc. *IEEE Lasers and Electro-Opt. Soc. Ann. Meet., LEOS 2003*, Tucson, AZ, USA, vol. 2, pp. 981–982, Oct. 2003.

[5] E. Gerster, I. Ecker, S. Lorch, C. Hahn, S. Menzel, and P. Unger, "Orange-emitting frequency-doubled GaAsSb/GaAs semiconductor disk laser," *J. Appl. Phys.*, vol. 94, pp. 7397–7401, 2003.

[6] D. Hofstetter, S.S. Schad, H. Wu, W.J. Schaff, and L.F. Eastman, "GaN/AlN-based quantum-well infrared photodetector for $1.55\,\mu$m," *Appl. Phys. Lett.*, vol. 83, pp. 572–574, 2003.

[7] T. Knödl, M. Golling, A. Straub, R. Jäger, R. Michalzik, and K.J. Ebeling, "Multistage bipolar cascade vertical-cavity surface-emitting lasers: theory and experiment," *IEEE J. Select. Top. Quantum Electron.*, vol. 9, pp. 1406–1414, 2003.

[8] R. Michalzik, H. Roscher, M. Stach, D. Wiedenmann, M. Miller, J. Broeng, A. Petersson, N.A. Mortensen, H.R. Simonsen, and E. Kube, "Recent progress in short-wavelength VCSEL-based optical interconnections" (invited), in *Semiconductor Optoelectronic Devices for Lightwave Communication*, J. Piprek (Ed.), Proc. SPIE 5248, pp. 117–126, 2003.

[9] R. Michalzik, "Optical data links over polymeric backplanes" (invited), in Proc. *14th Annual IEEE/LEOS Workshop on Interconnections within High-Speed Digital Systems*, paper MA2. Santa Fe, NM, USA, May 2003.

[10] R. Michalzik and K.J. Ebeling, "Operating Principles of VCSELs," Chap. 3 in *Vertical-Cavity Surface-Emitting Laser Devices*, H. Li and K. Iga (Eds.), pp. 53–98. Berlin: Springer-Verlag, 2003.

[11] J.M. Ostermann, C. Jalics, A. Kroner, M.C. Riedl, R. Michalzik, and P. Debernardi, "Polarization control of VCSELs by means of a monolithically integrated surface grating" (in German: "Polarisationskontrolle von VCSELn mit Hilfe eines monolithisch integrierten Oberflächengitters"), *Photonik*, vol. 35, pp. 42–44, 2003.

[12] H. Roscher and R. Michalzik, "Low thermal resistance flip-chip bonding of 850 nm 2-D VCSEL arrays capable of 10 Gbit/s/ch operation," in Proc. *IEEE Lasers and Electro-Opt. Soc. Ann. Meet., LEOS 2003*, Tucson, AZ, USA, vol. 2, pp. 511–512, Oct. 2003.

[13] H. Roscher and R. Michalzik, "Flip-chip integration of 850 nm 2-D VCSEL arrays," in Proc. *Semiconductor and Integrated Optoelectronics Conf., SIOE 2003*, Cardiff, Wales, UK, paper 26, Apr. 2003.

[14] S.S. Schad, B. Neubert, M. Seyboth, F. Habel, C. Eichler, M. Scherer, P. Unger, W. Schmid, C. Karnutsch, and K.P. Streubel, "Absorption of guided modes in light emitting diodes," in *Light-Emitting Diodes: Research, Manufacturing, and Applications VII*, E.F. Schubert, H.W. Yao, K.J. Linden, and D.J. MacGraw (Eds.), Proc. SPIE 4996, pp. 10–17, 2003.

[15] E. Schiehlen, F. Antritter, and P. Unger, "Diode-pumped semiconductor disk laser," in Proc. *Conf. on Optoelectronic and Microelectronic Materials and Devices, COMMAD 2002*, Sydney, Australia, pp. 29–30, 2003.

[16] M. Stach, J. Broeng, A. Petersson, N.A. Mortensen, H.R. Simonsen, and R. Michalzik, "10 Gbit/s 850 nm VCSEL based data transmission over 100 m-long multimode photonic crystal fibers," in Proc. *29th Europ. Conf. on Optical Communication, ECOC 2003*, Rimini, Italy, vol. 4, pp. 1024–1025, Sep. 2003.

[17] P. Unger, "High-power laser diodes and laser diode arrays," in *Handbook of Lasers*, Part B, Chapter 2.4, IOP Publishing, 2003.

[18] C. Angelos, S. Hinckley, R. Michalzik, and V. Voignier, "Simulation of current spreading in high-power bottom-emitting vertical cavity surface emitting lasers," in *Photonics: Design, Technology, and Packaging*, C. Jagadish, K.D. Choquette, B.J.Eggleton, B.D. Nener, and K.A. Nugent (Eds.), Proc. SPIE 5277, pp. 261–272, 2003.

[19] M. Camarena, G. Verschaffelt, M.-C. Moreno, L. Desmet, H.J. Unold, R. Michalzik, H. Thienpont, J. Danckaert, I. Veretennicoff, and K. Panajotov, "Polarization behavior and mode structure of elliptical surface relief VCSELs," in Proc. *Conf. on Lasers and Electro Optics Europe, CLEO-Europe 2003*, Munich, Germany, June 2003.

[20] P. Debernardi, H.J. Unold, J. Maehnß, R. Michalzik, G.P. Bava, and K.J. Ebeling, "Single mode, single polarization VCSELs via elliptical surface etching: experiments and theory," *IEEE J. Selected Topics Quantum Electron.*, vol. 9, pp. 1394–1405, 2003, in press.

[21] M. Grabherr, S. Intemann, R. Jäger, R. King, R. Michalzik, H. Roscher, and D. Wiedenmann, "Comparison of approaches to 850 nm 2-D VCSEL arrays," in *Vertical-Cavity Surface-Emitting Lasers VII*, C. Lei and S.P. Kilcoyne (Eds.), Proc. SPIE 4994, pp. 83–91, 2003.

[22] F. Gruson, T. Zhang, H. Schumacher, M. Kicherer, R. Michalzik, and K.J. Ebeling, "Equivalent circuit modeling of GaAs/AlGaAs VCSELs and its application to the design of a SiGe laser driver," in Proc. *WOCSDICE 2003*, Fürigen, Switzerland, pp. 53–54, May 2003.

[23] R. Häring and E. Gerster, "Semiconductor laser system fills yellow-orange gap," *Europhotonics*, vol. 8, pp. 38–39, 2003.

[24] P. Ivanov, H.J. Unold, R. Michalzik, J. Maehnss, K.J. Ebeling, and I.A. Sukhoivanov, "Theoretical study of cold-cavity single-mode conditions in vertical-cavity surface-emitting lasers with incorporated two-dimensional photonic crystals," *J. Opt. Soc. Am. B*, vol. 20, pp. 2442–2447, 2003.

[25] P. Ivanov, I.A. Sukhoivanov, and R. Michalzik, "Determination of cold-cavity single-mode conditions in photonic crystal surface-emitting lasers," in Proc. *5th Int.'l Conf. on Transparent Optical Networks, ICTON 2003*, Warsaw, Poland, vol. 1, pp. 216–219, July 2003.

[26] S.W.Z. Mahmoud, M.F. Ahmed, and R. Michalzik, "Influence of optical feedback-induced phase on turn-on dynamics of vertical-cavity surface-emitting semiconductor lasers," in Proc. *46th IEEE Midwest Symposium On Circuits and Systems, MWSCAS 2003*, Cairo, Egypt, Dec. 2003, in press.

[27] N.A. Mortensen, M. Stach, J. Broeng, A. Petersson, H.R. Simonsen, and R. Michalzik, "Multi-mode photonic crystal fibers for VCSEL based data transmission," *Opt. Express*, vol. 11, pp. 1953–1959, 2003, http://www.opticsexpress.org/abstract.cfm?URI=OPEX-11-17-1953.

[28] K. Panajotov, M. Camarena, M.-C. Moreno, H.J. Unold, R. Michalzik, H. Thienpont, J. Danckaert, I. Veretennicoff, and G. Verschaffelt, "Polarization behavior and mode structure of vertical-cavity surface-emitting lasers with elliptical surface relief," in *Vertical-Cavity Surface-Emitting Lasers VII*, C. Lei and S.P. Kilcoyne (Eds.), Proc. SPIE 4994, pp. 127–138, 2003.